

CZECH TECHNICAL UNIVERSITY IN PRAGUE

**Faculty of Electrical Engineering
Department of Measurement**

Magnetic sensors and gradiometers for detection of objects

Doctoral thesis

Author: Ing. Jan Vyhnánek

**Supervisor: Prof. Ing. Pavel Ripka, CSc.
Supervisor-specialist: Ing. Michal Janošek, Ph.D.**

**PhD Programme: P2612, Electrical Engineering and Information Technology
Branch of study: 2601V006, Measurement and Instrumentation**

Prague, 2018

Declaration

I declare, that this work is all my own work and I have cited all sources I have used in the bibliography.

Prague, 6. 6. 2018

Prohlašuji, že jsem předloženou práci vypracoval samostatně a že jsem uvedl veškerou použitou literaturu.

V Praze, 6. 6. 2018



Acknowledgements

I would like to express my gratitude to my supervisors Prof. Ripka and Dr. Janošek for their scientific guidance and patience during my studies. This thesis would not be possible without the support of my family, which I very much appreciate.

Abstract

This thesis describes development of innovative sensor systems based on anisotropic magnetoresistors (AMR) and fluxgate sensors for applications in proximity detection and magnetic field mapping devices for visualization of hidden metal objects. These devices are aimed at replacing detectors based on large induction coils which have low spatial resolution and which do not offer possibilities for precise location and visualization of metallic objects. Conversely, the AMR and fluxgate sensors have smaller sensing elements and high spatial resolution and additionally they offer frequency response starting from DC, which makes them especially suitable for very low frequency applications.

The first part of the thesis describes measurement of selected characteristics of commercial AMR and fluxgate sensors to consider suitability of such sensors in detectors in terms of noise and crossfield sensitivity.

The second part is dedicated to development of metal detectors and proximity sensors. First, a gradiometer with AMR sensors was developed which operates with an AC excitation coil. This configuration provides the sensitivity to metallic objects due to eddy currents, if the material has a high conductivity, and to an AC magnetic field induced by the AC excitation, if the material has a high permeability. A DC gradient appears also, if the object has a remanent magnetic field or an induced DC magnetic field as a response to the Earth's field. This gradiometer with multiple outputs and high spatial resolution was used in a mine detector with an array of gradiometers to enable visualization and possibly recognition of mines from scrap metal. Based on the parameters obtained, the mine detector was later redesigned to a device for visualization of concealed metallic structures in buildings.

Further, a proximity sensor in a simplified configuration was developed. Only one AMR sensor, excitation coil and square-wave generator are necessary; signal demodulation is provided directly by the AMR sensor. This proximity sensor is suitable for low frequency applications, for example detection through a conductive casing. A modified design with an array of commercial integrated fluxgate sensors was used for position detection for pneumatic actuators. This linear position sensor is fitted outside of the aluminum cylinder and detects the position of a common ferromagnetic rod, because the low-frequency excitation field penetrates the aluminum cylinder wall. Attached is also work on fluxgate gradiometers to compare the most important parameters with those achieved by the AMR gradiometers.

Keywords: Magnetic sensors, Mine detectors, AMR sensors, Fluxgate sensors, Gradiometers, Position sensors

Abstrakt

Disertační práce popisuje vývoj nových detekčních zařízení s anizotropními magnetorezistory (AMR) a senzory fluxgate, které jsou určeny pro aplikace, jakými jsou detekce přiblížení a vizualizace skrytých kovových předmětů. Cílem je nahradit detektory s velkou indukční cívkou, které mají malé prostorové rozlišení a které neumožňují přesnou lokalizaci a vizualizaci kovových předmětů. Naopak senzory ARM a fluxgate mají malé rozměry snímacích elementů a velké prostorové rozlišení a navíc jsou citlivé na střídavá i konstantní magnetická pole, takže mohou najít využití v aplikacích s velmi malou pracovní frekvencí.

První část práce popisuje vybrané vlastnosti komerčních senzorů fluxgate a AMR a srovnává možnosti jejich použití v detektorech z hlediska šumu a parazitní citlivosti na kolmé magnetické pole.

Druhá část se věnuje vývoji detektorů kovových předmětů a senzorů přiblížení. Nejprve byl vyvinut gradiometr se senzory AMR, který pracuje ve střídavém poli budicí cívky. Tato konfigurace umožňuje pomocí senzoru AMR detekovat vodivé předměty, díky odezvě vířivých proudů, a materiály s vysokou permeabilitou, pomocí magnetizace materiálu střídavým budicím polem. Jedním z výstupů je také stejnosměrná hodnota gradientu, která je citlivá na remanentní pole materiálu a stejnosměrnou magnetizaci vyvolanou zemským polem. Gradiometr s tímto množstvím výstupů a velkým prostorovým rozlišením byl použit ke konstrukci detektoru min s polem gradiometrů, který sloužil pro vizualizaci a případné rozpoznání min od kovového odpadu. Na základě dosažených parametrů byl tento detektor následně modifikován na zařízení pro vizualizaci zakrytých kovových struktur ve stavebnictví.

Dále byl vyvinut senzor přiblížení se zjednodušenou konstrukcí oproti gradiometru s AMR. Skládá se z jednoho senzoru AMR, budicí cívky a generátoru obdélníkového buzení. Demodulaci měřeného signálu provádí přímo senzor AMR. Tento senzor přiblížení je vhodný pro aplikace s nízkou pracovní frekvencí, například pro detekci předmětů za vodivým krytem. Upravená konstrukce s polem fluxgate senzorů integrovaných na čipu sloužila pro detekci pozice pístu pneumatického aktuátoru. Lineární senzor polohy se připevňuje vně hliníkového válce a detektuje pozici pístu z běžné feromagnetické oceli díky nízké pracovní frekvenci budicího pole, které proniká pláštěm hliníkového válce. Pro porovnání parametrů dosažených s AMR senzory je uvedeno také několik článků na téma gradiometrů s fluxgate senzory.

Klíčová slova: Senzory magnetického pole, Detektory min, Senzory AMR, Senzory fluxgate, Gradiometry, Senzory polohy

Table of contents:

1	STATE OF THE ART.....	6
1.1	SENSOR TECHNOLOGIES.....	6
1.1.1	<i>Induction coils.....</i>	6
1.1.2	<i>Fluxgates.....</i>	6
1.1.3	<i>AMRs.....</i>	7
1.1.4	<i>GMRs and TMRs.....</i>	7
1.1.5	<i>Resonant magnetometers, Hall sensors and other.....</i>	8
1.2	APPLICATIONS.....	8
1.2.1	<i>DC Magnetic field mapping.....</i>	9
1.2.2	<i>AC methods.....</i>	9
1.2.3	<i>Non-destructive testing.....</i>	10
2	OBJECTIVES OF THE THESIS.....	12
3	OWN RESULTS.....	13
3.1	CHARACTERIZATION OF MAGNETIC SENSORS.....	13
3.1.1	<i>Experimental Comparison of the Low-Frequency Noise of Small-Size Magnetic Sensors.....</i>	14
3.1.2	<i>Low frequency noise of anisotropic magnetoresistors in DC and AC-excited metal detectors.....</i>	19
3.1.3	<i>Crossfield response of industrial magnetic sensors.....</i>	25
3.2	APPLICATIONS.....	35
3.2.1	<i>AMR Gradiometer for Mine Detection.....</i>	35
3.2.2	<i>CW Metal Detector Based on AMR Sensor Array.....</i>	41
3.2.3	<i>Linear scanner with magnetic field mapping.....</i>	45
3.2.4	<i>AMR Proximity Sensor With Inherent Demodulation.....</i>	50
3.2.5	<i>Linear Position Sensing through Conductive Wall without Permanent Magnet.....</i>	56
3.2.6	<i>Localization of the Chelyabinsk Meteorite From Magnetic Field Survey and GPS Data.....</i>	61
4	CONCLUSIONS.....	69
5	LIST OF OWN PUBLICATIONS.....	70
	REFERENCES:.....	76
6	ATTACHMENT: OTHER PUBLICATIONS RELATED TO THE THESIS TOPIC.....	82
6.1.1	<i>Compact magnetic gradiometer and its astatization.....</i>	82
6.1.2	<i>Simple estimation of dipole source z-distance with compact magnetic gradiometer.....</i>	87
6.1.3	<i>The Effect of Sensor Size on Axial Gradiometer Performance.....</i>	92
6.1.4	<i>Effects of Core Dimensions and Manufacturing Procedure on Fluxgate Noise.....</i>	97

1 State of the art

1.1 Sensor technologies

This chapter describes the most relevant magnetic field sensors which are commonly used in practice and is focused on factors limiting the resolution, range and usability of sensors rather than properly explaining their principle.

1.1.1 Induction coils

Recent overview of induction sensors was compiled by Tumanski (2007a). These sensors are based on Faraday's law and their advantages are relative simplicity of production and predictable behavior allowing precise calculation of parameters. For high frequencies the resolution of magnetic field measurement is comparable with cryogenic magnetometers. Disadvantages are frequency dependent transfer function and the fact that the voltage output depends on the time derivative of the magnetic field.

Theoretical background and modeling of induction coil sensors is provided by Timofeeva (2011). Paperno (2012) worked on analytical optimization of induction coils for minimum noise. Higher resolution is attained by increasing coil diameter or by adding the ferromagnetic core; increasing the number of turns results in increased resistance, parasitic capacitance and noise. The study of sensitivity and spatial resolution of induction sensors for non-destructive testing is described by Gilles (2012). A differential sensor with 0.8 cm^3 had the white noise of $0.4 \text{ pT}/\sqrt{\text{Hz}}$ starting from 10 kHz. Prance (1999; 2000) presents a gradiometer with 2-cm long coils with $125 \text{ fT}/\sqrt{\text{Hz}}$ above 10 kHz, which is comparable with SQUID magnetometers. The space magnetometer for Themis mission was developed to overlap the frequency range of measurement with fluxgates (Roux, 2008); it had a search coil with 7 mm in diameter and 170 mm length and the resulting noise was about $10 \text{ pT}/\sqrt{\text{Hz}}$ at 1 Hz and $0.02 \text{ pT}/\sqrt{\text{Hz}}$ at 1 kHz.

1.1.2 Fluxgates

Fluxgates are DC (meaning here steady-state) magnetic field sensors, the principle is based on modulation of permeability in a ferromagnetic core. The sensor is composed of the ferromagnetic core with excitation winding and the pick-up coil as the sensor output. Details about fluxgate sensors can be found in (Ripka, 2001). Fluxgates measure magnetic field in the range of approximately 10^{-10} to 10^{-4} T with very good linearity. They are suitable for measurements with resolution on the order of 1 nT, where the most limiting factors are temperature stability and sensor noise, which is commonly about $10 \text{ pT}/\sqrt{\text{Hz}}$ at 1 Hz.

Typical signal processing circuit consists of a phase sensitive detector and feedback compensator. The output of fluxgate sensors can be evaluated in time domain using simpler electronics than in the case of frequency domain, however the output noise is higher (Ando, 2008). Ripka (1995) shows the possibility to measure AC fields up to 10 kHz using the pick-up and feedback coil of a fluxgate. Zhang (2010) describes similar concept with a Vacquier type fluxgate. Fluxgates manufactured by the PCB technology offer the possibility of a cheaper production; Kubik (2006) reports a PCB racetrack fluxgate with a 30mm x 8mm core with the noise level of $24 \text{ pT}/\sqrt{\text{Hz}}$ at 1 Hz. Ruhmer (2011) studied spatial resolution and noise of racetrack fluxgates for measurements of dipole fields. Both parameters can be changed by the core geometry, but cannot be optimized independently.

1.1.3 AMRs

Detailed information about anisotropic magnetoresistors (AMRs) is summarized by Tumanski (2010). AMRs are based on the magnetoresistive effect in a thin ferromagnetic film. The resistance of the material depends on its state of magnetization. The magnetization of the material has two stable states which should be properly set by the so called flipping field, because the characteristic of the sensor can be deteriorated by a relatively small field. Commercial sensors consist of four MR elements connected in a full bridge to reduce temperature dependence and coils for flipping and feedback compensation. Compared to fluxgates the noise and temperature offset drift is typically hundred times higher. The measuring range without feedback compensation is limited to several hundreds of A/m.

Ripka (2003) describes an AMR magnetometer with switched integrators to avoid the most noisy time intervals following the flipping pulses. The magnetometer has a temperature offset drift of 10 nT/K, noise at 1 Hz is typically $2 \text{ nT}/\sqrt{\text{Hz}}$ and linearity 0.2 % without feedback and 0.04 % with the feedback coil in the range of $\pm 200 \text{ } \mu\text{T}$. The flipping amplitude influences the output noise and offset (Hauser, 2003). With higher amplitude of the short flipping pulses the output noise is decreased about two times by increasing amplitude from 0.5 A to 3 A. Influence of the feedback and flipping on linearity and temperature stability is studied by Platil (2003).

While the 1/f noise is fixed, the Johnson noise depends on the sensor sensitivity, thus on the supply voltage of the resistor bridge. He (2009) shows an AMR magnetometer for NDT with an $800 \text{ } \Omega$ sensor supplied by 24 V where the Johnson noise is as low as $12 \text{ pT}/\sqrt{\text{Hz}}$ at 1 kHz. However this arrangement has high power consumption of the bridge supply. Magnetoresistors can be used to build a magnetometer for a small satellite where fluxgates are too bulky (Brown 2012). Noise level of $50 \text{ pT}/\sqrt{\text{Hz}}$ at 1 Hz referred in this paper is more than three times lower than that declared by the manufacturer of the AMR HMC1001 (Honeywell 2008). Linearity improvement of this sensor by the feedback compensation of the measured field is demonstrated by Hadjigeorgiou (2017).

1.1.4 GMRs and TMRs

Giant Magnetoresistors (GMR) and Spin Dependent Tunneling (SDT or TMR) devices and their applications are described in Daughton (2000). Function and basic properties of Giant Magnetoresistors is described in (NVE Co., 2005). The effect arises in thin ferromagnetic film multilayers by magnetic modulation of the electron spin in the material. Magnetoresistive properties are up to 20 times larger than the effect of AMR, the magnetoresistance percentage is up to 40 % and sensitivity to magnetic field reaches in some cases also higher values. For this reason and due to better spatial resolution GMR replaced AMRs in reading heads in hard drives. Vopalensky (2003; 2004) states, that although GMR and SDT sensors offer higher sensitivity than AMR, they currently cannot be used for precise linear measurements due to high non-linearity and hysteresis, for the GMR 3 % and 2 % respectively, hysteresis of an AC biased SDT was 12 % of full scale.

Output noise of GMRs is comparable to AMRs, measurements of several commercial GMR sensors is provided by Stutzke (2005). A cross-correlation method using two amplifiers allows measurement which is free of the noise of the processing electronics. Ripka (1999) measured noise, offset and hysteresis on GMR sensors and improved these parameters by AC excitation. Tondra (1999) developed a low noise SDT sensor with theoretically achievable resolution on the order of 1 pT if 1/f noise is reduced and only the thermal noise is the remaining source of noise.

1.1.5 Resonant magnetometers, Hall sensors and other

Further principles of magnetic sensors are described in (Ripka, 2001). The important devices for low field measurements are resonant magnetometers. Resonant magnetometers are based on nuclear magnetic resonance and the known gyromagnetic ratios of proton and electron. Resonant magnetometers for low field measurements are proton precession, Overhauser and optically pumped magnetometers. Magnetic field resolution is better than resolution of fluxgates, however resonant magnetometers are more bulky. The output is a scalar value of the magnetic field without temperature dependence or necessary calibration, but the measuring range starts from a certain minimum, otherwise the output signal is too low. Measuring range can be extended using external biasing field; this method also allows construction of vector resonant magnetometers. Although the magnetometers are principally insensitive to direction of the magnetic field, there is a dependence of the signal amplitude on the angle between the magnetic field and axis of the solenoid coil. So for some angles the sensor is not operating properly or is noisy. Although omnidirectional sensors are available, the construction is more complicated.

Magnetic sensors based on Hall effect are commonly used for position sensing applications, however this sensor usually needs a strong magnetic field to work properly, because its noise is several orders higher than the noise of MRs and fluxgates and the sensitivity is relatively low. Popovic (2002) summarizes key features of AMRs and GMRs and compares them with Hall sensors enhanced by concentrators. In some parameters like the full scale range Hall sensors are better than MRs, noise of Hall sensors is however still much higher. Reiniger (2006) describes applications of Hall and MR sensors for position control; usability of sensor arrays is discussed.

Other significant sensors are superconducting quantum interference devices (SQUIDS). They are cryogenic sensors reaching white noise of about $10 \text{ fT}/\sqrt{\text{Hz}}$, however with a complicated construction and operation. SQUIDS measure only field changes. Another principles are magnetoimpedance and magnetoinductance, but sensors using these effects have no significant advantage over MRs and fluxgates and till now have no such success in practice.

1.2 Applications

Magnetic field measurements can be divided into scalar field and vector measurements, additionally gradient and tensor can be estimated (Bracken, 2006). Scalar field magnetometers measure only the magnitude of the field and are insensitive to its direction. Scalar gradient is measured by operating two scalar magnetometers at a fixed distance - the difference of their reading divided by their distance (called gradiometric base) is an estimate of the gradient; it makes the nearby anomalies more pronounced and removes the variations of the Earth's field. Vector magnetometers measure the magnitude and direction of the field, precise attitude of the magnetometer has to be known. Using an array of vector magnetometers at a fixed distance a gradient tensor can be measured, however common vector gradiometers measure the gradient only in the direction of the gradiometric basis.

Most of the applications employ an excitation field. Magnetic field of the Earth is sufficient for several applications to induce a detectable magnetic field in objects where the remanent field is not available. Other magnetometers use an AC or DC excitation field generated by induction coils or magnets. The AC magnetic field is useful for detecting conductive objects using the magnetic response of eddy currents.

1.2.1 DC Magnetic field mapping

Complex information on the application of the DC magnetometers and gradiometers, especially the proton and fluxgate ones, is provided by Breiner (1999). These instruments are used in a search for buried objects, geological mapping, mineral exploration, geophysical research and archeology. The magnetic anomalies detected by the magnetometers originate in magnetic properties of buried objects and minerals in soil and rocks. Even non-magnetic buried objects or voids can be revealed by magnetic measurements as a gap in mineralized soil. The better the resolution of a magnetometer the more information on the scanned area is obtained, however the required resolution depends on the particular goal of the measurement. The Earth's magnetic field varies in time due to solar wind and other phenomena, resulting in diurnal variations and micropulsations. These effects have to be eliminated typically if the measurement takes more than 5 minutes and anomalies of interest are less than 50 nT.

Typical sensors for this application are resonant magnetometers. Mapping with a single sensor can be time consuming, so multiple sensor systems were developed. An array of eight Cs-vapor magnetometers in combination with three induction coils with a size of 1 m x 1 m is reported by Nelson (2001) for detection and characterization of unexploded ordnance. A similar system is reported by Siegel (2008).

The main disadvantages of fluxgates compared to resonant magnetometers are calibration errors and drift, which should be compensated by calibration before the beginning of the measurement (Munsch, 2007). Bartington (2004) describes a fluxgate gradiometer with the 1 m sensor separation intended for archeological applications and compares it with nuclear resonance magnetometers. The fluxgate magnetometers suffer from a temperature dependent output drift which is compensated by the calibration before beginning of each survey; calibration improves the heading error down to 0.5 nT. Merayo (2005) constructed a fluxgate gradiometer for space applications with the resolution of 100 pT/m and with 0.5 nT long-term stability of the sensor offset. Advantages of the fluxgate gradiometers are lower power consumption, overall weight, cost effectivity and suitability for array systems; they can provide higher data rates than resonant magnetometers. Fluxgate gradiometers are used for detection of deeply buried remnants of war (Hochreiter, 2000).

A SQUID gradiometer described by Linzen (2007) with the noise of 7 fT/cm in the frequency range 0.01 Hz to 10 Hz was used in archeological prospecting. The main disadvantage is the necessary supply of liquid helium for cooling with a filling cycle of two days.

1.2.2 AC methods

One of the main applications of AC metal detectors is demining. The basic principles and demands on the mine detectors are covered in Guelle (2003). Usually continuous wave and pulsed eddy current metal detectors are used with the ability to locate minimum-metal mines in soil with difficult electromagnetic properties. Overview of patents related to metal detectors is summarized by Siegrist (2002), who states, that patents are a valuable source in this case, as there is otherwise a lack of information. Bruschini (2000b, 2002) describes a theoretical background for eddy current detectors and shows possibilities of object discrimination using phase angle information from a commercial two-frequency mine detector Foerster Minex 2FD.

Bruschini (2000a) provides an overview of metal detectors for demining and reports on tests of commercial imaging metal detector Ferrosan (Hilti, 2006). Comparison of metal detectors with alternative methods for mine detection provides Lewis (2004) and McDonald (2003). Krueger (2008) shows a method to map the response of eddy currents using the standard

handheld metal detector. Ultrasound position sensors record the trace of the detector head so together with the detector output a signature graph is created and object recognition is possible. Ripka (2010) aims at the same goal using inertial navigation and infrared distance sensors. A mobile platform carrying the mine detector on a robotic arm was studied for safer automated demining (Fukuschima, 2009).

For characterization and discrimination of metal objects without the need of scanning a multiple coil gradiometer can be used (Gaspornikova, 2010). Wold (1999) constructed a handheld metal detector with a SDT array and pulse excitation, the detector was intended for demining with object recognition.

A commercial device MIT-Scan2 (MIT, 2008) is based on imaging using an array of eddy current sensors and is used to visualize ferrous joints in highways and pavements. Induction sensors are widely used in industrial applications for proximity detectors (Jagiella, 2006). An array of induction sensors with a single excitation coil is used for detection of metal pieces in glass recycling industry (Mesina, 2003). The receiver sensors have 7 mm in diameter and are connected as 30 gradiometers. The excitation coil has dimensions of 10 cm x 68 cm. The excitation frequency is variable from 700 Hz to 5 kHz.

1.2.3 Non-destructive testing

A typical eddy current sensor for non-destructive testing (NDT) is an induction sensor. Recent progress was however related rather to probes with magnetoresistors due to the high spatial resolution and sensitivity to the DC and low-frequency magnetic field. Comprehensive overview of magnetoresistors in NDT provides Jander (2005) and Smith (1999; 2000). Comparison between induction coil, GMR and AMR sensors for detection of cracks in metals was done experimentally by Hesse (2005). Very low excitation frequency of 350 Hz was used to achieve high depth of penetration. The results of detectivity and resolution test were similar for both MRs and a 8000-turn coil; the main disadvantage of the coil was a difficult reproducibility. Comparison between AMR and GMR eddy current probes is provided by Cherepov (2004). The fluxgate (specifically fluxset) sensor proved to be suitable for detection of metal cracks using eddy currents (Vértesy, 2000) and an array of fluxgates can be used for detection of DC magnetic signatures of cracks in ferromagnetic metals (Gruger, 2003).

An eddy current sensor with AMR was presented by Sikora (2001; 2003) and He (2011), multifrequency excitation enables to reduce lift-off effects. Torres (2005) used an AMR in a multifrequency probe to distinguish between different types of metal.

Eddy current GMR sensor is described in Wincheski (2000), Dogaru (2001) and Pasadas (2011). The main advantage of this technology is small sensor size allowing high spatial resolution and a broad frequency range from 1 Hz to 1 MHz. A rotational GMR probe can be used for detecting deeply buried cracks around a fastened holes (Wincheski, 2002; Dogaru, 2004). An NDT system using GMRs is described in Iorio (2007). A probe with 16 GMR elements and 100 Hz excitation is able to visualize defects in aluminum plates in depth up to 2 mm (Yashan, 2006).

Methods and devices for detecting and visualizing reinforcing bars in concrete are summed up in Gaydecki (2007). Among these devices belong Q-sensors, pulsed eddy current sensors and DC excited magnetometers. A commercially successful device for imaging of reinforcing bars in concrete based on DC field excitation is Ferrosan (Kousek, 1997; Hilti, 2006). A large magnet produces the magnetic flux which is distorted by a nearby ferromagnetic object. These variations are sensed by DC sensors in differential arrangement. An AC excitation is possible too. Depending on the the diameter of the bar the maximum working depth is 18 cm.

Benitez (2008, 2009) used magneto-impedance sensors in a magnetic imaging system. A DC field is excited by a coil and a 2D array of magneto-impedance sensors creates the magnetic image of a nearby object, e.g. reinforcing bars in concrete.

Several more application examples of DC sensors can be mentioned. Magnetic field of ferromagnetic objects like transformer components or magnets can be mapped using Hall and GMR probes (Christides, 2003) and AMR (Tumaski, 2002; 2007b). A Hall sensor was used for scanning of a polished surface of a rock sample to visualize the textures of the magnetic field (Kletetschka, 2013). Zimmermann (2005) used an array of AMR for magnetoelectrical resistivity tomography. A 2D array of magnetoresistors on one chip was used for forensic study of audio tapes and imaging currents in integrated circuits (Halloran, 2007).

2 Objectives of the thesis

- I. To design metal detectors with AMR sensors which have higher spatial resolution than induction coils.
- II. To solve the problem of the sensor operation in a strong excitation and biasing field. This can be achieved either by:
 - II.a. Field compensation – compensation coil may have large power consumption.
 - II.b. By measuring in the direction perpendicular to the excitation field. In this case problems with crossfield sensitivity are expected.
- III. To explore applications, where DC magnetic field sensors can replace induction sensors by virtue of better sensitivity at low frequencies.

To fulfill the tasks (I.), (II.b.) and (III.), detailed characteristics of the available commercial sensors have to be measured and compared. The tasks (I.), (II.a.) and (III.) require a development work on an innovative hardware to be carried out, so the metal detectors and other applications are designed. Realization of these tasks is described in the following pages.

3 Own results

Own results are presented in the form of the following nine journal and conference papers. They are ordered logically starting with characterization and comparison of sensors in chapter 3.1 and followed by applications in innovative sensor systems for detection of objects and position sensing in chapter 3.2. This ordering sometimes does not correspond to the chronological order, therefore knowledge and sensors already introduced by some paper may not be reflected in all the consecutive papers.

3.1 Characterization of magnetic sensors

The following papers supplement the information about selected commercial sensors which is not available in datasheets and literature. Chapters 3.1.1 and 3.1.2 present noise comparison of induction coil, integrated fluxgate and AMR sensors. These chapters are related to the objective of using DC magnetic sensors for low frequency applications (objective III.) and for design of metal detectors (I.). My contribution to the respective two papers was the experimental work and processing of measured data. Measurement of crossfield effect in an AMR and integrated fluxgate sensor is shown in chapter 3.1.3., which is related to the objective (II.b.) For this paper, I participated on designing of the measurement setup and on processing of the data.

Further sensor characteristics are usually available in literature to select the sensor which is best suited to the final application. Apart from detailed noise and crossfield data, other parameters has to be considered, for example power consumption, sensitivity, frequency dependence and input range of the sensor, complexity of conditioning circuits, spurious sensitivity to electromagnetic fields or manufacturing complexity. Some of these topics are discussed later in chapter 3.2.

3.1.1 Experimental Comparison of the Low-Frequency Noise of Small-Size Magnetic Sensors

The goal was to experimentally estimate the frequency range in which selected DC magnetic sensors are superior to induction sensors in terms of noise. The criterion for selection of the sensors was the similar size of the sensor package rather than the size of the sensing element. Commercial SMD fluxgate and AMR sensors have been chosen and compared with an 8 mm x 1 mm induction coil with ferrite core.

The primary reason why AMR sensors can often replace induction sensors in NDT applications (chapter 1.2.3) is the small sensing element size and its better spatial resolution with the advantage of low-frequency operation. Metal detectors with sensor arrays, on the other hand, allow bigger induction sensors to be used, considering that the detected objects are rather large.

The resulting frequency range, where the AMR and integrated fluxgate sensors performed better than the induction coil, was surprisingly low and widely varying, depending on the sensors selected (Fig. 9 in the paper). For example while the AMR HMC1001 in a low noise circuit had better noise than the coil from DC to 100 Hz, the integrated fluxgate DRV425 had better noise from DC to 7 Hz. Considering solely the noise data, some application designs with 1 kHz working frequency in chapter 3.2 would benefit from exchange of AMRs for induction coils.

Noise of the induction sensor also depends on selection of the conditioning circuit. The paper describes how to measure even DC field, when the coil is operated in a fluxgate mode. Such a sensor has a noise of $1 \text{ nT}/\sqrt{\text{Hz}}$ @ 1 Hz, which is comparable to the noise of the integrated fluxgate sensor and noisy types of AMR sensors. Further details are given in the paper.

Experimental Comparison of the Low-Frequency Noise of Small-Size Magnetic Sensors

Jan Vyhnanek and Pavel Ripka

Department of Measurement, Faculty of Electrical Engineering, Czech Technical University in Prague, 16627 Prague, Czech Republic

Small-size ac magnetic-field sensors are used for nondestructive testing (NDT), magnetic particle detection, and other applications, which require high spatial resolution. Up to now, inductive coils dominated this area, as their sensitivity at kHz frequencies, is superior to other magnetic sensors. However, some applications, such as magnetic imaging through conducting sheath, require lower working frequencies, in extreme case units of Hz. We successfully replaced inductive coils by an AMR sensor in NDT application and for distance measurement. In this paper, we compare designs of miniature ac magnetic field sensors, their achievable frequency characteristics, dynamic range, and noise parameters.

Index Terms—Magnetic sensors, noise measurement.

I. INTRODUCTION

COMPARISON of magnetic sensors of different technologies was recently done by Robbes in [1]. He used energy resolution-volume criterion and concluded that SQUID and SERF achieve the best resolution. However, these sensors are not practical for the industrial applications such as nondestructive testing (NDT).

In this paper, we compare commonly available small-size room temperature sensors: an induction coil with 8 mm long ferrite core (Fig. 1) and commercial fluxgate and AMR sensors. The selected sensors have comparable dimensions of the casing rather than the sensing element size. This is a practical criterion for the design of gradiometers or multiple sensor detectors. Dimensions of the sensing element, however, influence the spatial resolution of the sensor, an important requirement, e.g., in NDT applications, in position sensing, and in the detection of small ferromagnetic or superparamagnetic objects. Gruger [2] describes an array of planar fluxgate sensors for NDT. The sensors are 1 mm long and they have 0.5 mm pitch. Vertesy and Gasparics [3] used a similar sensor with time-output and unipolar excitation. Butin *et al.* [4] and Dolabdjian *et al.* [5] replaced induction coil in a pulsed eddy current system by GMR sensors. We have used an AMR sensor instead of the induction coil in the eddy-current position and distance sensor [6].

In this paper, we compare sensor noise at low frequencies, i.e., DC to 1 kHz following the study we made on AMR sensors [7]. In this frequency range, the sensor noise is the limiting factor for NDT applications. Similar study of magnetoresistive sensors was made by Stutzke *et al.* [8].

II. INDUCTION COIL

Induction coils are traditionally used in geophysics to measure magnetic field variations [9]. An induction coil can reach

Manuscript received August 10, 2016; revised November 15, 2016; accepted November 19, 2016. Date of publication November 29, 2016; date of current version March 16, 2017. Corresponding author: J. Vyhnanek (e-mail: vyhnajan@fel.cvut.cz).

Color versions of one or more of the figures in this paper are available online at <http://ieeexplore.ieee.org>.

Digital Object Identifier 10.1109/TMAG.2016.2633398

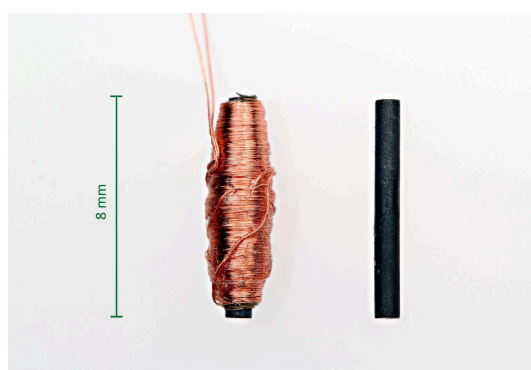


Fig. 1. Sensor with 2000 turns wound around a ferrite core and a ferrite core without the winding.

a resolution of fluxgate sensors at 1 Hz, but the dimensions and weight of such a coil is usually large [10], [11].

In the position detectors with moving magnets, induction sensors have been replaced by Hall and AMR sensors, which have speed-independent signal. However, induction coils are the most popular sensors in eddy current position sensors and NDT systems. Induction coils can be used either in the voltage output mode or in the current output mode. Theoretical model and real data comparison of a coil with the same instrumentation amplifier INA163, which was used here, are given in [12].

An induction coil with 2000 turns and 8 mm \times 1 mm ferrite core was developed in our laboratory and successfully tested *in vivo* as an inductive distance sensor to monitor gastric motility [13]. The coil is wound with a 0.035 mm diameter copper wire and its resistance R_s is 200 Ω .

After inserting the ferrite core, the coil inductance L_s was increased by the factor of 13 (from 1.4 to 18.6 mH) and the sensitivity increased by the factor of 12 at all frequencies. These are lower values than the theoretical apparent permeability of 50 according to [14]. One explanation of this discrepancy may be the influence of the real coil geometry.

The frequency dependence of the sensitivity of voltage output coil is shown in Fig. 2(a). The resonance peak of the

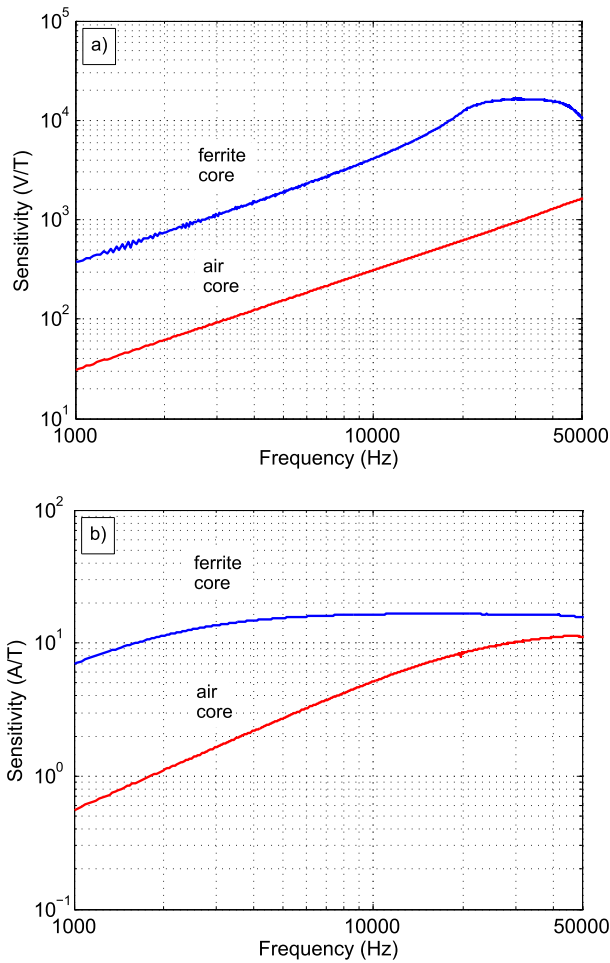


Fig. 2. Frequency dependence of the 8 mm long induction coil with and without ferrite core (a) with voltage output and (b) with current output.

cored coil is caused by coil self-capacitance in parallel with inductance.

The theoretical disadvantage of the induction coil with voltage output is its strong frequency dependence of sensitivity. The coil with current output is theoretically frequency independent for frequencies higher than

$$f_c = R_s / (2\pi L_s). \quad (1)$$

However, for small induction coils, this frequency is very high. The real frequency characteristics of the current output coil with and without a core are shown in Fig. 2(b). For the cored coil and the current output, the measured cutoff frequency corresponds to the theoretical value $f_c = 1.7$ kHz for $L_s = 18.6$ mH. For the air coil, the calculated f_c is 23 kHz.

Fig. 3 compares three conditioning circuits connected to the cored induction coil to select the optimal method of signal processing. Transimpedance amplifiers with INA163 and LT1028 were used for the current output. The value of the conversion resistor is 6 k Ω . The coil in the voltage output mode was connected to a voltage amplifier with INA163 with the gain of 1000. From the measured characteristics, we may conclude that for this type of the induction coil, voltage amplification is the best to achieve minimum noise.

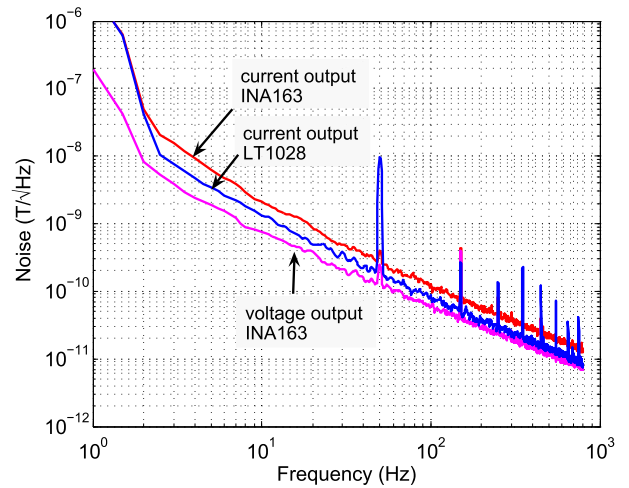


Fig. 3. Comparison of induction coil noise with voltage amplifier and transimpedance amplifier (current output) for 1–800 Hz.

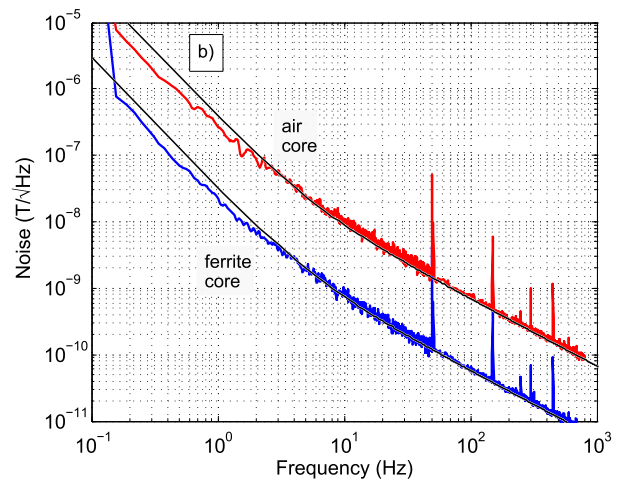
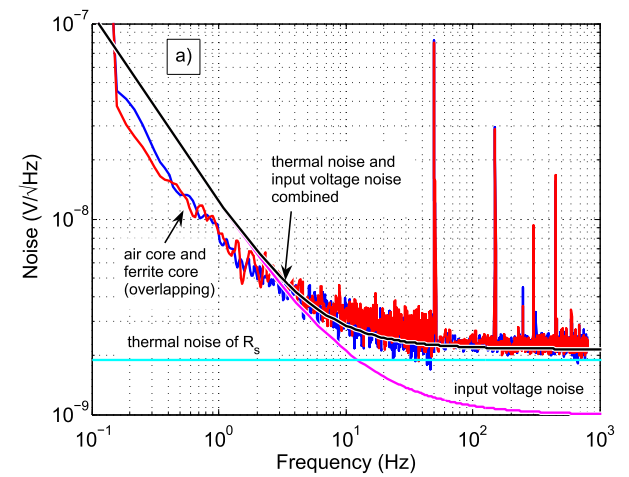


Fig. 4. Induction coil with core connected to INA163 voltage amplifier compared with modeled thermal noise and voltage noise of INA163. (a) In volts. (b) Recalculated in the units of magnetic field.

Fig. 4(a) shows the measured and modeled noise voltage for the voltage output coil compared with the calculated values. For the frequencies below 10 Hz, the dominant source of the noise is $1/f$ voltage noise of the amplifier, while the

TABLE I
 COMPARISON SUMMARY

Sensor	Conditioning circuit	Sensor dimensions (mm ³)	Sensor weight (g)	Freq. upper limit (kHz)	Sensor range (mT)	Noise, 10 Hz (nT/ $\sqrt{\text{Hz}}$)	Noise, 100 Hz (nT/ $\sqrt{\text{Hz}}$)
Coil, air core	INA163, G=1000 \times	8 \times 2.5 \times 2.5	0.01	>50	>1000	10	0.8
Coil, ferrite c.	INA163, G=1000 \times	8 \times 2.5 \times 2.5	0.13	20	5	0.8	0.07
Coil, fluxgate	Lock-in SR865	8 \times 2.5 \times 2.5	0.13	1	<5	1.2	1
HMC1001	AD8429, G=100 \times	11 \times 4 \times 2	0.15	4*	0.2	0.065	0.05
HMC2003	included in sensor	27 \times 20 \times 9	1.28	1	0.2	0.25	0.25
DRV425	included in sensor	4 \times 4 \times 0.8	0.04	32	2	1.5	1

*4 kHz with 10 kHz flipping and demodulation, 1.2 MHz without flipping

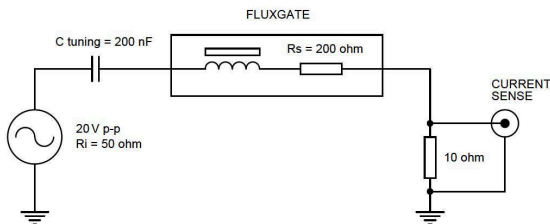


Fig. 5. Setup for the fluxgate sensor with current output.

contribution from the current noise is negligible. The noise model is based on datasheet data. The theoretical white noise of the coil is mainly determined by the thermal noise voltage of the coil resistance and the white noise region U_n of the voltage noise of the amplifier; for $R_s = 200\Omega$, $U_n = 1 \text{ nV}/\sqrt{\text{Hz}}$, room temperature T , and Boltzmann constant k , the combined white noise results in

$$U_{\text{white_total}} = \sqrt{4kTR_s + U_n^2} = 2.1 \text{ nV}/\sqrt{\text{Hz}}. \quad (2)$$

The measured value is $2.3 \text{ nV}/\sqrt{\text{Hz}}$. As the measured voltage noise with and without core is identical, the contribution of the magnetic noise of the core is negligible. Noise recalculated to the field units is shown in Fig. 4(b). It is clear that due to the frequency dependence of the sensitivity, the noise decreases with frequency monotonically. The achieved noise level with the cored coil is $0.8 \text{ nT}/\sqrt{\text{Hz}}$ @ 10 Hz and $22 \text{ nT}/\sqrt{\text{Hz}}$ @ 1 Hz.

The cored induction coil has a field amplitude range limited by the saturation of the core to 5 mT. Compared with that, the upper field range of the air coil is only limited by the output amplifier. In our case, the maximum measurable field on the high-resolution range is 1 mT. This field range can be further extended even over 1 T by decreasing the amplifier gain.

We also tested signal processing by analog integrator: homemade using LT1028 and commercially available Lakeshore 480. Due to the high resistance of the induction coil, the value of feedback capacitor should be about $1 \mu\text{F}$ and resulting sensitivity is very low.

III. INDUCTION COIL AS A SINGLE ROD FLUXGATE

The described miniature induction coil can be turned into the fluxgate sensor. The advantage of this unusual sensor is that it has only one winding. Setup for the fluxgate mode measurement is shown in Fig. 5. The sensor is excited in the voltage mode using $20 \text{ V}_{\text{p-p}}$ /2.3 kHz sinusoidal voltage. The capacitor C serves to decouple any dc component in the

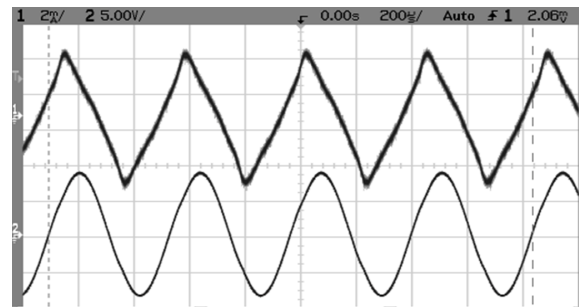


Fig. 6. Sensor current with higher harmonics due to core saturation (upper trace, 2 mA/div) and generator voltage (lower trace, 5 V/div).

excitation and to increase the excitation current amplitude by tuning.

The generator voltage and the corresponding sensor current are shown in Fig. 6. The excitation current was $8 \text{ mA}_{\text{p-p}}$. When the external dc field is present, second-harmonic component appears in the excitation current. This second harmonics is measured as a voltage drop across the 10Ω sensing resistor by the SR865 lock-in amplifier. At higher frequencies, most of the noise in the setup comes from the amplifier in this case considering the large feedthrough of the excitation signal to the output current.

Sensitivity dependence on the frequency of the excitation current was measured for constant excitation voltage of $20 \text{ V}_{\text{p-p}}$ (Fig. 7), and for the noise measurement, an excitation frequency of 2.3 kHz in the high-sensitivity region was selected.

Comparing the noise of fluxgate mode and induction mode (Fig. 8), a crossing of the two characteristics at around 10 Hz indicates the suitability of each mode for a specified frequency region: for frequencies from DC to 10 Hz, the recommended sensor mode is fluxgate, for higher frequencies induction coil.

IV. COMPARISON WITH COMMERCIAL SENSORS

We compared the performance of the developed sensors with sensors available on the market. The results are shown in Fig. 9 and a summary of parameters is given in Table I.

HMC2003 is a three-axis magnetic sensor module manufactured by Honeywell, which contains AMR sensor HCM1001 with instrumentation amplifier and a biasing source. The measured noise at 10 Hz is $250 \text{ pT}/\sqrt{\text{Hz}}$. No flipping (set/reset of the magnetic state) was applied. However, for

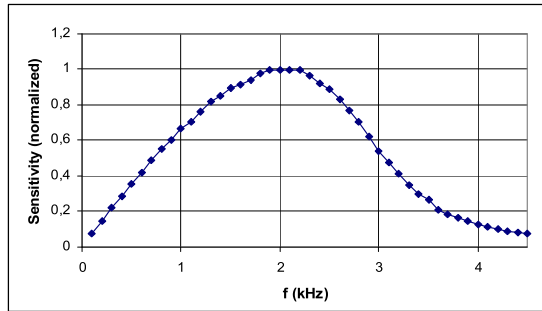


Fig. 7. Sensitivity of the fluxgate sensor in the measurement setup at the variable excitation frequency.

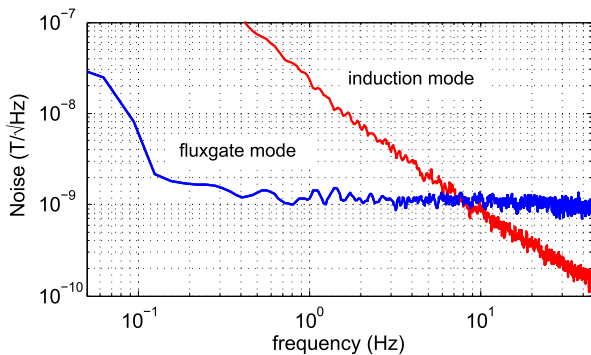


Fig. 8. Coil in fluxgate mode compared with induction mode using voltage output.

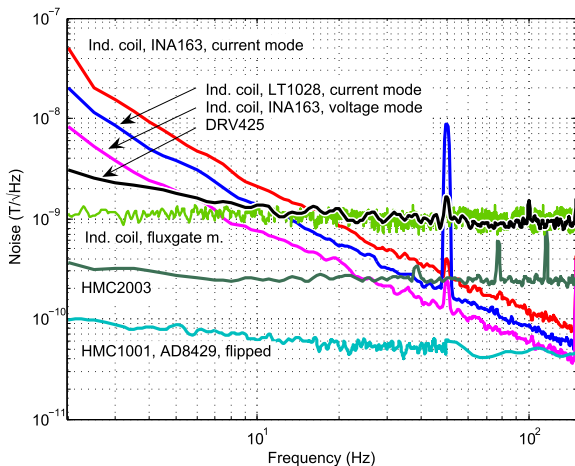


Fig. 9. Comparison of induction coil with AMR and fluxgate sensors for 2–250 Hz.

practical applications, the sensor should be periodically remagnetized (“flipped”) to ensure zero stability.

The same AMR sensor HMC1001 was characterized with enhanced electronics in [7]. The sensor was flipped at 10 kHz with an amplitude of $3.6 A_{p-p}$ and connected to a low-noise instrumentation amplifier AD8429 with a gain of 100. The biasing voltage was 5.5 V. After synchronous demodulation, the noise at 10 Hz is $65 \text{ pT}/\sqrt{\text{Hz}}$.

A serious limitation of the AMR sensors is their limited dynamic range. In this case, the maximum measurable field is 0.2 mT.

The last sensor in this comparison is integrated fluxgate DRV425 manufactured by Texas Instruments. This device has

both microfabricated fluxgate and complete electronics on a single CMOS-chip. We have used it in recommended circuit connection and 5.1 ohm shunt resistor to measure feedback current [15]. The measured noise is $1.5 \text{ nT}/\sqrt{\text{Hz}}@10 \text{ Hz}$. The maximum field range is 2 mT, which is 10 times the range of the AMR sensor.

V. CONCLUSION

In this paper, we compared the noise performance of small-size magnetic sensors suitable for NDT testing. With the exception of DRV425, the tested sensors work in open-loop. We describe small-size induction coil with high field range and noise level of $0.8 \text{ nT}/\sqrt{\text{Hz}}@10 \text{ Hz}$. At lower frequencies, the fluxgate mode of the same sensor is preferable, which at 1 Hz achieves already about 20 times better noise. Many industrial applications require high field range. From this point, the integrated fluxgate DRV425 offers the range of 2 mT, which is 10 times higher than that of AMR sensors. Our induction sensor works up to 5 mT with core and $>1 \text{ T}$ without the core.

REFERENCES

- [1] D. Robbes, “Highly sensitive magnetometers—A review,” *Sens. Actuators A, Phys.*, vol. 129, no. 1, pp. 86–93, 2006.
- [2] H. Grüger, “Array of miniaturized fluxgate sensors for non-destructive testing applications,” *Sens. Actuators A, Phys.*, vol. 106, no. 1, pp. 326–328, 2003.
- [3] G. Vértessy and A. Gasparics, “Nondestructive material evaluation by novel electromagnetic methods,” *Mater. Sci. Forum*, vol. 414, no. 1 pp. 343–352, 2003.
- [4] L. Butin, G. Waché, L. Perez, and C. Dolabdjian, “New NDE perspectives with magnetoresistance array technologies—From research to industrial applications,” *Insight, Non-Destructive Test. Condition Monitor.*, vol. 47, no. 5, pp. 280–284, 2005.
- [5] C. P. Dolabdjian, L. Perez, V. O. De Haan, and P. A. De Jong, “Performance of magnetic pulsed-eddy-current system using high dynamic and high linearity improved giant magnetoresistance magnetometer,” *IEEE Sensors J.*, vol. 6, no. 6, pp. 1511–1517, Jun. 2006.
- [6] P. Ripka, J. Vyhnanek, M. Janosek, and J. Vcelak, “AMR proximity sensor with inherent demodulation,” *IEEE Sensors J.*, vol. 14, no. 9, pp. 3119–3123, Sep. 2014.
- [7] J. Vyhnanek, M. Janosek, and P. Ripka, “Low frequency noise of anisotropic magnetoresistors in DC and AC-excited metal detectors,” *J. Phys. Conf. Ser.*, vol. 450, no. 1, p. 012031, 2013.
- [8] N. A. Stutzke, S. E. Russek, D. P. Pappas, and M. Tondra, “Low-frequency noise measurements on commercial magnetoresistive magnetic field sensors,” *J. Appl. Phys.*, vol. 97, no. 10, pp. 10Q107-1–10Q107-3, 2005.
- [9] S. Tumanski, “Induction coil sensors—A review,” *Meas. Sci. Technol.*, vol. 18, no. 3, pp. R31–R46, 2007.
- [10] A. Roux *et al.*, “The search coil magnetometer for THEMIS,” *Space Sci. Rev.*, vol. 141, no. 1, pp. 265–275, 2008.
- [11] E. Paperno and A. Grosz, “A miniature and ultralow power search coil optimized for a 20 mHz to 2 kHz frequency range,” *J. Appl. Phys.*, vol. 105, no. 7, p. 07E708, 2009.
- [12] M. Timofeeva, G. Allegre, D. Robbes, and S. Flament, “Differential search coils based magnetometers: Conditioning, magnetic sensitivity, spatial resolution,” *Sensors Transducers J.*, vol. 14, no. 1, pp. 134–150, 2012.
- [13] J. Tomek, “Inductive contactless distance measurement intended for a gastric electrical implant,” *Acta Polytech.*, vol. 47, nos. 4–5, pp. 76–79, 2007.
- [14] P. Ripka, “Induction sensors,” in *Magnetic Sensors and Magnetometers*, P. Ripka ed. Norwood, MA, USA: Artech House, 2001.
- [15] M. F. Snoeij, V. Schaffer, S. Udayashankar, and M. V. Ivanov, “Integrated Fluxgate Magnetometer for Use in Isolated Current Sensing,” *IEEE J. Solid-State Circuits*, vol. 51, no. 7, pp. 1684–1694, 2016.

3.1.2 Low frequency noise of anisotropic magnetoresistors in DC and AC-excited metal detectors

This work addresses noise performance of an AMR sensor in relation to flipping and excitation field. A thorough evaluation of noise sources is given, including thermal noise, magnetic noise and noise of an amplifier and demodulator.

A low-noise commercial anisotropic magnetoresistor HMC1001 was periodically flipped. A low noise instrumentation amplifier AD8429 was used for signal conditioning. With a 5.5 V bias voltage, the resulting noise was 30 pT/ $\sqrt{\text{Hz}}$ at 1 kHz and 125 pT/ $\sqrt{\text{Hz}}$ at 1 Hz.

When the sensor was not flipped, the noise at 1 Hz resulted in 246 pT/ $\sqrt{\text{Hz}}$, showing the capability of flipping to decrease the low-frequency noise of an AMR magnetometer. This improvement was caused by shifting the 1/f noise of the amplifier to an out-of-band frequency region, which is a classic technique, but additionally the sensor noise improved too. Whether this was mainly caused by suppressing the magnetic noise, or thermal effects on electrical properties of the sensor which is also manifested as 1/f noise, was not determined. Practical problems of utilizing HMC1001 are however relatively high power consumption and the need for costly and high power low noise amplifier, because the sensor has a low sensitivity.

LOW FREQUENCY NOISE OF ANISOTROPIC MAGNETORESISTORS IN DC AND AC-EXCITED METAL DETECTORS

J Vyhnanek, M Janosek, P Ripka

Czech Technical University in Prague, Technicka 2, 166 27 Prague, Czech Republic

E-mail: vyhnajan@fel.cvut.cz

Abstract. Magnetoresistors can replace induction sensors in applications like non-destructive testing and metal detection, where high spatial resolution or low frequency response is required. Using an AC excitation field the magnetic response of eddy currents is detected. Although giant magnetoresistive (GMR) sensors have higher measuring range and sensitivity compared to anisotropic magnetoresistors (AMR), they show also higher hysteresis and noise especially at low frequencies. Therefore AMR sensors are chosen to be evaluated in low noise measurements with combined processing of DC and AC excitation field with respect to the arrangement of processing electronics. Circuit with a commercial AMR sensor HMC1001 and AD8429 preamplifier using flipping technique exhibited 1-Hz noise as low as $125 \text{ pT}/\sqrt{\text{Hz}}$. Without flipping, the 1-Hz noise increased to $246 \text{ pT}/\sqrt{\text{Hz}}$.

1. Introduction

Magnetoresistors (MR) fall between Hall sensors and induction sensors in terms of sensitivity and noise. Unlike induction sensors, MRs have the frequency response starting from DC and they are therefore favorite sensors for non-destructive testing devices which detect deeply buried cracks [1]. MRs have small dimensions and high spatial resolution which allows to build array arrangements which can be used for metal detection and object recognition [2]. They are also readily available in commercial packaging as electronic components.

The limiting factors for these applications are the noise of the sensor, gain temperature drift, hysteresis and also offset temperature drift when sensors are used at low frequencies or DC. These parameters limit the detection depth in metal detection and non-destructive testing. Noise can be generally filtered by averaging, however this affects the speed of operation and temperature drifts become more pronounced. There are generally three competing magnetoresistive technologies: giant magnetoresistive (GMR), tunneling magnetoresistive (TMR) and anisotropic magnetoresistance (AMR) sensors. In the case of GMR and TMR, the hysteresis and noise are generally higher [3] than for AMRs, which are subject of this study.

We focus on the sensor noise which disqualifies MRs in favor of induction coils, whereas other parameters speak for MRs – they have small size with high spatial resolution and they are mass produced devices available in packages for assembly in printed circuit boards, so that they can be easily used in arrays [4]. A widely used technique of improving of the AMR sensors parameters is the so called flipping – periodic remagnetization of the sensor by applying large bipolar magnetic field pulses. With the magnetization of opposite polarity the output characteristic is reversed – “flipped”. Flipping was shown to improve the offset and gain temperature stability and to reduce crossfield



sensitivity of the sensor [5]. Metal detector noise was investigated in three possible circuit arrangements with and without flipping - their effects on AC and also DC detector noise were studied.

2. Measurement setup

For experimental measurements, AMR sensor HMC1001 (Honeywell) was used. This sensor has still the best available noise specifications from the off-the-shelf magnetoresistors. It is a barber-pole sensor with MR elements with 850 ohms resistance arranged in a full bridge, featuring on-chip flipping and compensation coils for feedback operation. The sensitivity is 140 V/T for the selected supply voltage of 5.5 V. As the sensitivity is low, the contribution of the noise of the processing electronics is not negligible. Electronics noise could be removed by the crosscorrelation technique [6], it is however not practical (speed of measurement).

The typical choice for the signal processing of an AMR bridge is a low noise instrumentation amplifier (Figure 1a). We chose AD8429 with a 1 nV/ $\sqrt{\text{Hz}}$ input voltage noise (gain = 100x) and 1.5 pA/ $\sqrt{\text{Hz}}$ current noise. Due to the high common mode of the bridge, the instrumentation amplifier cannot be set to the full voltage span therefore another amplifier with the gain 10x was connected as the last stage. A similar arrangement was evaluated in [7] where the high bridge supply of 24 V was applied in order to achieve higher sensitivity and lower noise; however 24V is impractical due to sensor heating.

AMR sensor exhibits two significant types of noise: the 1/f type magnetic noise and the white thermal noise. The white magnetic noise is still some orders of magnitude below the thermal resistive noise of the bridge elements; therefore it is not further taken into account. Whereas the 1/f noise affects low-frequency measurements and depends on the manufacturing process, the white noise influencing AC measurements can be predicted by the bridge resistance and parameters of the instrumentation amplifier.

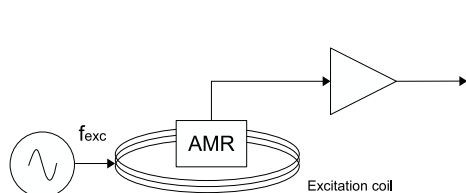


Figure 1a - Direct measurement

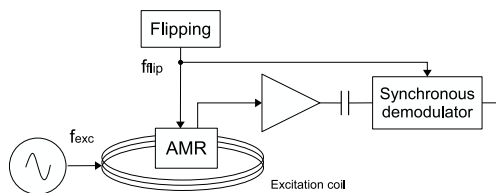


Figure 1b - Measurement setup with flipping

The commonly used method for improving the parameters of an AMR sensor is the so-called “flipping”: the sensitive magnetic layer of the AMR is remagnetized in the opposite direction, thus reducing the hysteresis and eliminating the temperature offset drift of the sensor and AC electronics.

For processing the output signal in the flipped mode where the output becomes modulated, a synchronous demodulator is used – Figure 1b. The demodulator in our case includes a switched integrator which eliminates noisy spikes in signal when the sensor is being remagnetized [3] – Figure 2a.

The noise was measured with the Agilent FFT Analyzer 35670A in all cases, without any further amplification, using DC-coupling, 100 averages and a Hanning window. The sensor together with amplifier stage was placed in a 6-layer magnetic shielding can with 100.000x attenuation of the ambient magnetic field noise.

3. Experimental results

3.1. Noise of the electronics

The noise of the electronics was evaluated by connecting a dummy bridge made of resistors of the same value as the MR elements in HMC1001 (850 Ω). Figure 2b shows the noise spectrum obtained at the output of the amplifier (input of the synchronous demodulator in Figure 2a). The 1/f noise with the equivalent of $B_E = 95 \text{ pT}/\sqrt{\text{Hz}}$ at 1 Hz (recalculated using sensitivity $S = 140 \text{ V/T}$) is dominantly due

to the instrumentation amplifier noise. The white noise with the equivalent of 30 pT/√Hz results both from the bridge thermal noise and the voltage and current noise of the instrumentation amplifier.

The expected white noise of the electronics B_{EW} can be calculated as

$$B_{EW}^2 = (SV_R)^2 + (SV_N)^2 + (SRI_N)^2 \quad (1)$$

$$B_{EW} = S \cdot \sqrt{(V_R)^2 + (V_N)^2 + (RI_N)^2} \quad (2)$$

where V_R is the resistor voltage noise, V_N is the amplifier voltage noise and I_N is the amplifier current noise.

$$B_{EW} = \frac{140V}{T} \cdot \sqrt{\left(\frac{4.12nV}{\sqrt{Hz}}\right)^2 + \left(\frac{1nV}{\sqrt{Hz}}\right)^2 + \left(\frac{1.5pA \cdot 850\Omega}{\sqrt{Hz}}\right)^2} = 31.4 \frac{pT}{\sqrt{Hz}}, \quad (3)$$

which matches the measured amplifier noise in Figure 2 (b).

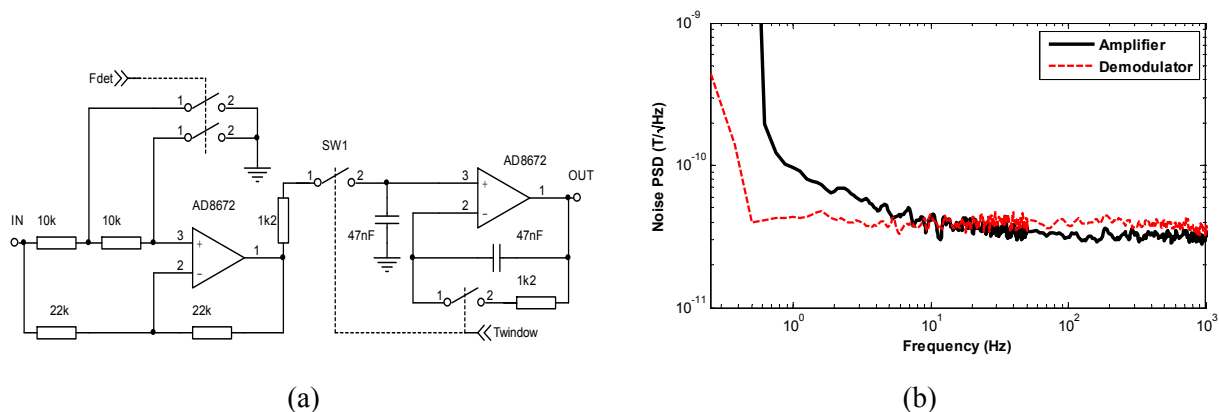


Figure 2. Synchronous demodulator schematics (a) and comparison of noise of the electronics at amplifier output and demodulator output (b)

The noise of synchronous demodulator was measured at the demodulator output with a 10-kHz reference and the same dummy resistor bridge. The spectrum shows an increased white noise level of 40 pT/√Hz. This was identified as the effect of the switched integrator used in the windowing circuit with the time window set to 70%. With the time window of 100%, the white noise level was 32 pT/√Hz. In the demodulator spectrum there is no 1/f noise of the instrumentation amplifier, due to the fact, that the frequency range was shifted by the 10-kHz demodulation frequency.

Knowing the electronic noise, the noise measurements were done using three different circuit arrangements.

3.2. Direct measurement

This arrangement with simple electronics is depicted in Figure 1a. The output of the AMR bridge is directly amplified. It has the full frequency span limited only by the corner frequency of the amplifier stage. The eventual feedback compensation, which eliminates gain drift and improves linearity, can be realized with a single-opamp PI controller. In this case, the 1/f sensor noise was dominating, the total noise value $B_{N1} = 246$ pT/√Hz at 1 Hz (Figure 3b).

From the measured values, we can estimate the 1-Hz noise of the sensor itself (B_{S1}) as

$$B_{S1} = \sqrt{B_{N1}^2 - B_{E1}^2} = \sqrt{246^2 - 95^2} \frac{pT}{\sqrt{Hz}} = 226 \frac{pT}{\sqrt{Hz}} \quad (4)$$

This result is in agreement with values published in [5]. The 1-kHz white noise, which would dominate in the AC application, is approx. the same as the electronic noise - 32 pT/ \sqrt{Hz} .

If we use this mode, a single remagnetizing pulse should be performed at least while switching on the device to assure the magnetic state of the sensor.

3.3. Modulation – flipping

The block diagram is shown in Figure 1b, the flipping current and output waveform are shown in Figure 3a. By using flipping at 10 kHz with peak-to-peak amplitude of 3.6 Amps, the output signal was modulated and shifted to the white-noise frequency range of the instrumentation amplifier. The resulting noise of 125 pT/ \sqrt{Hz} at 1 Hz (Figure 3b) makes flipping the obvious choice for precise DC field measurements, avoiding the offsets and 1/f noise of the instrumentation amplifier. When compared to 1/f noise of the amplifier and non-flipped sensor (4), the noise clearly further decreased: flipping improved also the low-frequency noise of the magnetoresistor.

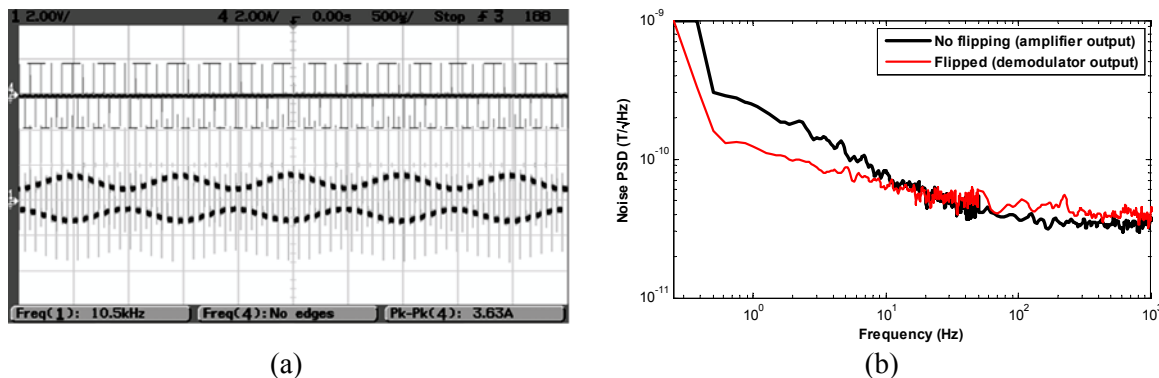


Figure 3 – Modulated output signal of flipped AMR (a) and comparison of overall noise with direct measurement (b)

However, flipping is power-demanding as the narrow current pulses have to have an amplitude of several amperes in order to properly magnetize the sensitive layer and reduce the 1/f noise [5]. The maximum allowed power dissipation allows maximum flipping frequencies in the order of tens of kHz, limiting the measuring frequency range. It is however possible to use a lower flipping frequency and higher excitation frequency.

3.4. D. Sensor as rectifier

A flipped sensor can be used as a rectifier [8], basic block diagram is presented in Figure 4a. If the flipping frequency is derived from the excitation frequency, the excitation signal is synchronously rectified and the output signal looks like in Figure 4b. The excitation frequency is evaluated with a simple low pass filter connected to the output of the amplifier stage, thus eliminating complex detection circuitry.

A simple feedback compensation is however possible only for a DC range, therefore the sensor should be positioned perpendicularly to the excitation field [1]. However a disadvantage is that the offset drift and the 1/f noise of the amplifier are not eliminated even at the excitation frequency f_{exc} .

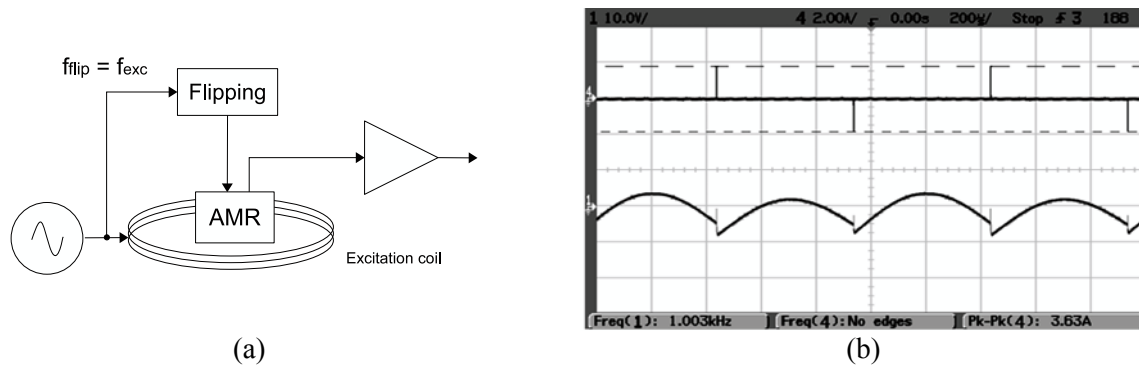


Figure 4- Special arrangement with $f_{\text{flip}}=f_{\text{exc}}$ (a), and the flipping current (upper trace) and amplified sensor output (lower trace) (b)

4. Conclusion

When the AMR-based metal detector works with an AC excitation field to sense the eddy current response of metal objects and only the AC frequency response is evaluated, then the noise level is determined by the sensor white noise level and it is approximately the same for either direct measurement or for flipping with demodulator– the 1-kHz noise was about $30 \text{ pT}/\sqrt{\text{Hz}}$ in both circuit arrangements.

For DC measurements, the $1/f$ noise of the amplifier and offset drifts of the sensor are best suppressed by flipping modulation technique. For the HMC1001 AMR sensor with $5.5 \text{ V}_{\text{DC}}$ bridge supply and 10-kHz flipping frequency, we have found an improvement from $246 \text{ pT}/\sqrt{\text{Hz}}$ 1-Hz noise with direct measurement down to $125 \text{ pT}/\sqrt{\text{Hz}}$ when using flipping with appropriate demodulation. This improvement was found to be larger than simple effect of shifting the modulated signal out of $1/f$ amplifier noise: flipping was found to further improve the sensor low-frequency noise.

The commonly used flipping method is however power-demanding with complicated detection electronics; also the measuring frequency range is limited, which is a difficulty in NDE. The possibility of using $f_{\text{flip}}=f_{\text{exc}}$ was thus investigated: while it allowed to reduce flipping power and to simplify signal processing circuitry, the $1/f$ noise of the amplifier was however present in this case.

References

- [1] Jander A, Smith C, Schneider R 2005 Magneto-resistive sensors for nondestructive testing and evaluation *Proc. SPIE*. vol. 5770 p. 1-13
- [2] Wold RJ, Nordman CA, Lavelly EM, Tondra M, Lange E, Prouty M 1999 Development of a handheld mine detection system using a magneto-resistive sensor array, *Proc. SPIE* vol. 3710 pp. 113-123
- [3] Popovic RS, Drljaca PM, Schott C 2002 Bridging the gap between AMR, GMR, and Hall magnetic sensors *Proc. 23rd Int. Conf. On Microelectronics* vol. 1 pp. 55-58
- [4] Vyhnánek J, Janosek M, Ripka P 2012 AMR Gradiometer for Mine Detection, *Sensors and Actuators*, vol. 186, pp. 100-104
- [5] Hauser H, Fulmek PL, Haumer P, Vopálenský M, Ripka P 2003 Flipping field and stability in anisotropic magneto-resistive sensors *Sensors and Actuators*, vol. 106, pp. 1-3
- [6] Stutzke NA, Russek SE, Pappas DP 2005, Low-frequency noise measurements on commercial magneto-resistive magnetic field sensors *J. Appl. Phys.*, vol. 97, pp. 10Q107
- [7] He DF, Tachiki M, Itozaki H 2009, Highly sensitive anisotropic magneto-resistance magnetometer for Eddy-current nondestructive evaluation, *Review of Scientific Instruments*, vol. 80, pp. 036102-1 - 036102-2
- [8] Tumanski S 2001, Thin film magneto-resistive sensors (IOP Publishing), pp. 78-79

3.1.3 Crossfield response of industrial magnetic sensors

This work compares crossfield sensitivity of the commercial AMR sensor HMC1001 and integrated fluxgate sensor DRV425. Crossfield is the component of magnetic field which is perpendicular to the sensitive axis. Sensitivity of a sensor to crossfield is therefore a parasitic effect. AMR sensors are especially sensitive to crossfield due to their fundamental principle, if feedback is not used.

However, there is a limit, where remanent magnetization of the sensing element loses its single-domain state, even with feedback. The state then has to be restored by a flipping pulse. The absolute maximum crossfield which the HMC1001 can withstand, is $\pm 380 \mu\text{T}$ (Fig. 7 in the paper), whereas the DRV425 can withstand at least 10 mT with minimum influence on the sensor characteristic.

Crossfield response of industrial magnetic sensors

Pavel Ripka*, Jan Vyhnanek and Andrey Chirtsov

Faculty of Electrical Engineering, Czech Technical University, Technicka 2, Czech Republic

Abstract. Magnetic sensors used for non-destructive testing, metal detection and other applications are subjected to large perpendicular field. In this paper we show that the existing models describing the response of anisotropic magnetoresistors (AMR) cannot be used for fields larger than the critical value, which is $350 \mu\text{T}$ for the Honeywell HMC1001. This critical value is one order of magnitude lower than the anisotropy field and it is decreasing with increased value of the measured field. From our findings it is clear that AMR sensors cannot be safely used in applications in which fields above $250 \mu\text{T}$ can appear. Neither flipping, nor feedback compensation can compensate for this error. We show that this behaviour is caused by the fact that the single-domain state of the AMR is broken at the mentioned critical field. Compared to that, fluxgate sensors including microfluxgates are by principle immune against the crossfield. Unlike in AMR, crossfield sensitivity in fluxgate sensors is second-order effect, which can be kept under control by proper design. We show that even crossfield of 10 mT does not cause significant degradation of the sensor precision.

Keywords: Magnetic sensors, crossfield sensitivity

1. Introduction

Non-linear response to the magnetic field perpendicular to the sensing direction is unwanted property of all magnetic sensors which contain ferromagnetic material [1]. This so called crossfield response can cause serious error of compass, gradiometer or current sensor.

In this paper we discuss crossfield resistance of AMR sensors and integrated fluxgate in the wider field range. Electromagnetic inspection methods often use strong AC or DC excitation field and very small field deviation caused by the defect is observed in perpendicular direction [2,3]. In such case the crossfield response can cause significant error.

Theoretical response is compared to the measured results. The crossfield response was measured by two sets of the Helmholtz coils, one generating field in the sensitive axis of the tested sensor, the other perpendicular. Ferromagnetic objects which could deform the magnetic field or cause nonlinearity were removed from the vicinity of the test setup. Each characteristics was measured several times to check repeatability; the data were not averaged, but they are shown in the same plot. The perpendicularity of the crossfield coil was adjusted to give minimum response. The residual linear response was corrected in the collected dataset.

*Corresponding author: Pavel Ripka, Faculty of Electrical Engineering, Czech Technical University, Technicka 2, 166 27 Praha 6, Czech Republic. Tel.: +420 736 760 601; E-mail: ripka@fel.cvut.cz.

2. AMR sensors

Crossfield sensitivity is inherent for all AMR sensors [4]. For the compass based on the unflipped Honeywell HMC 1001 the azimuth error caused by crossfield is 1 deg.

The crossfield is in the easy direction of the sensor permalloy stripe magnetization, so AMR sensors are very sensitive to it.

The basic equation for the response of the barber-pole sensor bridge is [5]

$$R = R'_0 + \Delta R \frac{H_y}{H_x + H_0} \sqrt{1 - \left(\frac{H_y}{H_x + H_0} \right)^2} \quad (1)$$

In [4] we have used simplification for $|H_x|, |H_y| \ll |H_0|$ and we finally arrived to

$$V_1 = \frac{aH_y}{H_x + H_0} \quad (2)$$

where: H_x is the crossfield; H_y is the measured field; H_0 is the (constant) anisotropy field; a is the sensitivity constant.

The anisotropy field for Honeywell HMC1001 is $H_0 = 0.8$ mT. Increasing H_0 leads to suppression of the crossfield effect, but also to the decrease of sensitivity, which is accompanied by the increase of the magnetic field sensor noise.

Many AMR sensors are stabilized by flipping, i.e. reversing the remanent magnetization of the magnetic layer by applying SET/RESET pulses into the flipping coil. Flipping pulses should have large amplitude to restore single-domain state of the sensor core [6]. The flipping field has the same direction as the crossfield. In [4] we have shown that flipping reduces sensitivity to crossfield. Later in this paper we will show that this is limited to small fields.

Mohamadabadi et al. [8] used more precise approximation of the AMR equations

$$V_1 = \frac{aH_y}{\sqrt{(H_x + H_0)^2 + H_y^2}} \quad (3)$$

and they developed and experimentally verified correction method which reduces the crossfield error without flipping by the factor of 8, and with flipping by the factor of 9. The problem of the mentioned correction methods is that they work only at small fields and they also require two or three sensors.

For perpendicular field larger than $200 \mu\text{T}$ the AMR sensors exhibit loss of sensitivity. Figure 1 shows the characteristics of the HMR2003 AMR module which is based on HMC1000 sensors. The flipping was switched-off and the characteristics was measured for several values of the crossfield. Applying crossfield has similar effect as increasing H_0 : the sensitivity is decreased and the full-scale range is increased. This behaviour seems to be useful for increasing of the sensor range more effectively than using offset stripe, which has only 50 mA/G field factor.

However, for practical situations this mode fails when the flipping is on, as shown in Fig. 2. When the flipping is applied, the sensor output polarity is periodically changing. The sensor output is therefore processed by synchronous detector controlled by the flipping signal. Two subsequent readings are subtracted giving double sensitivity.

For small crossfield the small field sensor characteristics is not affected, as the SET/RESET pulses erase the crossfield effect. The large field response is no longer reversed by flipping, which results in the sensor sensitivity falling to zero. Thus the claim that flipping increases the AMR sensors stability [8] is valid only for small field range.

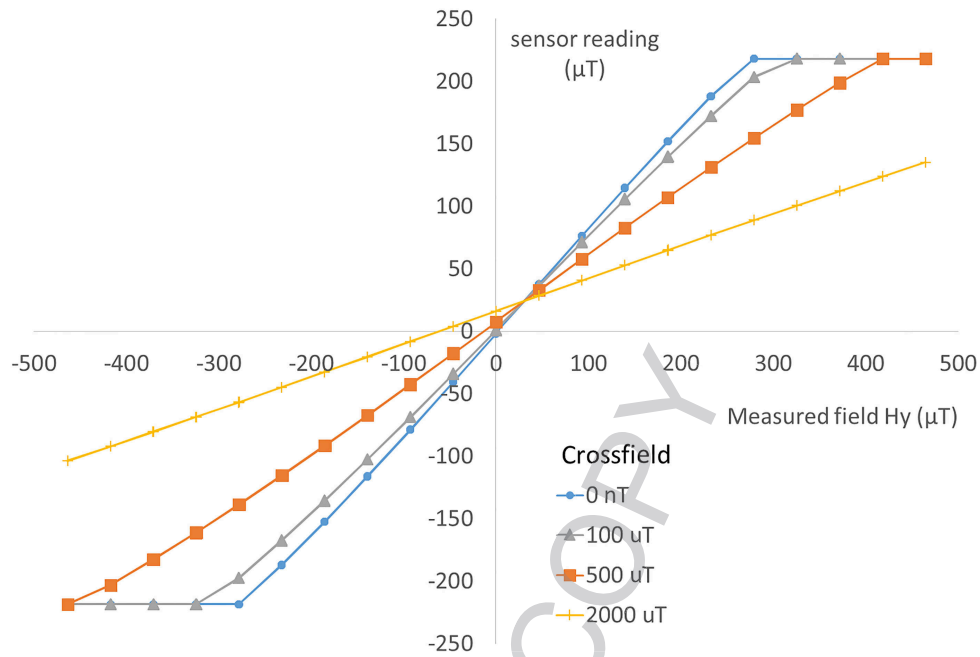


Fig. 1. AMR magnetometer characteristics for several values of the crossfield. Measured without flipping.

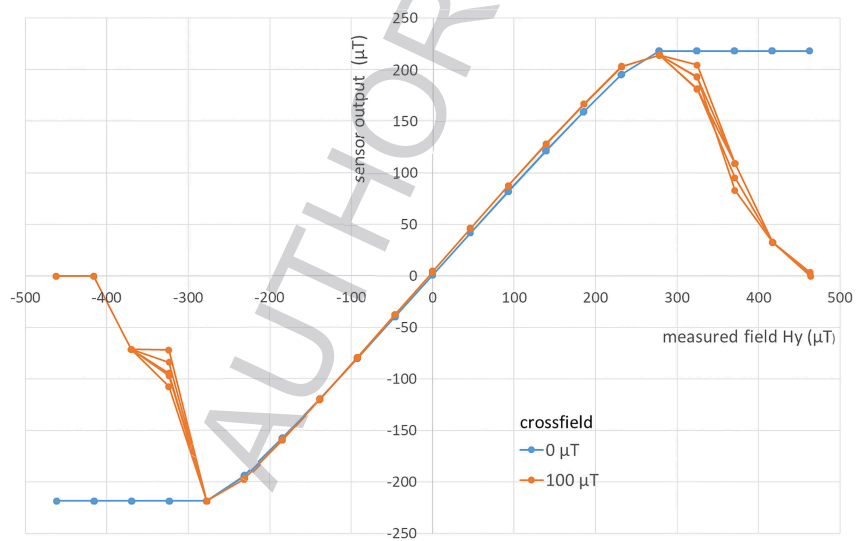


Fig. 2. Characteristics of the flipped AMR sensor without and with 0 μT crossfield.

The flipped sensor response is dramatically changed for larger crossfield values. This situation is illustrated by Fig. 3. The crossfield of $H_x = 250 \mu\text{T}$ is here so large, that flipping cannot fully reverse the core magnetization. For crossfield of $H_x = 500 \mu\text{T}$ the magnetisation is constant, regardless the polarity of the flipping pulse. The detector output is therefore zero.

If we look on the sensor output as a function of the crossfield, we finally observe the hysteresis, indicating that the sensor magnetic core is no longer in the single-domain state. Figure 4 shows the

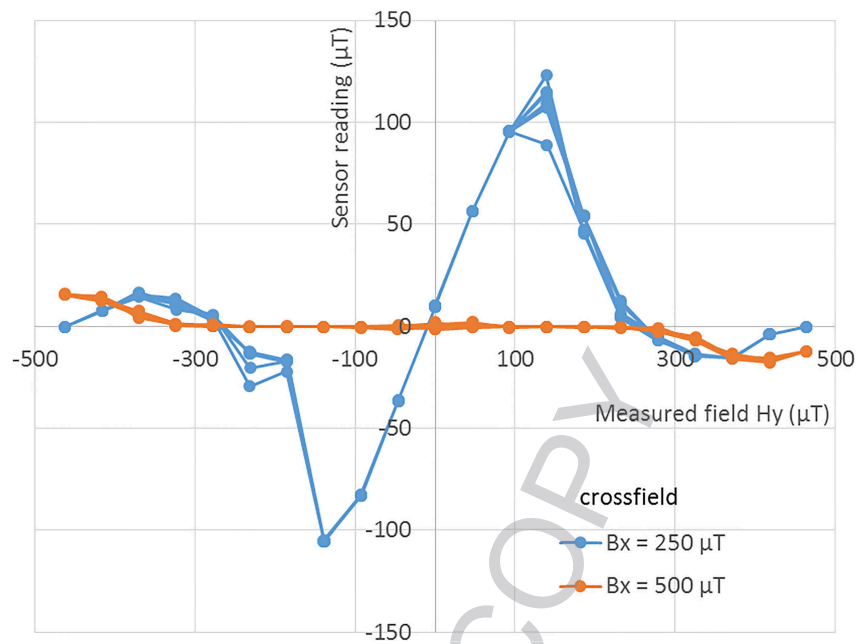


Fig. 3. Characteristics of the flipped AMR sensor with 250 μT and 250 μT crossfield.

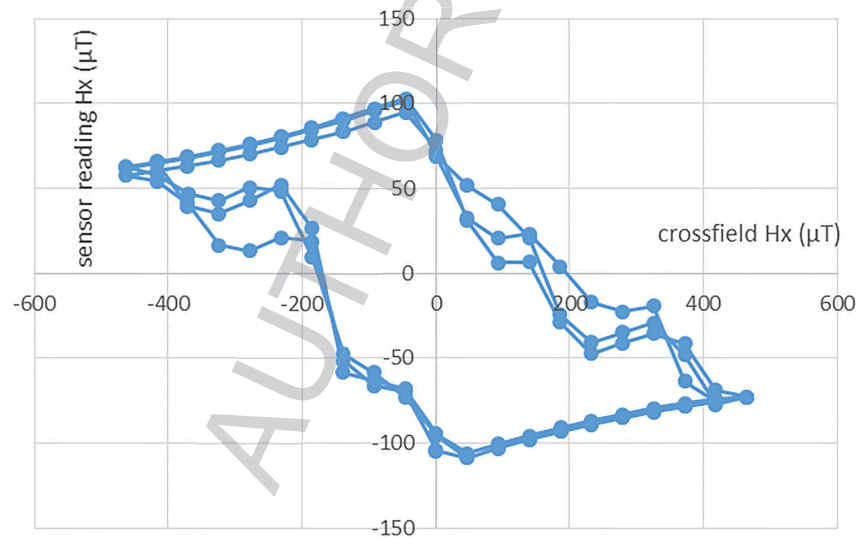


Fig. 4. Sensor output as a function of crossfield for small value of the measured field $H_y = 50 \mu\text{T}$ (no flipping).

sensor output as a function of crossfield for small values of the measured field H_y . For every field value in the measuring direction $H_y < 200 \mu\text{T}$, the response is very similar.

For larger H_y the hysteresis starts to decrease as shown in Fig. 5 and for $H_y = 0.7 \text{ mT}$ the hysteresis disappears – in the presence of the large field component the magnetization process in the strip longitudinal direction becomes rotational, this means that the hard and easy axes are now flipped. This state is interesting, but it can hardly have any practical applications.

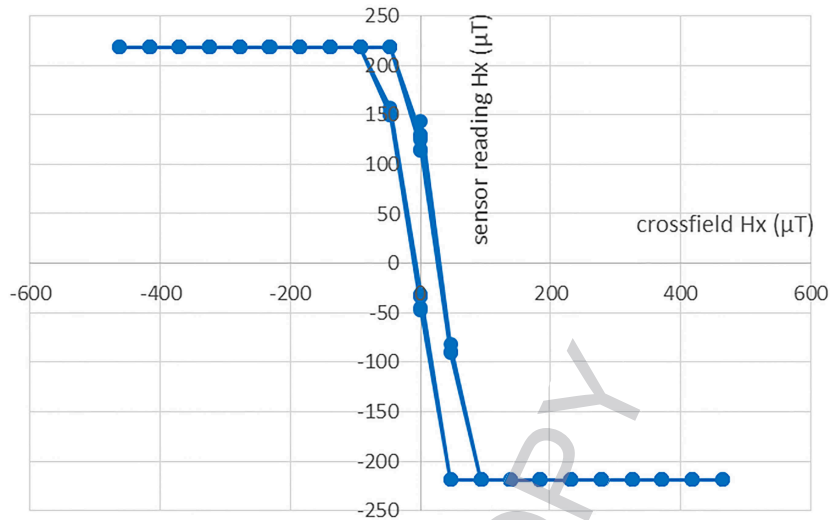


Fig. 5. AMR sensor output as a function of crossfield for very large value of the measured field $H_y = 500 \mu\text{T}$ (no flipping).

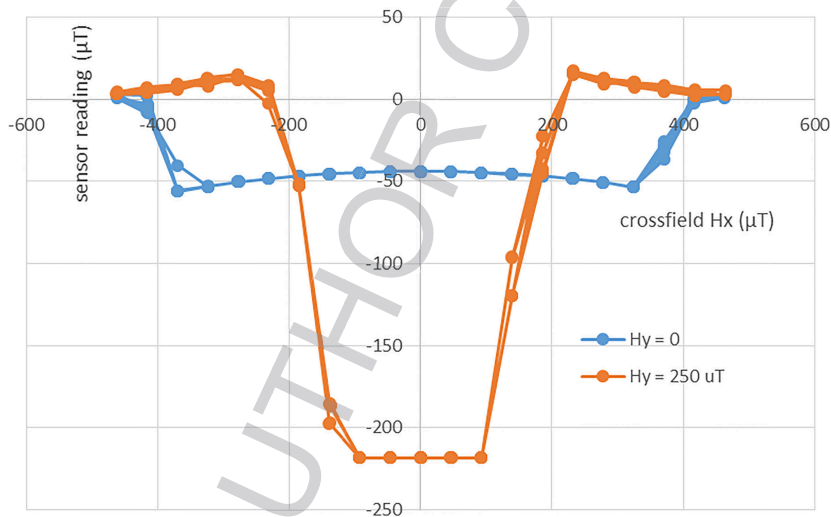


Fig. 6. Output of the flipped AMR sensor as a function of the crossfield for $B_y = 0$ and $B_y = 250 \mu\text{T}$.

The same dependence for the flipped sensor is shown in Fig. 6 confirming that in this case the critical field is about $350 \mu\text{T}$ for zero measured field, but only $100 \mu\text{T}$ for the maximum measured field of $250 \mu\text{T}$.

We may conclude that AMR sensors are very sensitive to crossfield larger than the critical value, which is about $350 \mu\text{T}$ for the Honeywell HMC1001. It should be noted that this critical value is one order of magnitude lower than the anisotropy field H_0 . This value is decreasing with increased value of the measured field H_y .

For larger values of the crossfield the sensor characteristics are heavily distorted due to the fact that the single-domain state is broken. However, some reading is still possible for sensor with no flipping. Once the flipping is on, the sensor output is useless.

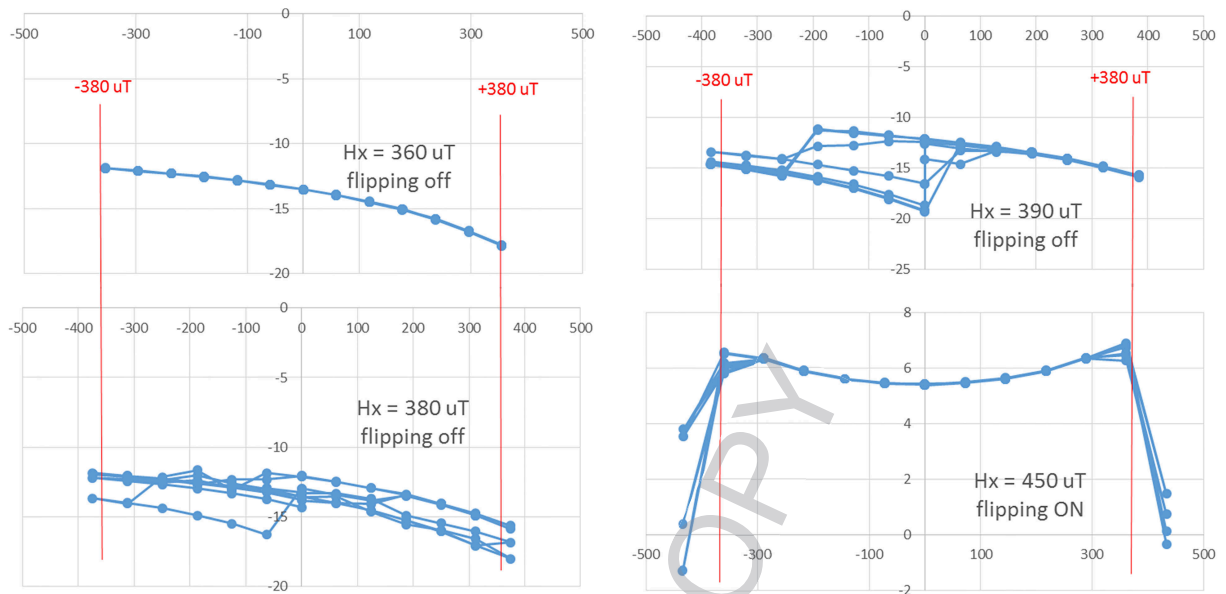


Fig. 7. Sensor response for slowly increasing value of the crossfield H_x .

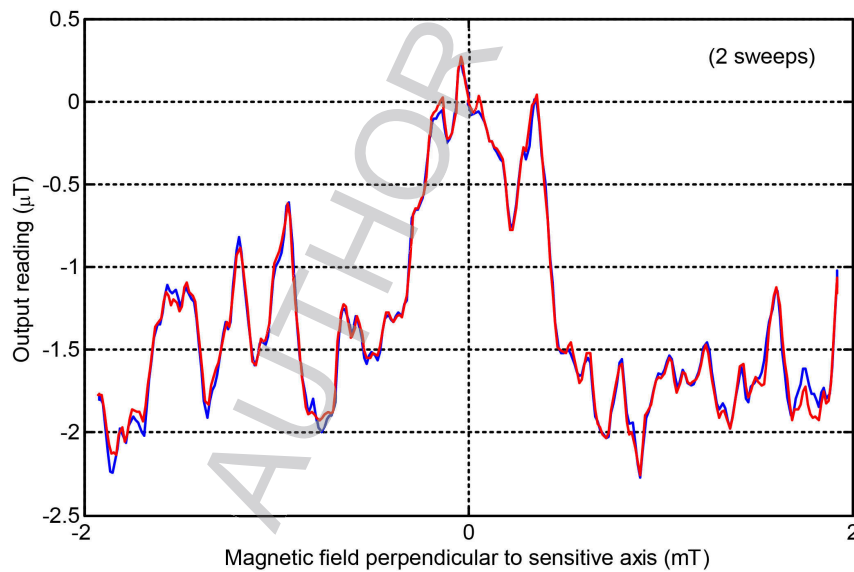


Fig. 8. Crossfield sensitivity of the integrated fluxgate DRV 425.

The exact value of the critical crossfield is clear from Fig. 7. The measured field H_x was kept zero and the response to the crossfield was measured, while the amplitude of the crossfield was slowly increased. The figure shows that for $H_x = 370 \mu\text{T}$ the response is nonlinear (as expected), without any hysteresis. The onset of hysteresis signalling first closure domains appeared at $H_x = 380 \mu\text{T}$, which corresponds to drop of the sensitivity of the flipped sensor (Fig. 6). With increasing maximum H_x the hysteresis rapidly increases.

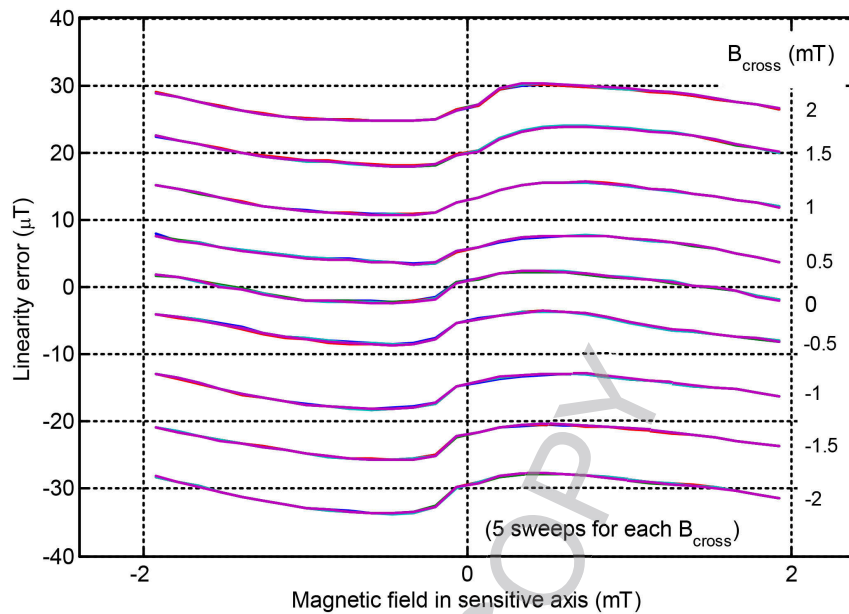


Fig. 9. Linearity error of the integrated fluxgate DRV 425. The curve parameter is the crossfield.

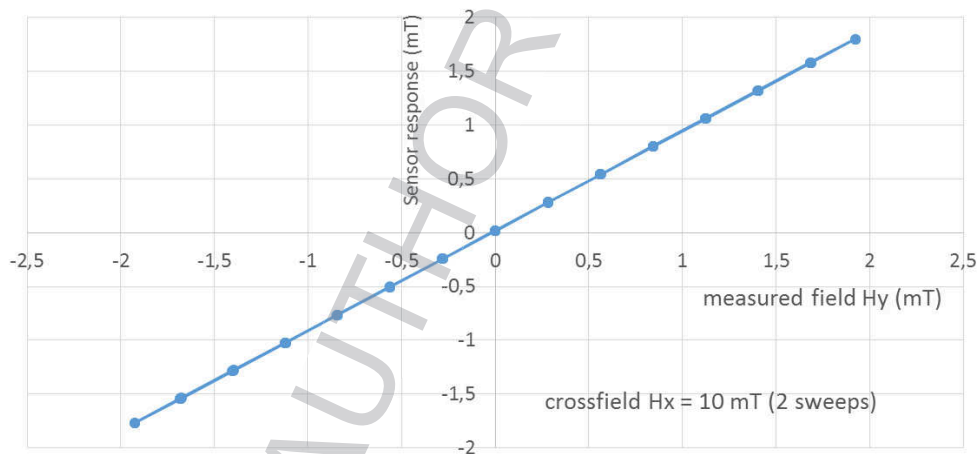


Fig. 10. DRV425 sensor response for the crossfield of $H_x = 10$ mT.

3. Fluxgate sensors

Crossfield was reported also for fluxgate sensors. First it was observed on the data from the Magsat magnetometer and verified by measurement and simulations [9].

In general, the effect of the crossfield is suppressed by high demagnetization factor in the direction perpendicular to the sensing axis [10]. Sensors with stripe or racetrack cores are therefore more resistant to the crossfield than ring-core sensors.

For the PCB fluxgate the crossfield error was 0.3%. Crossfield in fluxgate is a second-order error. It is caused by core non-homogeneity and imperfections in the geometry of the core and windings [11].

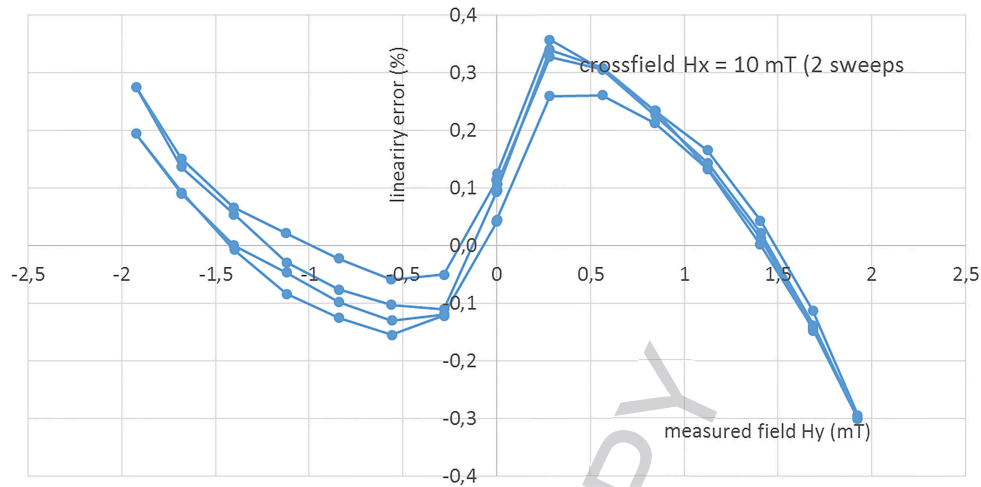


Fig. 11. DRV linearity error for the crossfield of $H_x = 10$ mT.

However, crossfield effect was not examined in the wider field range and it was never measured on microfabricated sensors.

Microfabricated fluxgates appeared recently. They replace the CMOS-based fluxgates with flat coils, which had poor coupling between the coil and core. Lu used microfabricated solenoid coils for excitation and flat coils for pick-up. The core was formed by two stripes [12]. Rectangular closed-core fluxgate of this type having solenoid coils both for excitation and pick-up was described in [13]. Closed core has an advantage in better excitation efficiency leading to lower perming and lower power consumption, but it is more sensitive to crossfield than the rod-type core.

We made our measurements on DRV 425 integrated fluxgate manufactured by Texas Instruments [14]. This sensor has open core formed by dual permalloy stripes of about 1 mm length. The device model was described in [15]. Internal signal processing is analog, which is still giving better results than digital fluxgates such as described in [16].

Figure 8 shows that the TI DRV 425 integrated fluxgate has only 0.1% crossfield error for perpendicular fields up to 2 mT. The crossfield of this magnitude has no effect on the sensor linearity error which is also 0.1% as shown in Fig. 9. For the crossfield of this magnitude AMR sensors completely fail. Even for the crossfield of $H_x = 10$ mT the response of this sensor has only 0.1% hysteresis and the linearity error of 0.4% as seen in Figs 10 and 11.

4. Conclusions

AMR sensors are by principle sensitive to crossfield, but if the total applied field is small (below $100 \mu\text{T}$ for Honeywell HMC 1001), this sensitivity can be suppressed by feedback, flipping or by calculation. For larger fields the crossfield error becomes dramatic and due to non-linearity it cannot be compensated. As a result, barber-pole AMR sensors cannot be used in applications in which fields above $250 \mu\text{T}$ can be present.

Compared to that, fluxgate sensors including microfluxgates are by principle immune against the crossfield. Unlike in AMR, crossfield sensitivity in fluxgate sensors is second-order effect, which can be kept under control by proper design.

The high crossfield resistance of the integrated fluxgate is caused by

1. High homogeneity of the deposited magnetic core compared to amorphous tapes
2. Geometrical accuracy of the sensor core and windings thanks to the microfabrication technology
3. High demagnetisation factor of the stripe cores in the crossfield direction.

We show that even crossfield of 10 mT does not cause significant degradation of the sensor precision.

High crossfield resistance allows to use the microfabricated fluxgate sensor in the vicinity of permanent magnets (for position sensing) and strong electric currents (for current sensing in multiphase systems). The compass error caused by the measured crossfield error would be below 0.1 deg. Crossfield resistance is also required for applications based on eddy-currents such as non-destructive testing and distance sensing of conductive objects.

Acknowledgments

This work was supported by the Grant Agency of the Czech Republic through the project “New methods for the measurement of electric currents” (GACR 17-19877S).

References

- [1] P. Ripka, M. Janosek, M. Butta, S.W. Billingsley and E. Wakefield, Crossfield error in fluxgate and AMR sensors, *Journal of Electrical Engineering* **61**(7) (2010), 13–16.
- [2] A. Fujii, T. Adachi and Y. Gotoh, Examination of inspecting method of opposite side defect in steel plate using AC and DC magnetic field, *International Journal of Applied Electromagnetics and Mechanics* **52**(3–4) (2016), 1045–1052,
- [3] Y. Sun, Z. Ye, G. Yang, D. Li, S. Liu, Y. Kang, M. Gu and C. Liu, Pulsed electric flux leakage (PEFL) techniques for defects detection and characterization, *International Journal of Applied Electromagnetics and Mechanics* **52**(3–4) (2016), 1099–1106.
- [4] J. Kubik, J. Vcelak and P. Ripka, On Cross-Axis Effect of the Anisotropic Magnetoresistive Sensors, *Sensors & Actuators A* **129** (2006), 15–19.
- [5] Tumanski: Thin Film Magnetoresistive Sensors, IoP Publ, 2001, p. 17–27.
- [6] P. Ripka, M. Janosek and M. Butta, Crossfield Sensitivity in AMR Sensors, *IEEE Trans. Magn.* **45** (2009), 4514–4517.
- [7] H. Hauser, P.L. Fulmek, P. Haumer, M. Vopalensky and P. Ripka, Flipping field and stability in anisotropic magnetoresistive sensors, *Sensors & Actuators A* **106** (2003), 34–37, 121–125.
- [8] K. Mohamadabadi, Ch. Coillot and M. Hillion, New Compensation Method for Cross-Axis Effect for Three-Axis AMR Sensors, *IEEE Sens. J.* **13** (2013), 1355–1362.
- [9] P. Brauer et al., Transverse effect in fluxgate sensors, *Sens. Actuators A* **59** (1997), 70–74.
- [10] P. Ripka and W. Billingsley, Crossfield effect at fluxgate, *Sensors and Actuators A* **81** (2000), 176–179.
- [11] M. Janosek, M. Butta and P. Ripka, Two sources of cross – field error in racetrack fluxgate, *J. App. Phys.* **107** (2010), 09E713.
- [12] C.-C. Lu, W.-S. Huang, Y.-T. Liu and J.-T. Jeng, Design, Fabrication, and Characterization of a 3-D CMOS Fluxgate Magnetometer, *IEEE Trans. Magn.* **47** (2011), 3752–3756.
- [13] C. Lei, Y. Liu, X.-C. Sun, T. Wang, Z. Yang and Y. Zhou, Improved Performance of Integrated Solenoid Fluxgate Sensor Chip Using a Bilayer Co-Based Ribbon Core, *IEEE Sens. J.* **15** (2015), 5010–5015.
- [14] M.F. Snoeij, V. Schaffer, S. Udayashankar and M.V. Ivanov, Integrated Fluxgate Magnetometer for Use in Isolated Current Sensing, *IEEE Journal of Solid-State Circuits* (51), 1684–1694, doi: 10.1109/JSSC.2016.2554147.
- [15] G. Gaskill Steven, Weisshaar Andreas: Compact Equivalent Circuit Modeling of Microfluxgate Devices With Thin-Film Magnetic Cores, *IEEE Trans. Magn.* **52** (2016), Article #: 4002808.
- [16] M. Kashmiri et al., A 200 kS/s integrated-fluxgate differential magnetic-to-digital converter with an oversampling compensation loop for contactless current sensing, in IEEE ISSCC Dig. Tech. Papers, 2015, pp. 490–491.

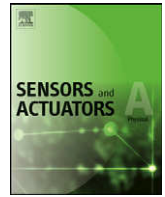
3.2 Applications

In the following chapters, commercial AMR and integrated fluxgate sensors were used in magnetometers with AC magnetic field excitation to fulfill the objectives (I.) and (III.) of the thesis. The decisive criteria for selecting the AMR sensors were their flat frequency response starting from DC, simple final assembly and relatively low cost. The papers address construction of gradiometers and sensor arrays and signal processing with considerations of practical applications for mine detection and visualization of concealed metallic building structures (chapters 3.2.1, 3.2.2, 3.2.3). Next, a proximity sensor with AMR is described in chapter 3.2.4. This paper fully exploits the advantages of the AMR sensors over induction sensors by low frequency operation and inherent demodulation feature of the AMR sensors. For these four papers, I designed the necessary hardware and did the processing of measured data within the framework of projects managed by Dr. Janošek, Prof. Ripka and Dr. Včelák. A linear position sensor with commercial integrated fluxgate sensors is described in chapter 3.2.5., which is related to the objective (II.b.). The integrated fluxgate sensors DRV425 introduced in 2015 bring the benefit of the ± 2 mT input range and on-chip conditioning circuit. I participated on design of the sensor hardware and testing platform. And finally, an application of DC field mapping is presented in chapter 3.2.6, where I performed the measurements and data processing, and which is partially related the objective (III.).

3.2.1 AMR Gradiometer for Mine Detection

Development of an AMR gradiometer is presented here. The goal of this work was to develop a sensor suitable for sensor arrays with focus on low noise operation due to the intended application for mine detectors.

The gradiometer is sensitive to DC and AC fields. Using an external excitation field, the eddy current response of metal objects can be measured together with the induced magnetic field of ferrous objects which have substantial permeability. The frequency of the excitation field is 1 kHz and it is already at the upper limit of the gradiometer frequency range; lower excitation frequency would result in lower eddy current response. However the response to the induced magnetic field due to permeability in ferrous objects shows minimum dependence with frequency. Flipping frequency of 30 kHz limits the gradiometer bandwidth, because further increase of the flipping frequency is restricted by the maximum power dissipation of the employed AMRs. Amplitude resolution of the gradiometer is limited by the noise of KMZ51 magnetoresistors which is for one piece of this type $3.1 \text{ nT}/\sqrt{\text{Hz}}$ at 1 Hz and $268 \text{ pT}/\sqrt{\text{Hz}}$ at 1 kHz. Based on the estimated limits of the proposed gradiometer, this work gave rise to papers on characterization of sensors in chapter 3.1 in subsequent years.



AMR gradiometer for mine detection

Jan Vyhnánek*, Michal Janošek, Pavel Ripka

Czech Technical University in Prague, Faculty of Electrical Engineering, Dept. of Measurement, Technická 2, 166 27 Prague, Czech Republic

ARTICLE INFO

Article history:

Received 6 October 2011

Received in revised form 10 February 2012

Accepted 2 March 2012

Available online 29 March 2012

Keywords:

Mine detection
Magnetic sensors
AMR
Gradiometer
Eddy currents

ABSTRACT

Anisotropic magnetoresistors (AMRs) are used to build an advanced mine detector. The sensing head involves a gradiometric pair of AMR sensors and a continuous-wave driven excitation coil, so the gradiometer is capable of detection of ferromagnetic materials as well as diamagnetic metals. The sensors are specially arranged to suppress the large AC-excitation field, so the mine detector senses both DC and AC field gradient responses of the object of interest. Being limited by the sensor and electronics noise of 268 pT/ $\sqrt{\text{Hz}}$ at 1 kHz, we were able to detect a 50 mm \times 50 mm \times 1.5 mm aluminum test object in a 20 cm depth using a 150 μT , 1-kHz excitation field.

© 2012 Elsevier B.V. All rights reserved.

1. Introduction

Mine detectors used for clearing landmines and other explosive remnants are in most cases specialized metal detectors constructed to reveal even minimum metal mines in electromagnetically difficult soils. They are nearly exclusively based on eddy currents and use induction coils for sensing the metallic parts of mines. They detect conducting objects very reliably, but they fail to discriminate dangerous objects from the scrap metal. The work of deminers is often very slow, as they have to carefully excavate each concealed metal object [1].

To distinguish metal parts of mines from other metal objects the AMR gradiometer uses sensors with high spatial resolution to discriminate objects by the recognition of their shape and dimensions. This process requires scanning, which is however already performed by deminers naturally by sweeping a detector head from side to side while searching for mines. For the effectivity of the scanning process multiple sensor array should be used, as was demonstrated by non-destructive testing systems [2,3]. Sensing both DC and AC magnetic field response should contribute to better characterization of the object. Even when some parts of a ferromagnetic object have corroded and lost its conductivity, they still can be detected by steady-state magnetic fields.

The proposed gradiometer benefits from the simple design of commercially available AMR sensors and printed circuit board (PCB) technology. It can operate with a 1-kHz continuous-wave

excitation field, so non-magnetic metals can be detected in the AC part of the gradiometer output in addition to ferromagnetic metals that affect the DC part. The gradiometric arrangement allows to measure the weak gradient field of the object of interest, while suppressing the strong excitation and Earth's field.

A similar mine detector with spin dependent tunneling sensors (SDT) was presented in [4], however it worked with a pulsed field and the DC noise of the SDT sensors disqualifies them from the combined DC and AC response sensing. An AMR sensor working with a harmonic excitation field was used for non-destructive testing [5] and dealt with reduction of the sensor noise as the main factor limiting the sensitivity, but it did not solve the suppression of the Earth's magnetic field needed for the DC gradient sensing.

2. Gradiometer principle

AMRs of the KMZ51 type (NXP, ex. Philips) are thin-film permalloy sensors with magnetoresistive elements configured in a full bridge and with the on-chip flipping and compensation coil. They detect the magnetic field component along the sensitive axis, the sensitivity reaches up to 130 mV/(A/m) for the maximum 8-V bridge supply. Two AMRs are arranged in the distance of 40 mm, forming a vertical dB_x/dx gradiometer (Fig. 1). The two gradiometric sensors in a SO-8 package are soldered on the PCB together with signal preamplifiers (total gain of 1000 \times).

As a proper mine detector needs to sense diamagnetic metals too, we added a continuous-wave driven excitation coil and solved the most difficult part of suppressing the large excitation field, which is needed for the proper detection depth. The coil is symmetric to the gradiometric sensors and it is fed with a 1-kHz

* Corresponding author.

E-mail address: vyhnajan@fel.cvut.cz (J. Vyhnánek).

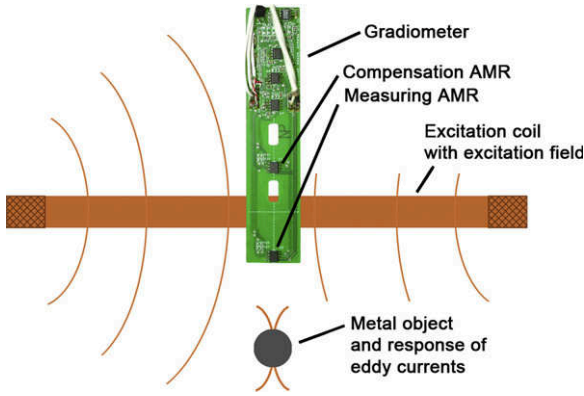


Fig. 1. Gradiometer combined with the excitation coil form the detector head. The compensating and measuring sensors of the gradiometer are symmetrically placed on both sides of the excitation coil.

harmonic signal resulting in an AC field of about $150 \mu\text{T}$ amplitude. The first (measuring) AMR sensor is located on the sensitive side of the detector head and experiences the same excitation magnetic field as does the second (compensation) sensor. Without any deformation of the excitation or Earth's field the gradiometer response is near zero, limited by the gain of the PI controller in the feedback loop (Fig. 2).

Choosing the coil diameter is not a simple task: for a given excitation current, a small coil provides stronger magnetic fields to a small distance, while a larger coil delivers weaker fields to greater distances. Coils with the diameter in the range of centimeters are used in non-destructive testing for the detection of small near-surface cracks in metals [6,7], while a coil of 1-m diameter is employed for the detection of large deeply buried bombs [1]. The selected diameter of 27 cm is a compromise and should be suitable for both minimum metal mines and bombs close to the surface; this coil diameter is also common to commercial mine detectors.

3. Gradiometer circuitry

In order to assure the magnetic state of the AMR sensors and to improve the stability of its parameters, the AMR sensors are periodically remagnetized – “flipped” at 30 kHz. The sensor field response becomes modulated (Fig. 3), therefore the signal processing is shifted to a less noisy frequency band of the amplifiers. High flipping pulses (1.5 A peak) are used in order to lower the sensor noise [8] while keeping the maximum power dissipation by a low duty-cycle.

Synchronous demodulators with the reference signal of 30 kHz provide reconstruction of the flipped output of the AMR sensors. The 30-kHz demodulation stage is followed by a sampling circuit using a switched integrator, which is inactive in the noisy time intervals, where the sensor output is recovering after a flipping

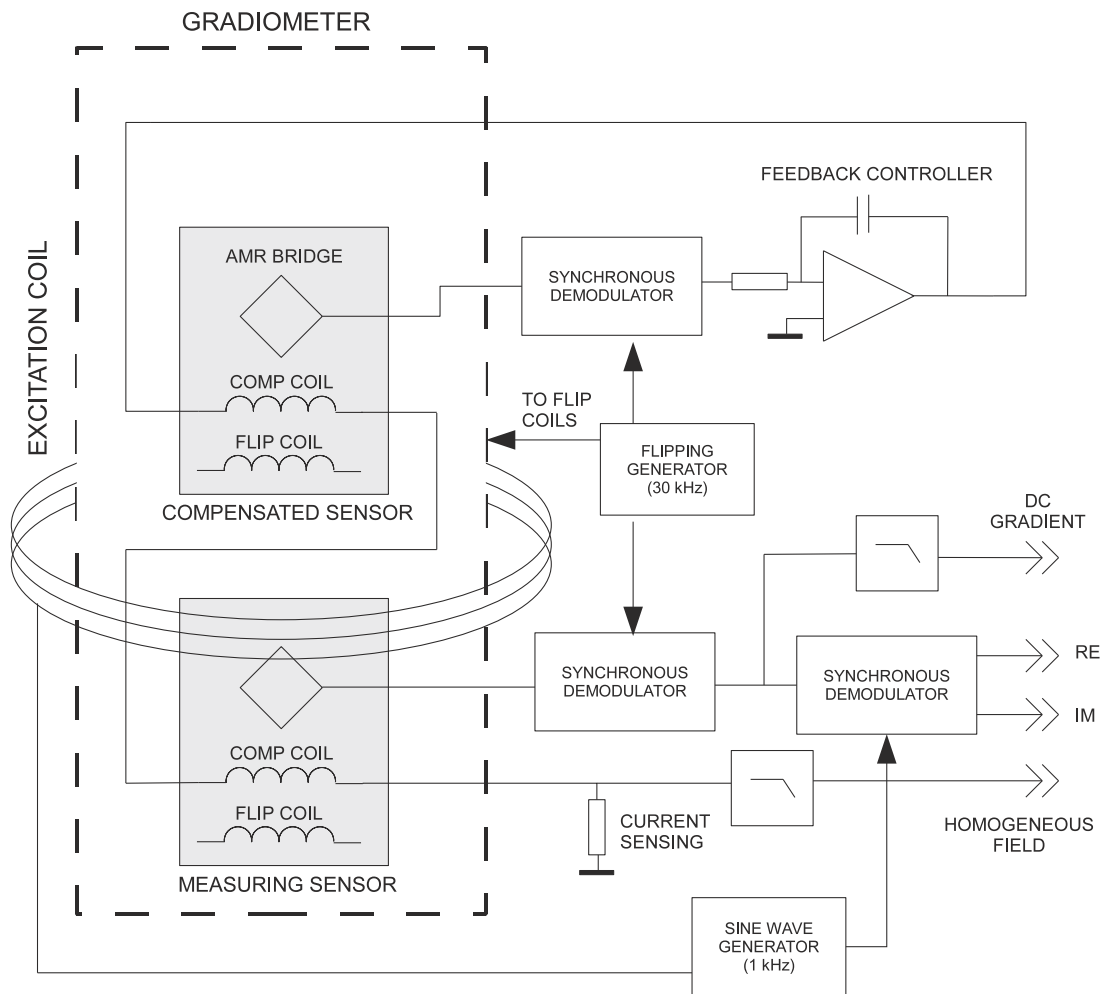


Fig. 2. Functional diagram of the gradiometer operating in the excitation coil. Gradiometric function is obtained by connecting the on-chip compensation coils of the “measuring” and “compensated” sensors in series.

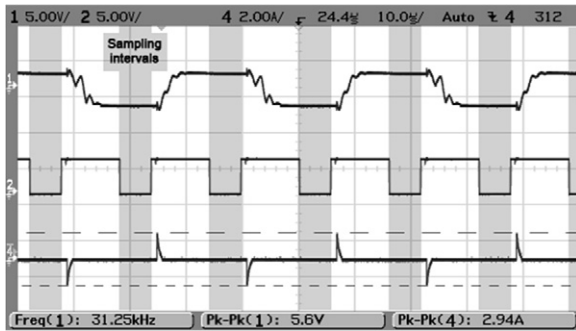


Fig. 3. Sensor output (top trace) and the reference (middle) of the switched integrator suppressing the noisy intervals after flipping pulses (bottom trace).

pulse [9]. The sensor connected to the feedback regulator is maintained in a zero magnetic field by the compensation coil current from DC up to 1 kHz. The compensating current flows through the serially connected compensating coils of both AMR sensors, so the output of the second (measuring) sensor is proportional to the magnetic field gradient. Suppressing the excitation field in addition to the suppression of the Earth's DC field by the compensator allows using higher excitation fields, therefore provides a reserve in DC gradient measurements and possibly an improvement in S/N ratio.

There are four relevant outputs of the gradiometer: the DC field, DC field gradient and the AC field gradient decomposed into the real and imaginary parts. The DC field magnitude (homogeneous part compensating both sensors) is sensed on a shunt resistor in the feedback loop and can be used for correcting for the spurious sensitivity on the Earth's field due to non-orthogonalities of the gradiometer.

4. System noise

The noise of the measuring channel, which consists of a KMZ51 sensor, an AD621 preamplifier and a 30 kHz demodulator, is shown in Fig. 4 – it was determined as 3.1 nT/ $\sqrt{\text{Hz}}$ @ 1 Hz and 268 pT/ $\sqrt{\text{Hz}}$ @ 1 kHz, respectively. When the feedback compensation is switched on (as in the normal operation), the noise increases by 19% @ 1 Hz and 38% @ 1 kHz. This roughly corresponds to a noise increase due to adding an uncorrelated noise signal with the same standard deviation, which comes from the second (compensation) AMR sensor in our case. We could confirm the lack of correlation by the coherence measurement – the compensating current did not show any

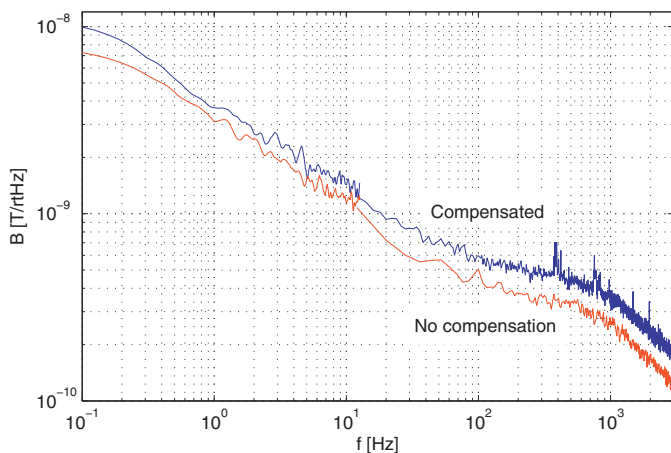


Fig. 4. Noise of the AMR sensor KMZ51 after the first demodulation (bottom trace), the influence of the feedback compensation (top trace). Noise level decrease above 1 kHz is caused by the low pass filter of the demodulator.

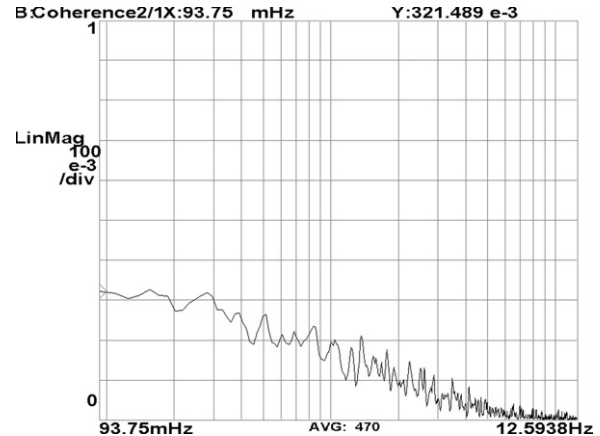


Fig. 5. Coherence of the compensating current and the measuring sensor output, the region of the near zero coherence continues up to 1 kHz.

significant coherence with the signal from the measuring sensor (Fig. 5).

The $1/f$ noise of the sensor dominates in DC field measurements and decreases with the frequency. At higher frequencies, the system noise can be already limited by the instrumentation amplifier noise and resistive thermal noise of the bridge elements:

$$B_N = \frac{1}{S} \sqrt{4kTR + V_{ni}^2 + (V_{no}/G)^2 + (I_{ni}R)^2/2} \quad (1)$$

The noise spectral density thus decreases with the lower resistance of the AMR bridge (R) and higher sensitivity (S), which can be augmented by a higher bridge bias voltage. The most critical parameters of the instrumentation amplifier are the input voltage noise (V_{ni}), output voltage noise (V_{no}), current noise (I_{ni}) and the gain (G). For the KMZ51 and AD621 instrumentation amplifier, this would yield 137 pT/ $\sqrt{\text{Hz}}$ noise spectral density which corresponds to the measured electronics noise – the 1-kHz electronic noise was 141 pT/ $\sqrt{\text{Hz}}$ in this case, and was mainly limited by the 10 nV noise of the instrumentation amplifier. As we did not notice any further improvement in the noise level of the KMZ51 when increasing its gain by a higher bridge supply voltage, we can conclude that even at 1 kHz we were measuring the intrinsic magnetic noise of the sensor [10].

Further improvement in the noise performance is possible by using another type of AMR sensor [11]. With the AMR sensor HMC1001 and the low-noise instrumentation amplifier INA103 we were able to achieve 33 pT/ $\sqrt{\text{Hz}}$ @ 1 kHz, however the power consumption disqualifies these components from the application in an advanced handheld metal detector using multiple of these gradiometers in an array.

5. Detection performance

The gradiometer output was tested on aluminum and ferrous objects in different distances. The best approximation curve for both AC and DC gradient responses resulted in x^{-3} . Compared to conventional metal detectors with an induction coil (e.g. Schiebel ATMID), the AMR gradiometer with KMZ51 sensors has still about a half of the detection depth. An aluminum object of 5×5 cm could be recognized from the noise level at the gradiometer AC output up to the distance of 20 cm. A ferrous nail 3 cm long and 3 mm thick could be recognized in the DC gradient signal up to the 10 cm distance.

Graphs of the spatial resolution (Fig. 6), measured with the 27-cm-diameter excitation coil, confirm that the gradiometer responds to the local magnetic field disturbance, rather than the possible changes of the excitation field caused by the changing inductance of the coil. Therefore it is possible to use an array of

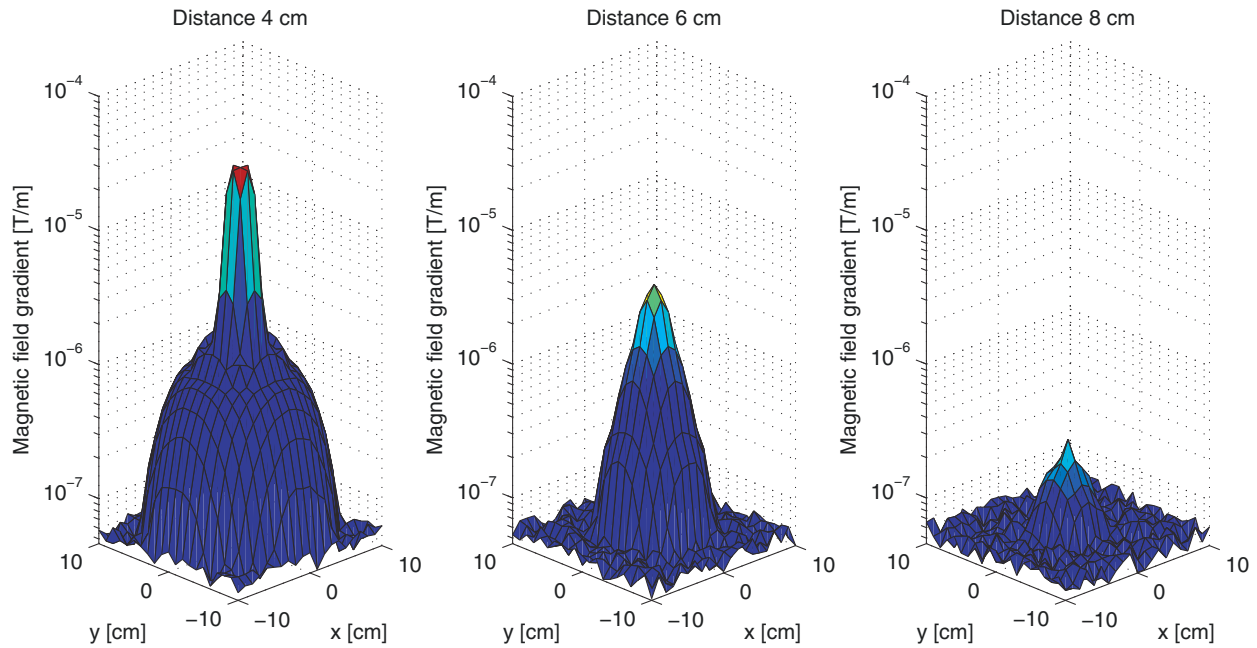


Fig. 6. Single gradiometer scans showing the spatial resolution – a 10 mm diameter stainless steel sphere at distances of 4 cm, 6 cm and 8 cm (AC gradiometer response).

gradiometers inside a single large coil (Fig. 7) – we built a prototype of such a metal detector which is a subject of further investigations [12].

However, as the AMR sensors in the gradiometer have their sensitive axes not perfectly coaxial, the gradiometer is still sensitive to homogeneous fields. Due to limited soldering accuracy and with no factory specifications of the sensitive axis deviation to the package frame of the sensor, the parasitic sensitivity will also differ for each gradiometer. For one gradiometer it was determined by calibrations to be 150 nT/50 μ T (output change caused by rotation in the Earth's field). The mine detector will be operated by sweeping in the horizontal plane; therefore at higher latitudes (e.g. the most of Europe) the main part of the Earth's field is vertical to the detector head: this linear dependence can be then used for correcting of the DC response using the homogeneous field magnitude (one of the four gradiometer outputs). The AC output of the gradiometer was

found not to be affected by homogeneous fields, as the excitation field direction is stable.

6. Conclusion

The presented gradiometric mine detector uses AMR sensors of KMZ51 type for metal detection together with 1-kHz continuous-wave excitation. As the gradient response of ferromagnetic and diamagnetic objects falls with distance approximately with a $1/r^3$ rule, the most limiting factor of the maximum detection depth is the sensor noise – in our case we can detect a 50 \times 50 mm aluminum plate up to 20 cm depth only being limited by the 268 pT/ $\sqrt{\text{Hz}}$ sensor and electronics noise at 1 kHz, which translates to 6.7 (nT/m)/ $\sqrt{\text{Hz}}$ gradient noise. Further improvement of the detection depth is possible when using AMR sensors with a lower noise at the cost of increased current consumption. Prospectively, the high spatial resolution of AMR sensors should allow to recognize objects by using signals from a sensor array.

Acknowledgement

This research was supported by the internal grant of the Czech Technical University in Prague, SGS10/205/OHK3/2T/13 “Compact sensors of magnetic field gradient – development and application”.

References

- [1] D. Guelle, A. Smith, A. Lewis, T. Bloodworth, *Metal Detector Handbook for Humanitarian Demining*, European Communities, 2003.
- [2] D.S. Benitez, S. Quek, P. Gaydecki, V. Torres, A 1-D solid-state-sensor-based array system for magnetic field imaging of steel reinforcing bars embedded within reinforced concrete, *IEEE Transactions on Instrumentation and Measurement* 58 (2009) 3335–3340.
- [3] S. Tumanski, A. Liszka, The methods and devices for scanning of magnetic fields, *Journal of Magnetism and Magnetic Materials* 242 (2002) 1253–1256.
- [4] R.J. Wold, C.A. Nordman, E.M. Lavelly, M. Tondra, E. Lange, M. Prouty, Development of a handheld mine detection system using a magnetoresistive sensor array, *Proceedings of SPIE* 3710 (1) (1999) 113–123.
- [5] D.F. He, M. Tachiki, H. Itozaki, Highly sensitive anisotropic magnetoresistance magnetometer for Eddy-current nondestructive evaluation, *Review of Scientific Instruments* 80 (2009), 036102-1–036102-2.

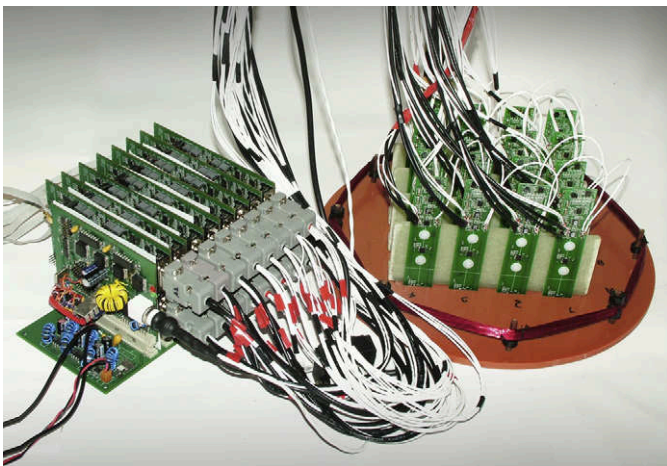


Fig. 7. The array of gradiometers with AMR sensors KMZ51 in a prototype mine detector.

- [6] T. Dogaru, S.T. Smith, Giant magnetoresistance-based eddy-current sensor, *IEEE Transaction on Magnetism* 37 (2001) 3831–3838.
- [7] R. Sikora, T. Chady, S. Gratkowski, M. Komorowski, K. Stawicki, Eddy current testing of thick aluminum plates with hidden cracks, *Review of Progress in Quantitative Nondestructive Evaluation* 20 (2003) 427–434.
- [8] H. Hauser, P.L. Fulmek, P. Haumer, M. Vopalensky, P. Ripka, Flipping field and stability in anisotropic magnetoresistive sensors, *Sensors and Actuators* 106 (2003) 121–125.
- [9] P. Ripka, M. Vopalensky, A. Platil, M. Doscher, K.M.H. Lenssen, H. Hauser, AMR magnetometer, *Journal of Magnetism and Magnetic Materials* 254–255 (2003) 639–641.
- [10] N. Stutzke, S.E. Russek, D.P. Pappas, M. Tondra, Low-frequency noise measurements on commercial magnetoresistive sensors, *Journal of Applied Physics* 97 (2005), 10Q107-1–10Q107-3.
- [11] E. Zimmermann, A. Verweerd, W. Glaas, A. Tillmann, A. Kemna, An AMR sensor-based measurement system for magneto-electrical resistivity tomography, *IEEE Sensors Journal* 5 (2) (2005) 233–241.
- [12] M. Janosek, J. Vyhnanek, P. Ripka, CW metal detector based on AMR Sensor Array, *IEEE Sensors 2011 – Proceedings*, pp. 1515–1517.

Biographies

Jan Vyhnanek was born in Prague in 1987. Received the engineering degree from the Faculty of Electrical Engineering, Czech Technical University in Prague in 2011, currently a student of PhD at the Dept. of Measurement. His main fields of interest are magnetic sensors and their applications in detection of metal objects.

Michal Janosek, born in Varnsdorf in 1980, graduated from the Faculty of Electrical Engineering, CTU in Prague in 2007 at the Dept. of Measurement. He is working as a junior researcher and PhD candidate at the same department. His main research activity is the application of magnetic sensors in gradiometers and further development in PCB fluxgate sensors.

Pavel Ripka was born in Prague in 1959. He received an Engineering degree in 1984, a CSc (PhD equivalent) in 1989, Associate Prof. in 1996 and finally Prof. in 2002. He was elected the dean of the Faculty of Electrical Engineering, CTU in Prague in 2011. He continues to work at the Department of Measurement as a Professor, lecturing in Measurements, Engineering Magnetism and Sensors. His main research interests are magnetic measurements and magnetic sensors, especially fluxgate. He is a co-author of 4 books and >200 scientific papers.

3.2.2 CW Metal Detector Based on AMR Sensor Array

This work is an application of the AMR gradiometer with KMZ51 (presented in the previous paper in chapter 3.2.1) for a metal detector with multiple sensors. The goal was to create a hand-held detector which provides more information about the detected object than an induction coil does, for the purposes of object recognition. The advantage of the multiple-sensor detector is the ability to present to the user the precise location and also the shape of the object and indicate presence of multiple objects.

These features could enable object recognition and discrimination in the application of mine detection. Although the standard metal detector technology with an induction coil is able to roughly recognize objects based on the material properties and signal profile, this is not useful for mine detectors which are therefore constructed to produce alarm on any metal object. For this reason demining is a slow process and provides opportunity for improvement.

The AMR metal detector consists of 16 gradiometers arranged in a 4 x 4 array which is mounted inside an excitation coil. The coil is producing a 1 kHz field with 150 μ T amplitude. The detector measures simultaneously DC gradient additionally to AC response of metal objects, which is another advantage over the induction coil detectors. Digitized signals are delivered to a PC and displayed in four graphs for DC field, DC gradient and real and imaginary components of the 1-kHz excitation field. The detector exhibited good ability to precisely locate even multiple objects. However due to the fact, that AMR sensors are more noisy than a detector with an induction coil, the detection depth was reduced 2 to 3 times compared to a conventional mine detector.

CW Metal Detector Based on AMR Sensor Array

M. Janosek, J. Vyhnanek and P. Ripka

Dept. of Measurement, Faculty of Electrical Engineering
Czech Technical University in Prague
PRAHA 6, Czech Republic
Email: janosem@fel.cvut.cz

Abstract— We developed an eddy-current metal detectors with Anisotropic Magneto-resistors (AMR's) arranged in a 4x4 array. The magnetoresistive sensors in a gradiometric configuration are sensing the vertical component of the magnetic field – either originating from magnetized ferromagnetic bodies or induced by 1-kHz, alternating continuous-wave excitation. The AMR's are arranged so that the homogeneous Earth's field and the large excitation field can be suppressed. The mine-detector was constructed as a standard portable device. The presented results show that the performance is limited by the noise of the selected magnetoresistive sensor. If the size of the sensor array was increased, the system could form an advanced mine-detector for quick, large-scale demining purposes.

I. INTRODUCTION

Modern metal detectors should not be only very sensitive, but also very selective and be able to compensate the influence of soils containing ferromagnetic particles as well as electrically conducting medium when working in wetlands and shallow waters. A pick-up coil is practically the only sensor used to detect field variations caused by eddy currents in a conducting object. It would be very desirable to replace it by a smaller sensor, which would give better spatial resolution and allow arranging of the sensors in scanning arrays for speeding up the detection process [1].

Magnetoresistive sensors are the favorite for this purpose as they became readily available and low-cost. A fluxgate sensor might be used too [2], but the excellent noise performance of a fluxgate is traded off for its complexity, cost and size.

The main advantage of an AMR is its small size, which allows to achieve much higher spatial resolution compared to the traditional pick-up coil. When compared to other magnetoresistive sensors (GMR, SDT), AMRs have an advantage of low DC magnetic noise. Drawbacks of AMRs compared to the pick-up coils are however numerous: increased power consumption, $1/f$ noise, non-linearity, perming, and necessity of periodical flipping.

In [3], authors described an advanced, eddy-current handheld mine-detection system with SDT sensors using pulsed excitation. The device was quite complex, however we are not aware of any real-world performance data. As the low

frequency noise of the SDT sensors is too high, it did not allow for including the DC magnetic response.

II. DESCRIPTION OF THE METAL DETECTOR

Our metal detector is based on an array of 16 AMR gradiometers, arranged in a 4x4 matrix, sharing a common continuous-wave excitation coil. The metal detector is able to sense the AC response to the excitation field and the DC magnetic field, decomposed in 4 components. All of them are available at one moment: Re and Im component of the AC response, DC field gradient and DC homogeneous field (mainly for calibration and verification purposes).

The electronics of the mine-detector is built on a modular base with 19 blocks – the flipping generator, CW amplifier, 8 two-channel signal-processing blocks and finally the data-transfer module (Fig. 1). On the search-head, the 16 gradiometers with KMZ51 sensors in 4-cm distance are arranged in a 4x4 matrix. The size of the search head is approx 35 cm in diameter (Fig. 2A), the coil generates a 1-kHz AC field of 150 μ T amplitude.

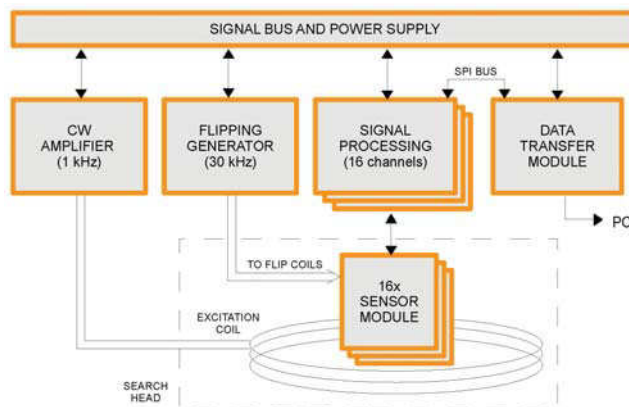


Figure 1. Building blocks of the mine-detector

For a reliable operation the sensors should be periodically flipped, otherwise the stable monodomain state could be corrupted by field or temperature shocks and performance of the sensor would deteriorate. The flipping frequency (30 kHz)

was relatively high to avoid overlap with signals resulting from the main excitation field of 1 kHz.

Every signal-processing channel consists of the respective synchronous detectors (30 kHz, 1 kHz Re and Im), a PI feedback regulator, amplifiers and filters. Each 2 channels share a 24-bit delta-sigma AD converter ADS1278 (Fig. 2B) with 96 samples/second, giving 48 Hz alias-free bandwidth. The Earth's field and most of the 1 kHz excitation field are compensated using the internal feedback coils of the KMZ51 by the negative feedback-loop with the "distant" sensor as reference. The detailed principle of each gradiometer was described by the authors in [4].

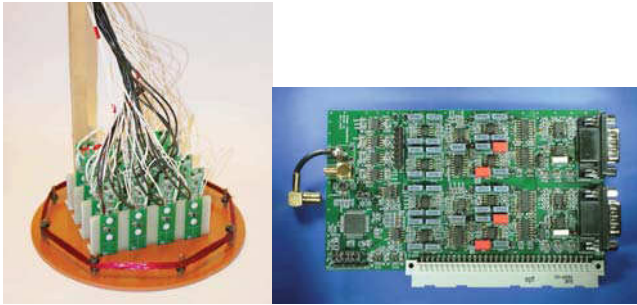


Figure 2. A – the sensor head with 4x4 matrix, B – electronic with 2 channels. The upper sensor is the "distant", the lower "close" sensor is hidden in the search-head frame to be as close as possible to scanned object

The data from all 16 channels (64 values) are simultaneously transmitted using daisy-chaining via USB to the host computer for postprocessing in LabView environment.

III. LABORATORY RESULTS

A. Noise performance

Noise performance was tested with one of the gradiometers. After increasing the flipping pulses to 2.9A peak-peak [6, 7], we obtained 1-kHz noise of 200 pT/ $\sqrt{\text{Hz}}$ (limits detection of diamagnetic objects) and 2 nT/ $\sqrt{\text{Hz}}$ at 1 Hz (DC field response of ferromagnetic objects). The noise figures are shown in detail in [4] and correlate with those published in [8] – as we did not find any significant coherence between the two AMR sensors noise, the influence of the common current-source was negligible. For the perspective use of an AMR with lower noise (HMC1001 was shown to have 15 pT/ $\sqrt{\text{Hz}}$ @ 1 kHz [9]), we face two problems:

- the noise of the electronics is 150 pT/ $\sqrt{\text{Hz}}$ at 1 kHz, and is mainly limited by the noise of the instrumentation amplifier sensing the bridge output.
- the internal feedback-coil constant of HMC1001 is low, excessive current would be needed for each channel to compensate Earth's field

The solution of the electronic noise is only by increasing the AMR gain (by applying larger supply voltage – up to 8V for KMZ51, up to 10V for HMC1001) or by selecting a better instrumentation amplifier.

As the compensating current of the HMC1001 is tens of mA's for the Earth's field, the power consumption of the device would significantly increase (the feedback coil constant of KMZ51 is 10x larger), causing further problems in power consumption of a portable instrument

Further reduction of the noise is possible by averaging: for 1 second, we should be able to lower the noise 10x as we are sampling at 100 samples/s. It was however not used as we required dynamic performance of the detector.

B. Response to test object

Figures 4 and 5 show the response in 3, 6 and 9-cm depth to an empty Kalashnikov shell, which was moved in a 5-cm grid below the sensing head (Fig. 3). It can be seen that for the steel shell, the DC response is 3-orders of magnitude larger; however both the DC response and Im part of the AC response are similar, allowing to identify the position of the shell with a single scan (Fig. 6).

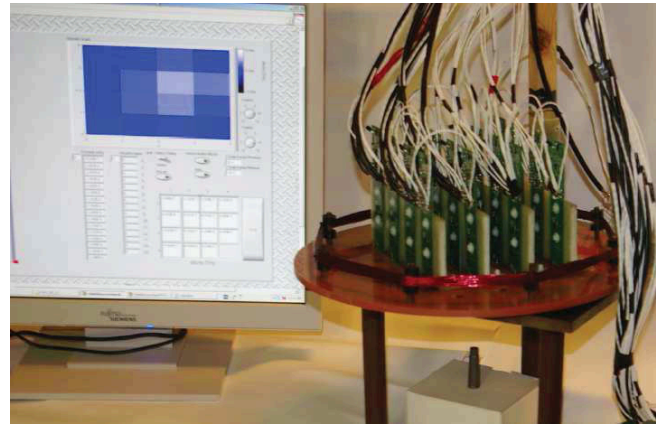


Figure 3. Measuring the response to the test object

During tests, it turned out that even for measuring field "gradient", the response of distant objects is $1/r^3$ and not $1/r^4$: in most cases the response falls quickly enough so that the "distant" sensor measures only Earth's field or the excitation field, and does not see the object's response measured with the "close" sensor (Fig. 2A).

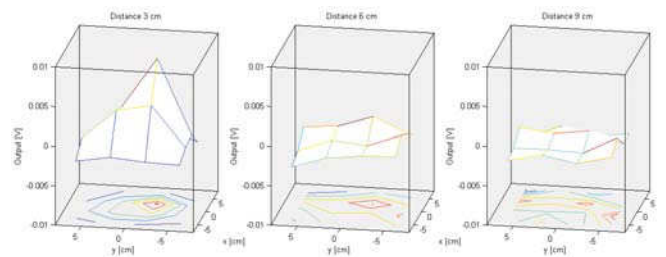


Figure 4. IM part of the AC response –Kalashnikov shell in 3, 6 and 9-cm depth

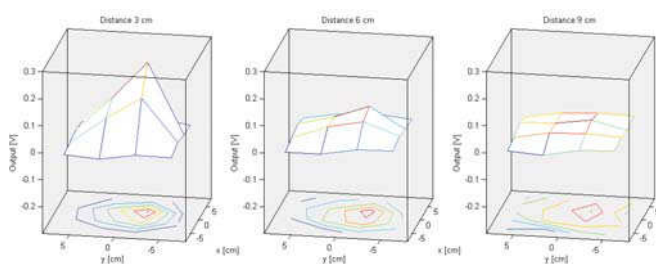


Figure 5. DC response – Kalashnikov shell in 3, 6 and 9-cm depth

The maximum detection depth of the steel shell was 13 cm and of an 5x5cm aluminum plate it turned out to be 20-cm. In both cases, the sensor noise was the limiting factor.

IV. FIELD TEST

To exclude the laboratory noise, the mine-detector was rearranged to a portable, battery-powered device. However due to large power consumption (~20W) and moderate weight (5kg), the portability was somehow affected (Fig. 6A). For a real-world application, it turned out that an average of all 16-sensors was helpful to create a thresholded alarm, and that the position of the sensing head should be determined in some means [10] to incorporate averaging during multiple sweeps. Fig. 6B shows the response to sweeping over Khalasnikov shell with decreasing distance from 20 cm down to 1cm.

V. CONCLUSION

The presented mine-detector shows that it is possible to build a CW-metal detector with AMR sensors – the main problem of compensating the excessive excitation field amplitude was solved. The 4x4 array of gradiometers proved usable for small, shallow objects, for more distant targets an average from all 16 sensors was helpful. As the mine-detectors is able to produce 4 physically meaningful outputs from each channel, the system is overdetermined and it should be possible to improve the detection performance by mathematical postprocessing, which is out of scope of this paper.

The detection depth is mediocre, a noise reduction of at least one magnitude is needed. This is possible with another type of AMR sensor, however the power consumption would then disqualify this type of mine-detector from being portable. In this case re-arranging the sensing head to a larger array, or a single-line scanner, would allow to create a highly efficient, large-scale detection system, which could be towed or moved by other means.

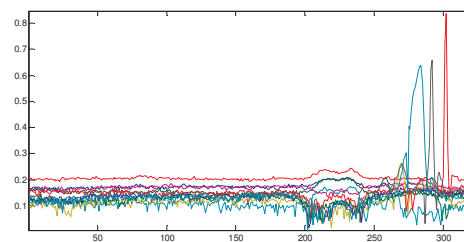


Figure 6. A – the portable version of mine-detector during field tests, B – 16-ch response to sweeps 20 to 1 cm above a steel shell (highlighted with $\sqrt[3]{|y|}$)

REFERENCES

- [1] H. H. Nelson and J. R. McDonald, "Multisensor towed array detection system for UXO detection", *IEEE Transactions on Geoscience and Remote Sensing*, Vol. 39, No. 6, pp. 1139-1149, 2009
- [2] Y. Zhang, M. Steiger, A. D. Hibbs, R. E. Grimm and T. A. Sprott, "Dual-mode, Fluxgate-Induction Sensor for UXO Detection and Discrimination", *Journal of Environmental & Engineering Geophysics*, Vol. 15, p. 51-64, June 2010.
- [3] R. Wold, C.A. Nordnlan, E.M. Lavelly, M. Tondra, E. Lange and M. Prouty, "Development of a handheld mine detection system using a magnetoresistive sensor array", *Proc. SPIE*, vol. 3710 (1), pp. 113-123, 1999.
- [4] J. Vyhnanek, M. Janosek and P. Ripka, "AMR gradiometer for mine detection and sensing", *Proceedings of Eurosensors XXV*, September 2011, accepted.
- [5] N. A. Stutzke, S.E. Russek, D. P. Pappas, M. Tondra, "Low-frequency noise measurements on commercial magnetoresistive magnetic field sensors", *Journal of Applied Physics*, Volume 97, Issue 10, pp. 10Q107-10Q107-3, 2005.
- [6] P. Ripka, M. Vopalensky, A. Platil, M. Döscher, K. -M. H. Lenssen and H. Hauser, "AMR magnetometer". *Journal of Magnetism and Magnetic Materials* 254-255, pp.639-641, 2003
- [7] H. Hauser, P.L. Fulmek, P. Haumer, M. Vopalensky and P. Ripka, "Flipping field and stability in anisotropic magnetoresistive sensors", *Sensors and Actuators A*, Vol. 106, pp. 121-125, 2003
- [8] E. Zimmermann, A. Verweerd, W. Glaas, A. Tillmann and A. Kemna, "An AMR sensor-based measurement system for magneto-electrical resistivity tomography", *IEEE Sensors Journal*, Vol. 5, no. 2, pp. 233-241, April 2005
- [9] D. F. He, M. Tachiki, and H. Itozaki, "Highly sensitive anisotropic magnetoresistance magnetometer for Eddy-current nondestructive evaluation", *Review of Scientific Instruments*, Vol 80, pp. 036102, 2009
- [10] H. Krüger and H. Ewald, Handheld metal detector with online visualisation and classification for the humanitarian mine clearance, *IEEE Sensors*, 2008 Proceedings, pp.415-418, Oct. 2008

3.2.3 Linear scanner with magnetic field mapping

This work deals with modifications to the above-mentioned metal detector to create a linear array scanner. First experiments of visualization of metallic construction structures are presented.

Based on the experience with low sensitivity to small metal components contained in minimum-metal mines, further efforts were focused on a different application and the detector was redesigned accordingly. The studied application was visualization of concealed metal construction structures, which are usually made of massive metal parts and provide enough response of the AMR gradiometers up to the distance of 10 cm in AC mode.

Due to the same orientation of the axes of the gradiometers and the excitation coil, the AC mode provides images even of complex structures, like a reinforcing mesh, directly without further processing. For example a competitive magnetic-method based device Ferrosan (Hilti, 2006) requires merging of two perpendicular scans due to perpendicularly oriented axes of its excitation coil and gradiometers.

Apart from the apparent application of avoiding drilling through a pipe or hitting a reinforcing bar, there is a requirement of the building industry to inspect thickness of a covering layer of concrete above reinforcing steel. If the concrete layer is too thin, the steel is prone to corrosion and consequently the corrosion products react with concrete and damage it. For depth estimation, devices based on magnetic method are superior to competitive radar technology, because the speed of electromagnetic wave in concrete is variable and greatly influenced by humidity of the concrete. The same holds true for verifying the diameter of steel bars. But unlike radar technology, magnetic methods cannot detect non-metallic structures, so neither method is universal.

Great attention was devoted to the excitation coil design. The resulting coil design is a compromise between homogeneity of the inner area 1) in the direction of the sensor array and 2) in the perpendicular direction. Narrow rectangular coil demonstrated good homogeneity along the long side, i.e. in the direction of the sensor array, whereas in the direction of the short side the field changes rapidly with position. This is a concern of mechanical stability of a holder of the coil and gradiometers. Length of the short side also determines, whether the excitation field is strong, but of short range, which is more suitable for smaller objects, or if it is weaker and of longer range. A coil with a size of 80 cm x 10 cm has been chosen.

In the prototype several possible improvements were identified which are to be addressed in the subsequent design. First, the mechanical construction of the detector has to be rigid, because even subtle deformations of the coil result in a change in the output signal, so does any change in orientation of gradiometers to the coil. Next, for a stand-alone instrument an embedded computer is to be added which will present measured data in real-time using a position sensor with optical encoder.

Linear scanner with magnetic field mapping

Jan Vyhnanek¹, Jakub Král²

¹ UCEEB CTU, Nam. Sitna 3105, 272 01 Kladno 2, Czech Republic

² Dept. of Measurement, Czech Technical University, Technicka 2, 166 27 Praha, Czech Republic

jan.vyhnanek@uceeb.cz, kraljaku@fel.cvut.cz

Abstract. Presented device is a detector of metallic and ferromagnetic objects with the ability to create images of magnetic fields. The detection head utilizes an array of 16 gradiometers composed of anisotropic magnetoresistors (AMRs) which are sensitive to both steady-state (DC) and alternating (AC) magnetic fields. Thus the sensors are sensitive to ferromagnetic objects. With the addition of an external excitation field also non-ferromagnetic metals are detected due to the magnetic response of eddy currents. The array of sensors is arranged in a linear scanner so the scanning speed is good, the scanning area is 0.6 m wide and the resolution in the direction of scanner motion is high. Digitized signals of gradiometers are transferred to a portable computer to create maps of DC and AC magnetic fields which correspond to the shape, depth and material of the detected objects.

Keywords

metal detector, gradiometer, anisotropic magnetoresistor, magnetic field mapping

1. Introduction

Mapping of magnetic fields is useful in applications where information about the shape or precise position of the detected object is required, in addition to the information whether the object is present or not offered by simpler devices. Applications of magnetic mapping can be found e.g. in non-destructive testing (NDT), metal detection and geophysical surveys.

Generally there are two approaches which use magnetic fields for detection, the first is suitable for ferromagnetic objects and detects steady-state (DC) field surrounding the object. The second one, suitable for highly conductive materials like metals, is based on magnetic field response generated in objects by using external alternating (AC) field.

An example of NDT application is Ferroskan produced by Hilti [1] which is designed for mapping of steel reinforcement in concrete blocks used in building industry. The detection head consists of an array of DC magnetic field sensors and a permanent magnet which is used to guide the magnetic flux of rather randomly

magnetized steel bars. Another application using the DC magnetic field is the mapping of areas with unexploded ordnance [2] and geophysical surveys in archeology [3]. A scanner with DC field sensors [4] can be used for imaging of magnetic fields surrounding ferromagnetic components.

Methods based on the AC magnetic field have been used in applications like detection of cracks in metals [5], imaging of magnetic fields of mines [6] or mapping of mine fields [7].

2. Construction of the detector

The detector combines both DC and AC methods by evaluating frequencies in the range of DC and 1 kHz. The DC range is naturally sensitive to ferromagnetic objects, while the AC range detects all conductive materials due to eddy currents induced by an excitation coil.

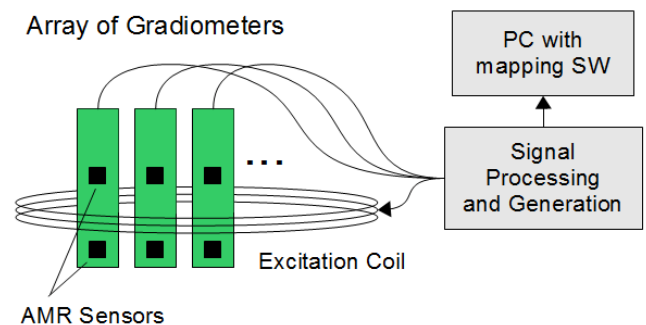


Fig. 1. Detector consists of a linear array of gradiometers and excitation coil. Signals of the array are processed and generated in a block of electronics with an output for PC

The main parts of the detector are described in Fig. 1. An array of anisotropic magnetoresistors (AMRs) is used for magnetic field sensing. The detector operates as a linear scanner which creates images of magnetic fields.

The sensors are used in gradiometric arrangement to compensate the magnetic field of the Earth and the excitation field. The operating principle was described in [8]. The electronics employed in the detector comes from the CW metal detector designed originally for mine detection [9].

2.1 AMR sensors

Each of the 16 gradiometers in the array consists of two anisotropic magnetoresistors (AMRs) KMZ51 type (Philips/NPX). KMZ51 are single axis sensors of magnetic field with a small-dimension SOIC package. The AMRs use so called flipping, which is periodical remagnetization of the internal magnetic layer by strong and narrow magnetic pulses, resulting in modulation of the sensor output. It is used to enhance the temperature coefficient of sensitivity and offset of the sensor and to transfer the signal processing to a less noisy frequency range of the electronics. The drawback of the flipping function lies in the complex circuitry, higher power consumption and reduced frequency range of the measured magnetic fields. However in this application the flipping function is necessary to achieve the good resolution in the measurement of low magnetic fields.

2.2 Gradiometers

The AMR sensors are exposed to the strong magnetic field of the Earth (absolute value of $48 \mu\text{T}$ in the Czech republic) and the excitation coil (about $400 \mu\text{T}$ p-p). The sensors are allowed to be exposed to fields up to $240 \mu\text{T}$, so the sensors are connected as zero-field detectors using an on-chip compensation coil and a current feedback loop.

Another complication presents the high dynamic range of the measurement, where weak fields in the order of nT have to be detected on the strong background field. These strong fields however are roughly homogeneous so gradiometers are used to suppress them in this detector design.

Noise of the sensors also limits the resolution. The measured noise of one gradiometer used in the detector design is $92 \text{ (nT/m)/}\sqrt{\text{Hz}}$ at 1 Hz and $9.3 \text{ (nT/m)/}\sqrt{\text{Hz}}$ at 1 kHz [8]. Temperature drift produces significant error which is for the AMR KMZ51 typically 2 nT/K . Another error source is the spurious sensitivity to homogeneous field of the gradiometer in DC range due to misalignment of sensitive axes of the two AMR sensors – for one gradiometer it is $150 \text{ nT}/50\mu\text{T}$ (change of the output by rotation in the Earth's field). The latter error may be compensated by calibration.

The tempco and misalignment errors are dominant. The measuring frequency bandwidth could be selected quite large with the 45 Hz corner frequency for both AC and DC range which allows for high scanning speed (e.g. 1 m/s when scanning reinforcement mesh).

2.3 Excitation coil design

The excitation field is driven by a rectangular coil; the design is depicted in Fig. 2 and Fig. 3. The winding itself has 50 turns; impedance is 8 ohms and inductance 3.16 mH. The 16 gradiometers are linearly spread along the Y-axis resulting in 0.6 m scanning area.

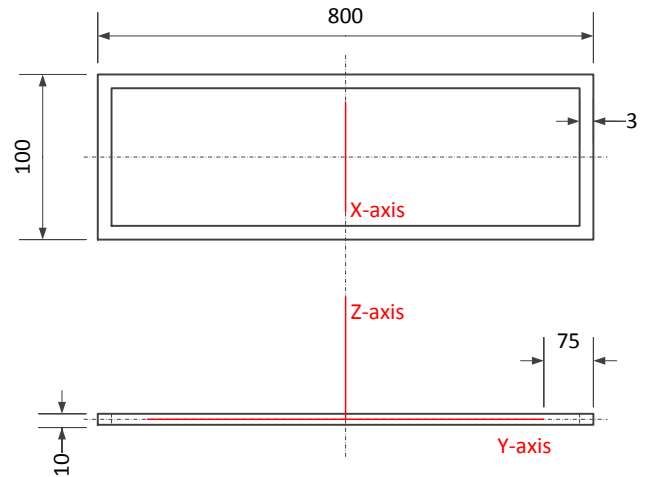


Fig. 2. Design of the excitation coil.

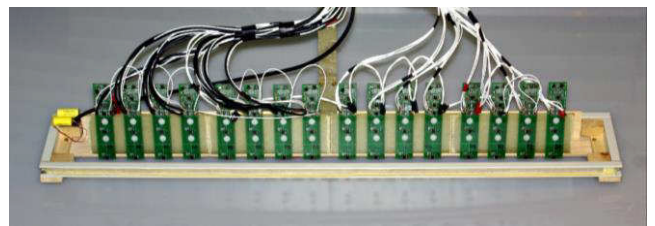


Fig. 3. Actual detection head with the linear array of gradiometers and excitation coil.

A harmonic current of 1A peak-peak and frequency 1 kHz excites the coil from a harmonic generator and generates the magnetic field in the coil vicinity. The coil has been designed and optimized using a FEM modeling software. The main focus of the FEM modeling is to achieve uniform magnetic field distribution inside the coil frame especially on the line where the gradiometers are installed.

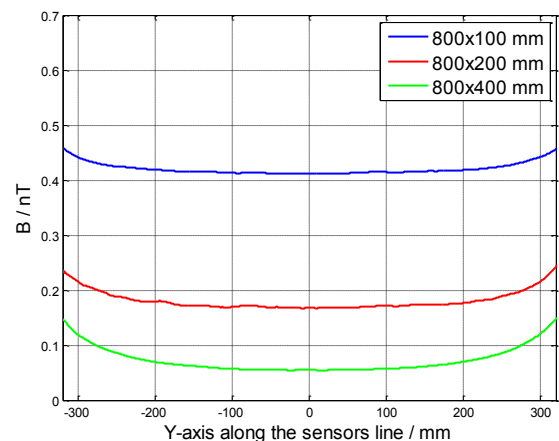


Fig. 4. B-field distribution along the Y-axis of the coil for three size alternatives.

Fig. 4 shows simulated magnetic B-fields along the whole sensor line (Y-axis), with no conductive object in the coil vicinity. Three different X-side lengths of the coil (100, 200, 400 mm) are compared and presented. The narrowest option gives the highest and the most uniform

field in this axis. The curve is relatively flat which means that the scanned field is constant regardless of the sensor position. Fig. 5 presents simulated field changes in the perpendicular direction (X-axis). On the contrary the field variation is highest for the narrowest coil. Each gradiometer contains two sensing elements, one over another that measure vertical field gradient. It is evident that the narrow coil sets the highest demands on the perpendicular position of gradiometers to the X-axis. The uniform influence of the excitation field on each sensor in the array should be ensured.

Taking into account all the aspects that have been investigated the narrowest option (100 mm) is considered to be the most suitable for this application, because the requirements on the position of gradiometers are easily achievable.

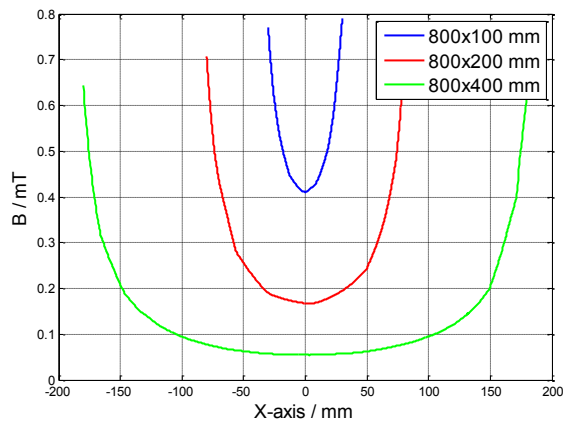


Fig. 5. B-field distribution along the X-axis of the coil for three size alternatives.

3. Measurement trials

Signals collected by the sensors are presented in a graphical Labview based software. Gradients of AC and DC field are indicated in two separate false-colour intensity graphs. As the detection head does not currently incorporate any positioning device like a wheel with an encoder, the measurement is free-running and the intensity graph is updated immediately with newly arrived data. Scans are acquired with a constant scanning speed and the dimension in the scanning direction can be calculated using the indicated time of the scanned samples.

To evaluate detection limits the trial measurements were performed with the stationary detection head so to avoid errors in the DC gradient when moving the detection head. The error is caused by the non-compensated misalignment of the sensors (however it does not affect the AC gradient, see chapter 2.2 Gradiometers). A scanned object is then positioned under the detector by a hand.

Fig. 6 shows the scan of a ferrous screw in the depth of 6 cm under the detection head. The DC gradient shows the typical field of a magnetic dipole, while the AC gradient, originating from induced eddy currents, better

represents the shape of the screw. The overall detection depth is however better for the DC gradient, the magnetic field of the screw could be recognized up to the 10-cm depth.

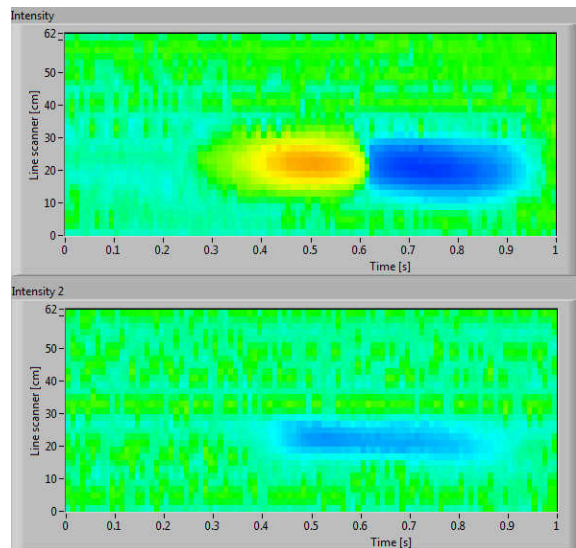


Fig. 6. DC gradient (upper) and AC gradient (lower) scan of a ferrous screw 1 cm x 10 cm which is 6 cm under the detector. The whole scan took 1 second.

Another tested object was a steel reinforcement mesh in the depth of 6cm (Fig. 7). The DC gradient shows random magnetization of the steel mesh which does not correspond to its shape. AC gradient however provides usable picture showing steel bars in the blue and the holes in the red.

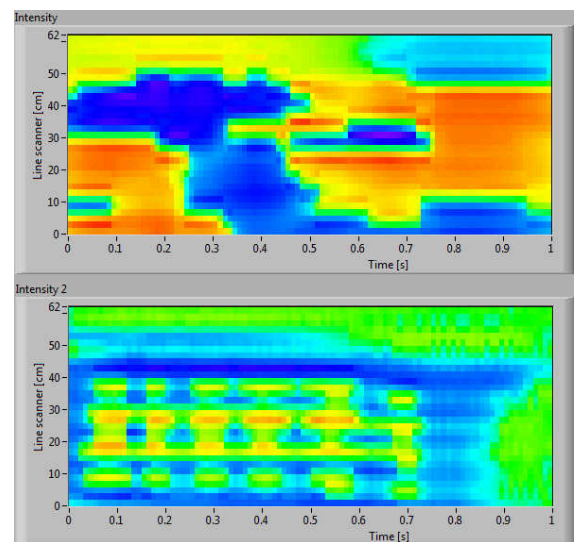


Fig. 7. Scan of a ferrous reinforcement mesh 6 cm under the detector in DC field (upper) and AC field (lower). While the magnetization of the steel is not correlated with the shape of the reinforcement mesh in the DC field, using the AC field the structure is clearly visible.

Non-ferrous metals like copper and aluminum were also tested with the expected zero response in the DC gradient and rather weak response in the AC gradient, plate-like shaped objects were detected in the greatest depths of about 10 cm.

4. Conclusions

The detector benefits from the simultaneous measurement of DC and AC gradient of magnetic fields. This feature allows to simply distinguish between ferromagnetic and non-ferromagnetic metals. The linear array proved to be useful for mapping the magnetic fields with sufficient resolution especially in the direction of scanning so the shape of the object can be estimated. Scans of ferrous objects show better detection depth in the DC gradient, while the image in the AC gradient represents the shape of the object more correctly.

The DC and AC ranges are set for a wide bandwidth of 45 Hz allowing for the high scanning speed up to 1 m/s at the cost of the increased output noise. The noise, temperature coefficient errors and misalignment of sensors in gradiometers limit the detection depth which is not sufficient yet for e.g. diagnostics of steel reinforcement located deeply in concrete. Although the misalignment error may be suppressed by calibrations, further detection depth enhancement could be achieved by replacing the sensors with AMRs of better specifications or fluxgates.

Acknowledgements

This work has been supported by the European Union, OP RDI project No. CZ.1.05/3.1.00/13.0283 – Intelligent Buildings. The work was also supported in part by a Czech Technical University students' grant—Advanced Methods of Signal Processing for Diagnostics SGS12/155/OHK3/2T/13

References

- [1] HILTI Corporation, Ferrosan PS 200 brochure, 2013.
- [2] MUNSCHY, M., BOULANGER, D., ULRICH, P., et al. Magnetic mapping for the detection and characterization of UXO: Use of multi-sensor fluxgate 3-axis magnetometers and methods of interpretation. *Journal of Applied Geophysics*. 2007, p. 168 – 183.
- [3] LINZEN, S., CHWALA, A., SCHULTZE, V., et al. A LTS-SQUID system for archaeological prospection and its practical test in Peru. *IEEE Trans. on Appl. Superconductivity*. 2007, p. 750 – 755.
- [4] TUMANSKI, S., LISZKA, A. The methods and devices for scanning of magnetic fields. *Journal of Magnetism and Magnetic Materials*. 2002, p. 1253 – 1256.
- [5] YASHAN, A., BISLE, W., MEIER, T. Inspection of hidden defects in metal-metal joints of aircraft structures using eddy current technique with GMR sensor array. *Proc. 9th ECNDT*. Berlin, 2006.
- [6] KRUGER, H., EWALD, H. Handheld metal detector with online visualisation and classification for the humanitarian mine clearance. *IEEE Sensors – Proceedings*. Italy, 2008, p. 415 – 418.
- [7] RUSSELL, K.L., DAS Y., MCFEE, J.E., et al. Real-time target detection technique for metal detector arrays: an image processing approach. *Proc. SPIE 3710, Detection and Remediation Technologies for Mines and Minelike Targets*. Orlando, 1999.
- [8] VYHNÁNEK, J., JANOSEK, M., RIPKA, P. AMR gradiometer for mine detection. *Sensors and Actuators*. 2012, p. 100 – 104.

- [9] JANOSEK, M., VYHNÁNEK, J., RIPKA, P. CW metal detector based on AMR Sensor Array. *IEEE Sensors – Proceedings*. 2011, pp. 1515–1517.

About Authors...

Jan VYHNÁNEK was born in Prague in 1987. Received the engineering degree from the Faculty of Electrical Engineering, Czech Technical University in Prague in 2011, currently a student of PhD at the Dept. of Measurement. His main field of interest are magnetic sensors and their applications in detection of metal objects.

Jakub KRÁL was born in Tabor, Czech Republic, in 1983. He received the B.Sc. and M.Sc. degrees from the Faculty of Electrical Engineering, Czech Technical University, Prague, Czech Republic, in 2006 and 2009, respectively, where, since then, he has been pursuing the Ph.D. degree at the Department of Measurement. He is a member of the Laboratory for Diagnostics and Non-Destructive Testing. His current research interests include nondestructive evaluating of material properties using eddy current techniques.

3.2.4 AMR Proximity Sensor With Inherent Demodulation

In this chapter, development and characterization of a low-frequency proximity sensor with an excitation coil and AMR which provides inherent demodulation. Foundations for this sensor principle were already formed in the paper in chapter 3.1.2, where noise performance of several circuits for AMR detectors was studied. Later, during preparation of this paper for publication, it was found out that the principle of inherent demodulation of an AMR sensor was proposed before by Tumanski (2010) to which we added the application for a proximity sensor capable of operating at very low frequencies and even through a conductive shielding.

The sensor consists of an AMR sensor, excitation coil with a square-wave generator and a low-pass filter. The advantage of the sensor is the inherent demodulation feature, which simplifies sensor design, as no other demodulator is necessary. The inherent demodulation occurs when the frequency of the excitation field is the same as the frequency of flipping. Flipping is ensured by supplying short current pulses of several amperes, supplied by switched capacitor, to the flipping coil, which invert magnetization of the AMR and effectively also its output characteristic. Thus the operation is the same as a synchronous demodulator using the excitation frequency as a reference frequency.

The proximity sensor output can be evaluated by comparison with threshold levels for high-permeability and conductive materials. High-permeability materials (ferromagnetic materials, ferrites) increase the amplitude of the excitation field, therefore the output level increases. Conductive materials, due to internally induced eddy currents, decrease the amplitude of the excitation field, therefore the output level decreases. An ambient DC field appears at the output as an AC signal due to the demodulator, which is removed by the low-pass filter.

The sensor was operated at a very low frequency of 100 Hz to enable penetration of the excitation field through a conductive wall (whatever the reason for its presence is). This brings an advantage compared to industry-standard induction sensors which are operated at much higher frequencies. Once the position of the AMR proximity sensor and the conductive shielding is fixed and sensor threshold levels reestablished, metallic object can be detected behind the conductive shielding.

Sensitivity of the sensor to the conductive material can be increased by sampling near the edges of the square-wave excitation field, because eddy currents are most pronounced when the excitation field changes fast. Conversely, sensitivity to high-permeability materials can be increased by sampling at the end of a steady-state interval of the square wave, because this part of the signal is the least influenced by eddy currents from a conductive shielding. These circuits however increase sensor complexity.

A concern in the design with an AMR is the non-linearity of the output in uncompensated mode and the crossfield error. Remanent field of an object in the vicinity of the sensor can shift the operating point of the sensor and create a false detection event. To address this issue, a DC compensation of the proximity signal was created. This however required a synchronous demodulator to extract the DC field component from the sensor output. Bandwidth of the sensor was decreased to filter out the feedback action of the DC field compensation.

However, the sensor in its simplest form without any DC field compensation proved useful for detection of objects with minimum remanent magnetic field and these can be positioned behind a conductive shielding.

AMR Proximity Sensor With Inherent Demodulation

Pavel Ripka, Jan Vyhnanek, Michal Janosek, and Jan Vcelak

Abstract—Our novel position sensor is based on the combination of the eddy-current and permeability effects. The primary field is excited by a coil, but instead of induction coil, the sensing part uses anisotropic magnetoresistor (AMR), which also measures dc magnetic field. As the AMR is being flipped at the excitation frequency, the sensor is self-demodulated and the output is dc. The AMR sensitivity does not depend on frequency; therefore, this sensor can be used at ultralow frequencies, where coils fail as sensors. We show the response of our sensor to ferromagnetic and nonferromagnetic metals and possibilities to distinguish between them. We also show that our sensor can measure position through the conducting sheath.

Index Terms—AMR sensor, magnetoresistor, position sensor.

I. INTRODUCTION

TWO families of proximity detectors and distance sensors are based on magnetic principle:

1. DC magnetic sensors mostly use permanent magnet as a source of the field. The magnet may be attached to the target or the sensor. In the second case the target is ferromagnetic and changes the field shape and its amplitude in the sensor location.
2. Eddy-current proximity detectors and distance sensors are most often based on the change of the quality factor of the coil caused by eddy currents in the target from conducting material [1], [2]. These sensors are often referred as Inductive Sensors.

Our sensor belongs primarily to the second group, but it is also able to measure DC response. The difference is that the source of the DC field is a coil instead of permanent magnet.

A. Inductive Sensors

Inductive sensors usually work in the frequency range of 1 kHz to 100 kHz. New trends of these sensors are

Manuscript received March 17, 2014; revised May 6, 2014; accepted May 9, 2014. Date of publication May 19, 2014; date of current version July 22, 2014. This work was supported in part by the European Union, through the OP RDI Project under Grant CZ.1.05/2.1.00/03.0091—University Centre for Energy Efficient Buildings, Czech Technical University, Prague, Czech Republic, and in part by the Grant Agency of the Czech Republic under Grant P102/12/2177. This is an expanded paper from the IEEE SENSORS 2013 Conference. The associate editor coordinating the review of this paper and approving it for publication was Dr. Kailash Thakur.

P. Ripka and J. Vyhnanek are with the Centre of Energy Efficient Buildings, Faculty of Electrical Engineering, Czech Technical University, Prague 166 27, Czech Republic (e-mail: ripka@fel.cvut.cz; vyhnajan@fel.cvut.cz).

M. Janosek is with the Faculty of Electrical Engineering, Czech Technical University, Prague 166 27, Czech Republic (e-mail: janosem@fel.cvut.cz).

J. Vcelak is with the Centre of Energy Efficient Buildings, Czech Technical University, Prague 166 27, Czech Republic (e-mail: vcelakj1@fel.cvut.cz).

Color versions of one or more of the figures in this paper are available online at <http://ieeexplore.ieee.org>.

Digital Object Identifier 10.1109/JSEN.2014.2325406

described in [3]. These sensors have been also miniaturized by using printed coils [4] or CMOS technology [5]. At high frequencies the penetration depth is very small and the sensor is also strongly influenced by parasitic capacitances. At low frequencies the sensitivity of such sensor is small, which is a consequence of the induction law: the induced voltage is proportional to frequency. However, for some applications it is desirable to use very low working frequency. At low frequency and low permeability the penetration depth is high and the sensor can be used to measure a position of ferromagnetic target through a conducting sheath. The requirement is that the sheath has low permeability – if it is from ferrous material, its permeability can be lowered by DC saturation.

B. AMR Position Sensor

Our novel solution separates the transmission coil from the magnetic field sensor, which is in our case Anisotropic magnetoresistor (AMR) with a frequency response starting from DC [6]. AMR sensors are based on a thin film Permalloy strip, which forms a single domain. The external magnetic field rotates the permanent magnetization of the domain and causes a change of its electrical conductivity. Large external field can cause that the single-domain state is damaged, which results in hysteresis and drop of sensitivity. The cure is called flipping: short periodical pulses of magnetic field which remagnetize the sensor core and restore its single-domain state. If the flipping pulses are bipolar, the sensor output also periodically reverts its polarity, i.e. it is modulated by the flipping frequency. Flipping brings also other advantages:

1. suppression of the sensor offset;
2. suppression of the crossfield effect [7];
3. doubling the sensitivity.

Anisotropic magnetoresistors were already used in eddy-current NDT with high spatial resolution [8]. Compared to induction coil, AMR sensors have smaller size and their response is to some limit frequency independent. Therefore AMR sensors can be used at much lower frequencies than induction coils, which have sensitivity proportional to frequency. Fig. 1 shows the conventional system using AMR: f_{flip} is typically 1 Hz to 1 kHz, the AMR output is AC at $f_{exc} \pm f_{flip}$ frequency. Synchronous demodulator at its output is controlled by f_{flip} and the dominant signal at its output is at f_{exc} .

C. Self-Demodulation

Our new concept of self-demodulated sensor is shown in Fig. 2. The excitation field is a squarewave of the same

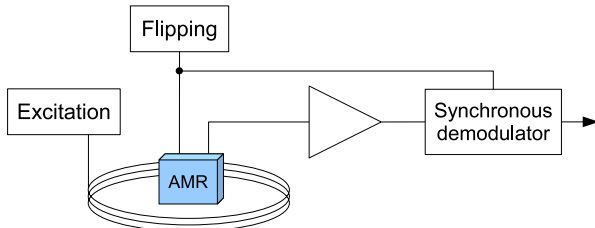


Fig. 1. Flipped AMR with external demodulator. The sensor output is AC at f_{exc} .

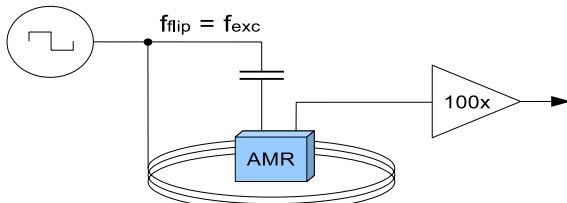


Fig. 2. AMR with inherent demodulation. The primary sensor output is DC.

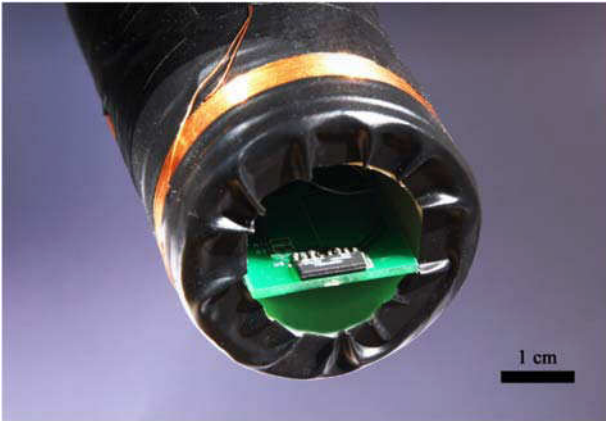


Fig. 3. Experimental proximity sensor with the AMR inside the excitation coil.

frequency as the flipping pulses, so that the sensor output is at DC (and also at $2f_{exc}$).

The possibility to use flipping for signal demodulation was predicted by Tumanski [9], but to our knowledge we were the first who experimentally proved this concept and used it for sensing. The output signal is DC voltage without any external demodulator. We can use the same sensor to separately measure DC magnetic response and eddy-current response.

Our method has three advantages over DC magnetic position sensors:

1. it does not require any permanent magnet,
2. it suppresses the influence of the external DC magnetic fields and magnetic remanence of iron parts, and
3. it works also for non-magnetic conducting targets.

The only limitation is the measuring range of the AMR sensor as the DC magnetic field results in the AC output signal. However, using an appropriate processing and feedback compensation the DC magnetic field can be suppressed. By this sensor we can separately measure DC magnetic response and eddy-current response in order to compensate for the target temperature-dependent permeability.

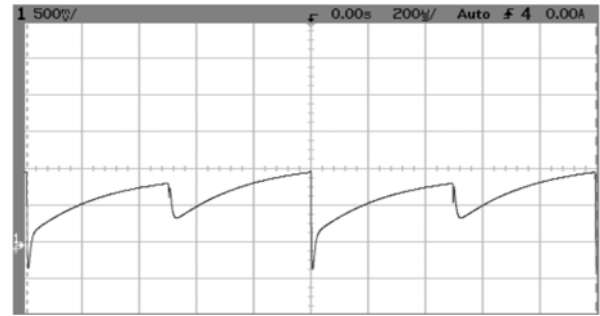


Fig. 4. Sensor response to Al target, $f_{exc} = 1$ kHz

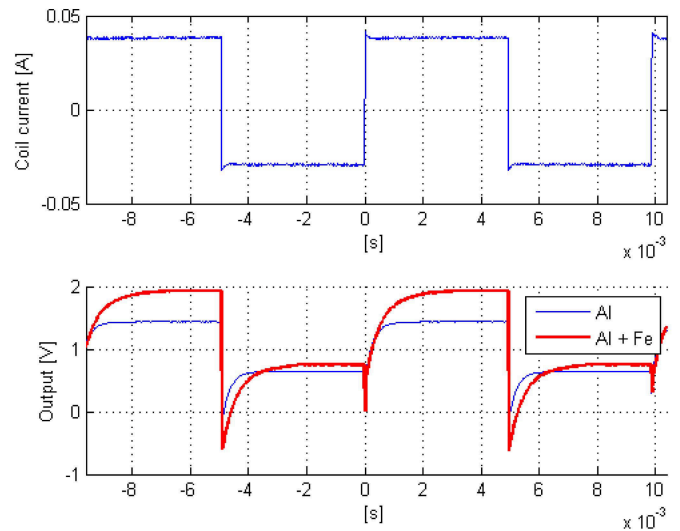


Fig. 5. Excitation current (upper trace) and the sensor response (lower trace) to Al sheath alone with the thickness below the penetration depth. The eddy currents decay fast and the magnetic field propagates through the 2.5 mm sheath, $f_{exc} = 100$ Hz. Signal belonging to the ferrous target inside the sheath is visible.

II. THE MEASUREMENTS

The prototype sensor is shown in Fig. 3.

It uses single Honeywell HMC 1001 AMR sensor and AD8429 instrumentation amplifier with the gain of 100. The sensor is inside the 46 mm diameter, 22 mm long excitation solenoid powered by 70 mA p-p squarewave current, which generates 115 A/m field at the end of the coil and 12 A/m field in 4 cm distance. The sensor is located in the coil axis at the coil end. Flipping is made using the integrated flipping coil by 1.2 A p-p current created by discharging a 6.8 nF capacitor directly coupled to the 30 V p-p square-wave excitation waveform from 50 Ω generator. Fig. 4 shows the typical response of the self-demodulated sensor to conducting target for 1 kHz excitation frequency. Basic DC shift is caused by the fact that the sensor is subjected to the full excitation field which is self-demodulated into the DC voltage. If necessary this basic DC shift can be compensated either by feedback current in the sensor or by voltage shift in the pre-amplifier. The exponential pulses are caused by eddy currents in the target. Notice that after self-demodulation all pulses have the same polarity and therefore they contribute to DC output. If the target is ferromagnetic, further DC shift is caused by its permeability. The eventual squarewave component is caused

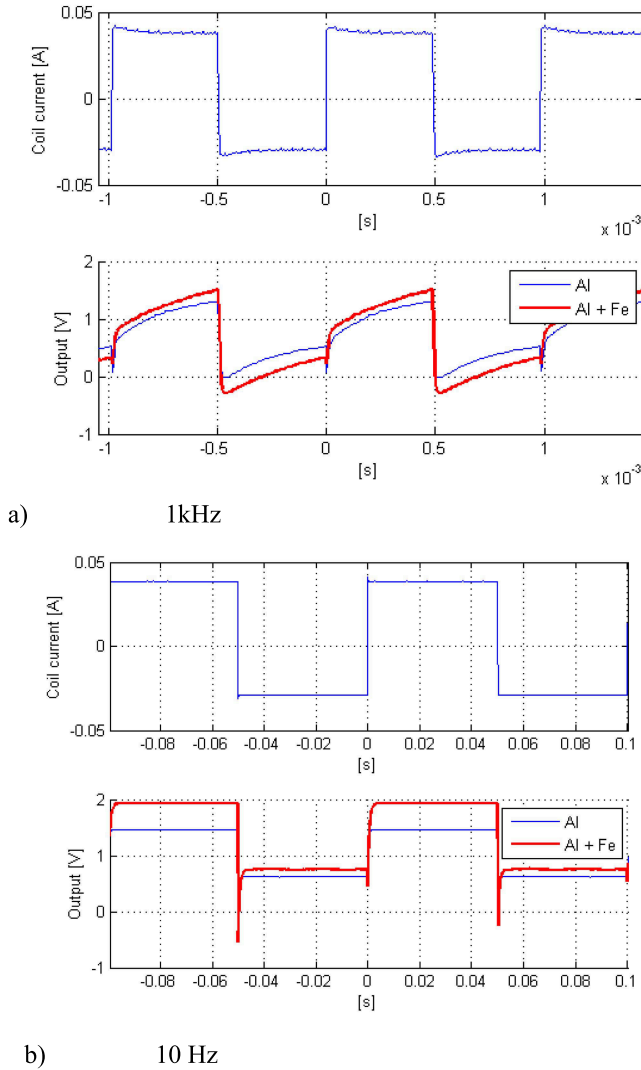


Fig. 6. Excitation current and sensor output for a) 1 kHz and b) 10 Hz. The sheath and target are the same as in Fig. 5.

by external magnetic field or (in the case of ferromagnetic target) by the target remanence.

When measuring the target position through the sheath the excitation frequency should be adjusted so that the penetration depth is larger than the sheath thickness. In such case the eddy currents decay fast and the magnetic field propagates through the sheath towards the target. This situation is shown in Fig. 5.

Fig. 6 shows sensor response also to 10 Hz and 1 kHz excitation current. While at 1 kHz the sensitivity is smaller, 10 Hz give nice response for Fe target, however the transitional part is too short for time-domain analysis. 100 Hz excitation was therefore selected as optimum for this configuration.

Fig. 7 shows the calibration of the selected setup. We measured a DC response from both ferromagnetic and aluminum targets through the same 2.5 mm aluminum sheath. The target distance is measured from the end of the excitation coil. The frequency dependence in this case is caused not only by the eddy currents in the sheath, but also in the target. Conventional induction coil at this frequency shows very small sensitivity and cannot be used.

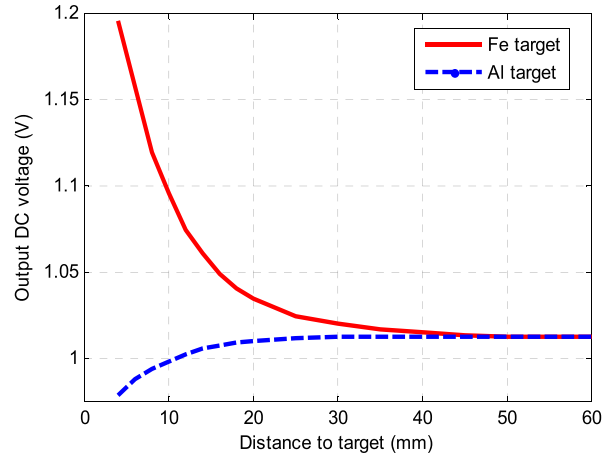


Fig. 7. DC output of self-demodulating AMR proximity detector sensing iron and Al target through 2.5 mm Al sheath. $f_{exc} = 100$ Hz.

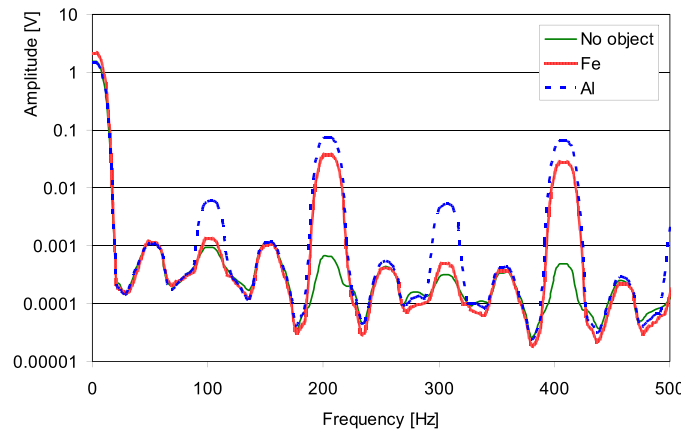


Fig. 8. Spectrum of sensor output for various targets, 100 Hz excitation, 100 Hz flipping.

III. PROCESSING OF THE AC SIGNAL

The used principle is very flexible and it allows estimating the target properties using techniques developed for eddy-current non-destructive testing and mine detection. The analysis can be performed both in the frequency and time domain.

A. Processing in the Frequency Domain

Sinewave excitation field at multiple frequencies is ideal for analysis in the frequency domain. For position sensor the overall circuit simplicity is an important aspect, which is a strong argument for using squarewave excitation. However, the signal spectrum for squarewave excitation is rather complex as illustrated in Fig. 8. The 100 Hz \pm 100 Hz signal created by mixing 100 Hz excitation with 100 Hz flipping frequencies has two products: DC which is the main sensor output and signal at 200 Hz. However, part of the 200 Hz signal comes from the third harmonic component of the excitation squarewave mixed with flipping (200 = 300-100). The 100 Hz spectrum component is caused by DC signal (including the sensor offset) modulated by 100 Hz. A small part of this signal can be also caused by capacitive or inductive feedthrough from the excitation. In general the higher even harmonics are caused by squarewave spectrum components modulated by 100 Hz signal

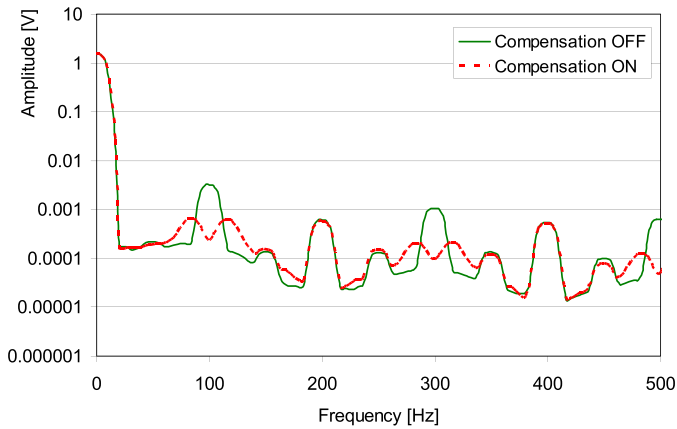


Fig. 9. Spectrum of sensor output with feedback compensation on/off in magnetic shielding.

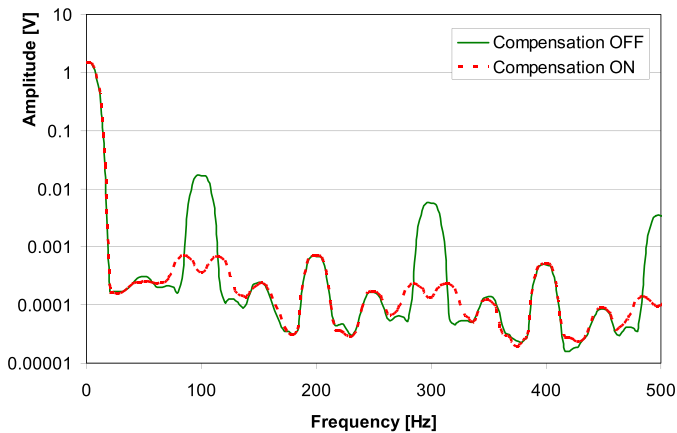


Fig. 10. Spectrum of sensor output with feedback compensation on/off in the Earth's field.

and the higher odd harmonics are caused by AMR sensor non-linearities.

B. DC Field Compensation

We have shown that the external DC field together with AMR non-linearity creates harmonics. More serious is the danger of the saturation at larger fields. Therefore we decided to employ DC field compensation. In our case the frequency band of the feedback loop is limited to 5 Hz, which leaves the 100 Hz field unaffected. The effect of the feedback compensation on output spectrum is shown in Fig. 9. In this case the sensor is placed inside the magnetic shielding, so that the DC component is caused only by the sensor offset. An unwanted consequence of the feedback compensation is the increased noise in sidebands of 100 Hz and all odd harmonics.

When the sensor is exposed to the Earth's magnetic field of 50 μT (Fig. 10) the amplitude of 100 Hz and odd harmonic components is significantly higher, confirming the origin of this signal. After compensation the spectrum is practically the same as in Fig. 9.

DC field is not the only source of the frequency of 100 Hz as shows the spectrum for the aluminum target in Fig. 8. Similar behavior was observed when an improper phase between the excitation field and the flipping current deteriorates the rectification and results in an output waveform with negative

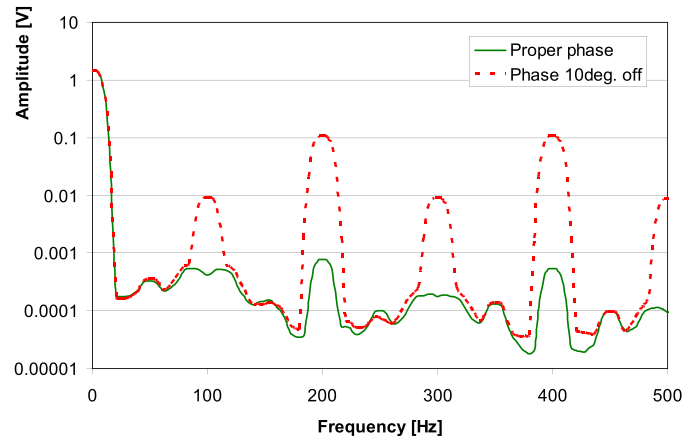


Fig. 11. Spectrum of sensor output for different phase between excitation field and flipping current with active feedback compensation.

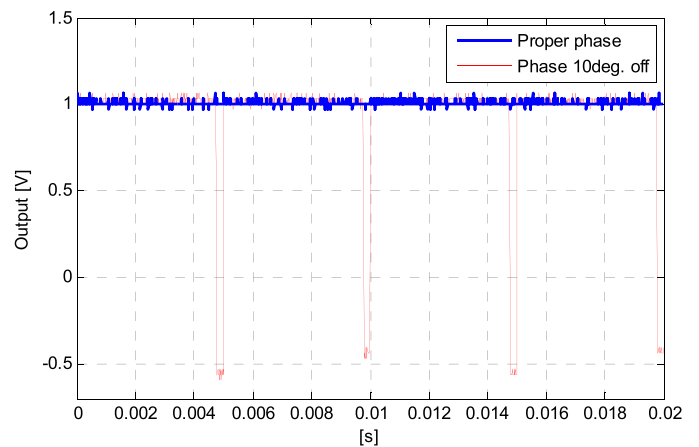


Fig. 12. Sensor output for different phase in time-domain.

peaks with the repetitive frequency of 200 Hz (Fig. 11 and 12). Deteriorated function of the feedback results in the rise of 100 Hz in the frequency domain. Due to its origin the remaining 200-Hz signal cannot be eliminated by the feedback designed for the DC field compensation. At the low excitation frequency the phase accuracy is however not critical as the largest delay in our setup was the recovery time of the AMR sensor after flipping, which was only 30 μs .

C. Signal Processing in the Amplitude Domain

Analysis of amplitude and phase shifts of shown spectra is not an easy task. Therefore we decided for time-domain signal processing, which in low-frequency case appears to be more straightforward.

For the laboratory evaluation we developed a software application based on dividing the digitized waveform into two intervals, the first one measures eddy currents and the second one the steady field of the excitation coil (Fig. 13). The digitizer was 16 bit PCI-6221 from National Instruments, where a 10 kHz sampling rate proved to be sufficient for the 100 Hz excitation.

The mean value of the signal in the first interval is a function of target conductivity, permeability and distance,

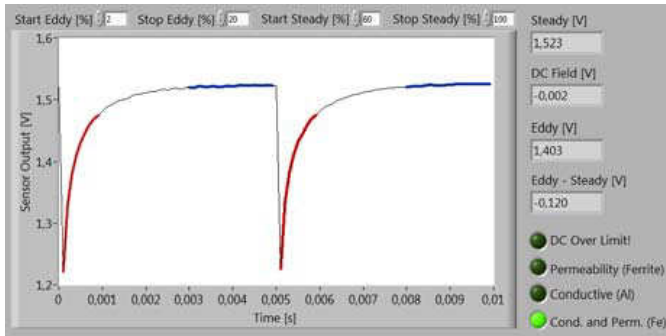


Fig. 13. Sensor DC output of self-demodulating AMR proximity detector sensing iron and Al target through 2.5 mm Al sheath. $f_{exc} = 100$ Hz. The “squarewave component” is compensated due to DC field feedback.

while the mean value in the second interval depends only on permeability and distance.

The effects of conductivity and permeability can be therefore evaluated separately using a single squarewave excitation frequency of 100 Hz. Therefore apart from proximity detection the material type is also indicated. It should be noted, that the signal amplitude also depends on the target distance and geometry. Some apriori information about the target is therefore necessary. More information can be brought by multitone excitation, technique routinely used for mine detection.

The DC field (e.g. the Earth’s field) is obtained as the squarewave component amplitude of the self-demodulated output and compensated by an external coil to suppress the non-linearity of AMR output characteristic. Thus the linear output behavior is ensured for ± 700 A/m DC field range. However the sensor frequency response, which is already low due to the low excitation frequency, is further restricted by the feedback compensation.

IV. CONCLUSION

We have shown that the proposed AMR eddy current sensor can be used at very low excitation frequency (1 to 100 Hz) to detect the position of ferromagnetic or massive conducting object covered by a metal sheath. For the first time we demonstrated the self-demodulation ability when the excitation and flipping signals have the same frequency. We have proven 40 mm detection distance for ferrous target measured through the 2.5 mm thick aluminum sheath. Using the time-domain signal analysis, it is also possible to identify the target material. The sensor also measures and simultaneously compensates the DC field component. This makes the sensor immune against external fields without shielding, which was used for this purpose in [10] and [11]. The present sensor is not differential, DC field compensation is made electronically and no suppression of the excitation field is necessary. Using gradiometric configuration for larger detection distances is also possible; the detection distance limit can be increased also by increasing of the excitation coil diameter. Final version of the intelligent position sensor should have electronics integrated into the sensor body, which will be the next step of the development.

REFERENCES

- [1] T. Reininger, F. Welker, and M. von Zeppelin, “Sensors in position control applications for industrial automation,” *Sens. Actuators A, Phys.*, vol. 129, pp. 270–274, May 2006.
- [2] M. Jagiella, S. Fericean, and A. Dorneich, “Progress and recent realizations of miniaturized inductive proximity sensors for automation,” *IEEE Sensors J.*, vol. 6, no. 6, pp. 1734–1741, Dec. 2006.
- [3] S. Fericean and R. Droxler, “New noncontacting inductive analog proximity and inductive linear displacement sensors for industrial automation,” *IEEE Sensors J.*, vol. 7, no. 11, pp. 1538–1545, Nov. 2007.
- [4] H. Bartsch, T. Geiling, and J. Mueller, “A LTCC low-loss inductive proximity sensor for harsh environments,” *Sens. Actuators A, Phys.*, vol. 175, pp. 28–34, Mar. 2012.
- [5] P.-H. Lo, S.-H. Tseng, J.-H. Yeh, and W. Fang, “Development of a proximity sensor with vertically monolithic integrated inductive and capacitive sensing units,” *J. Micromech. Microeng.*, vol. 23, no. 3, Article Number: 035013, 2013.
- [6] P. Ripka and M. Janosek, “Advances in magnetic field sensors,” *IEEE Sensors J.*, vol. 10, no. 6, pp. 1108–1116, Jun. 2010.
- [7] P. Ripka, M. Janosek, and M. Butta, “Crossfield sensitivity in AMR sensors,” *IEEE Trans. Magn.*, vol. 45, no. 10, pp. 4514–4517, Oct. 2009.
- [8] B. Marchand, J. M. Decitre, and O. Casula, “Flexible and array eddy current probes for fast inspection of complex parts,” in *Proc. Rev. Quant. Nondestruct. Eval.*, vol. 29. Kingston, 2010, pp. 385–392.
- [9] S. Tumanski, *Thin Film Magneto-resistive Sensors*. Bristol, U.K.: IOP, 2001, pp. 76–81.
- [10] M. Martino, A. Danisi, R. Losito, A. Masi, and G. Spiezia, “Design of a linear variable differential transformer with high rejection to external interfering magnetic field,” *IEEE Trans. Magn.*, vol. 46, no. 2, pp. 674–677, Feb. 2010.
- [11] A. Masi, A. Danisi, R. Losito, and Y. Perriard, “Characterization of magnetic immunity of an ironless inductive position sensor,” *IEEE Sensors J.*, vol. 13, no. 3, pp. 941–948, Mar. 2013.

Pavel Ripka was born in Prague in 1959. He received the Engineering degree in 1984 and the C.Sc. (Ph.D. equivalent) degree in 1989. He was an Associate Professor in 1996 and a Professor in 2002. He was the Dean of the Faculty of Electrical Engineering at the Czech Technical University, Prague, Czech Republic, in 2011. He is with the Department of Measurement as a Professor, lecturing in measurements, engineering magnetism, and sensors. His main research interests are magnetic measurements and magnetic sensors, in particular, fluxgate.

Jan Vyhnanek was born in Prague in 1987. He received the Engineering degree from the Faculty of Electrical Engineering, Czech Technical University, Prague, Czech Republic, in 2011, where he is currently pursuing the Ph.D. degree at the Department of Measurement. His main fields of interest are magnetic sensors and their applications in detection of metal objects.

Michal Janosek was born in Varnsdorf in 1980. He received the degree from the Faculty of Electrical Engineering, Department of Measurement, Czech Technical University, Prague, Czech Republic, in 2007, where he is currently pursuing the Ph.D. degree at the Department of Measurement, and is currently a Junior Researcher. His main research activity is the application of magnetic sensors in gradiometers and further development in PCB fluxgate sensors.

Jan Vcelak received the Ing. (M.Sc. equivalent) and Ph.D. degrees from the Faculty of Electrical Engineering, Czech Technical University, Prague, Czech Republic, in 2003 and 2007, respectively. From 2006 to 2007, he was with Ricardo Prague, where he was involved in the development of SW&HW for hybrid vehicles. In 2007, he joined the Tyndall National Institute, Cork, Ireland. Since 2012, he has been a Researcher with the Czech Technical University, Prague. His research interests include sensors (magnetometers, accelerometers, and gyroscopes), methods and electronics for inertial navigation, and compasses.

3.2.5 Linear Position Sensing through Conductive Wall without Permanent Magnet

This work is a follow-up to the previous sensor which is able to detect objects behind a conductive shield (3.2.4). Instead of the AMR sensor, an integrated fluxgate sensor was used, which has greater input range and all the analog electronics provided on-chip including fast feedback compensation. To keep the design simple, signal demodulation is provided by software after digitization.

16 sensors are mounted on a PCB to create an array for linear position measurement. Low frequency excitation allows metallic objects to be detected behind an aluminum wall. To pursue a practical application, a model of an aluminum pneumatic cylinder was built and position of the iron piston rod was detected.

The principle for position detection of the piston rod lies in deformation of the excitation field which appears at the end of the rod. When the sensors are positioned perpendicular to the excitation field and parallel to the iron rod axis, the end of the iron rod creates a distinct peak in the sensor array data.

The output of the position sensor is continuous and two interpolation methods were tested for this purpose. Because the output of the sensor array approximates the response peak in discrete locations, the knowledge of the shape of the response peak allows a fitting method to be applied to the output signals. The fitting method had lower position error than the simple method of weighted average.

The position error of the sensor which is reaching ± 2 mm, can be further lowered by decreasing the spacing of individual fluxgate sensors to meet the industry demands. However further measurements which were out of the scope of this conference paper, showed a strong influence of motion dynamics on the output of the position sensor. Given the available industry-standard Hall sensors with a higher bandwidth, practical application of this position sensor for pneumatic cylinders can be considered only in very special cases, such as a restricted use of a permanent magnet, while ferromagnetic rod is available and with low motion dynamics demands. So this paper should be treated as a demonstration of a new principle of position measurement rather than a practical sensor development for pneumatic cylinders.

Proceeding

Linear Position Sensing through Conductive Wall without Permanent Magnet

Jan Vyhnánek^{1,*}, Pavel Ripka¹ and Andrey Chirtsov¹

¹ Faculty of Electrical Engineering, Czech Technical University, Technická 2, 166 27, Prague, Czech Republic

* Correspondence: vyhnajan@fel.cvut.cz; Tel.: +420-224-352-178

Presented at the **EuroSensors 2017 Conference**, Paris, France, September 3–6, 2017.

Received: date; Accepted: date; Published: date

Abstract: A linear position sensor for pneumatic actuators is presented. Position of the piston rod made of ferromagnetic material is detected by low frequency magnetic field which penetrates the aluminum wall of the cylinder. The sensor consists of an array of integrated fluxgate sensors and two excitation saddle coils mounted outside the actuator. The method does not need a permanent magnet attached to the piston as required by common magnetic position sensors.

Keywords: position sensor; fluxgate; pneumatic actuator

1. Introduction

The presented sensor is motivated by application of position sensing through conductive sheath presented in [1]. A low frequency magnetic field excitation penetrates thin conductive material and allows to detect metallic objects behind it. Active excitation allows synchronous demodulation of sensor signal to suppress off-band noise fields including DC. In the study ([1]) a 100 Hz excitation was used to detect position of objects through a 2.5 mm thick aluminum wall.

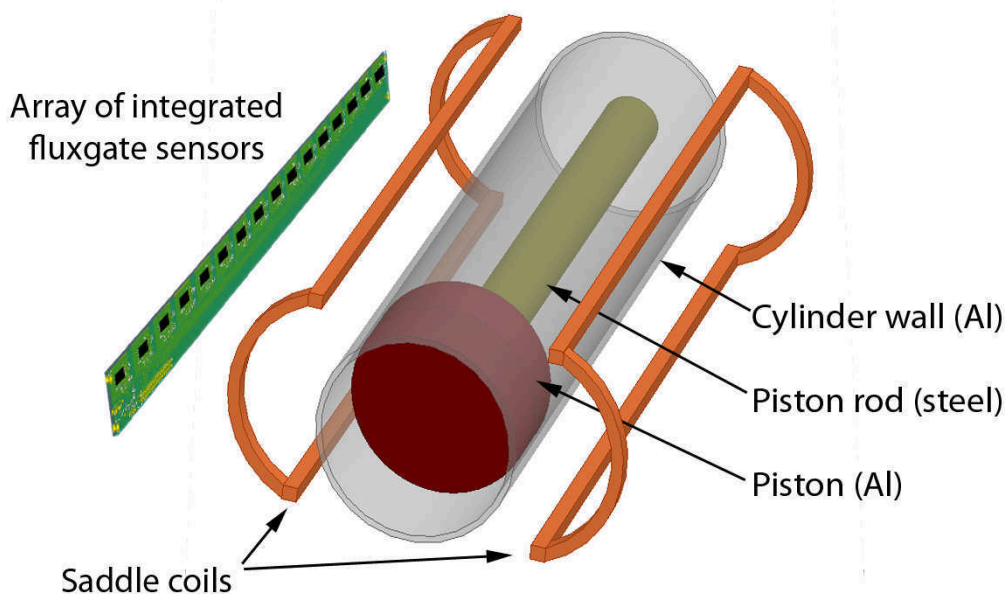


Figure 1. The position sensor consists of an array of integrated fluxgate sensors and two excitation saddle coils. The sensor is attached onto the pneumatic cylinder wall and has no moving parts.

This method can be used for position detection of a piston in a pneumatic actuator which has usually an aluminum wall. So far for position sensing a permanent magnet had to be installed in the piston and a DC-field sensor detected its position [2]. Magnetic field of the permanent magnet then has to be strong enough to ensure good signal to noise ratio to suppress DC field noise.

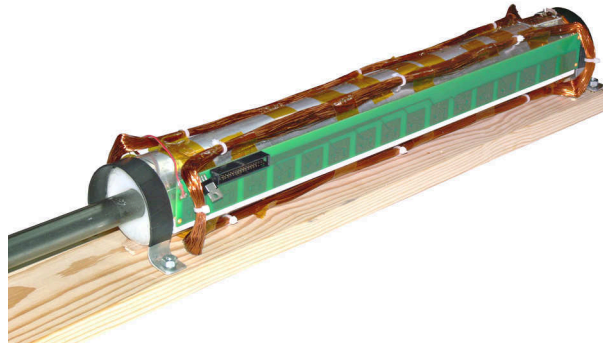


Figure 2. The actual position sensor is made of 16 integrated fluxgate sensors and is attached to the pneumatic actuator model which is 50 cm long and 6 cm in diameter

2. Materials and methods

The proposed sensor does not need modifications to the piston; it is installed externally on the actuator wall (Figure 1, 2). The magnetic field response of the steel rod to the radial excitation field is sensed by integrated fluxgate sensors in axial direction (Figure 3).

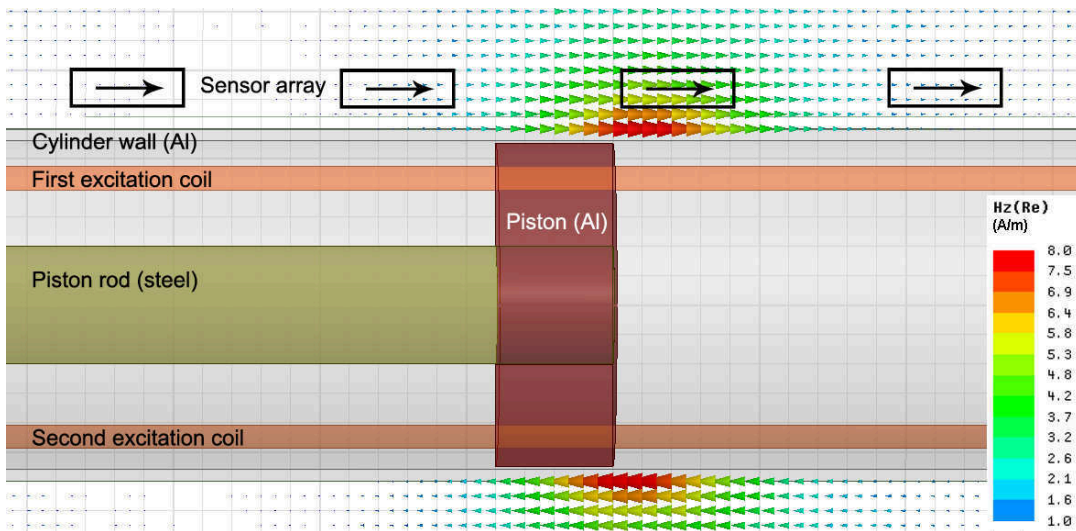


Figure 3. Magnetic field component in axial direction outside the pneumatic cylinder simulated by FEM. Excitation field of 4 Hz in radial direction penetrates the aluminum wall and is substantially deformed near the end of the piston rod made of common magnetizable steel. Sensors are oriented in the axial direction and perpendicularly to the excitation field.

Each sensor output was evaluated by a synchronous demodulator implemented in software due to high number of channels (Figure 4). The measurement setup is suitable for assessment of sensor parameters, however for application e.g. in a feedback controlled system a real-time system is needed to eliminate a variable delay.

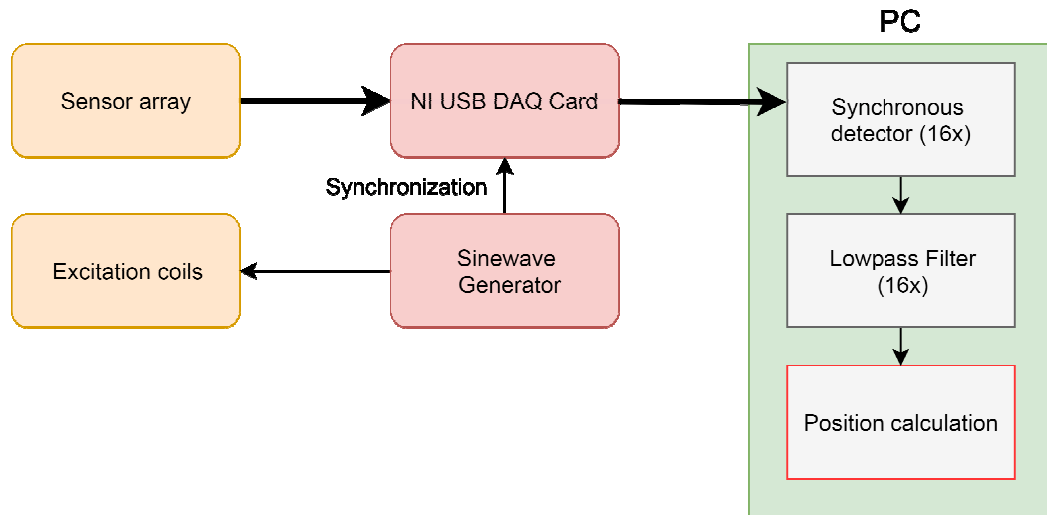


Figure 4. Schematic diagram of signal processing.

3. Results

The response of the steel rod is frequency dependent. At very low frequencies only permeability effects contribute to the signal, at 64 Hz eddy current effects change noticeably the shape of characteristics (Figure 5). The selection of the used excitation frequency depends on the required dynamic properties of the designed sensor. We evaluated the error of position measurement with excitation frequency of 32 Hz and 16 sensors in the array with 3-cm spacing.

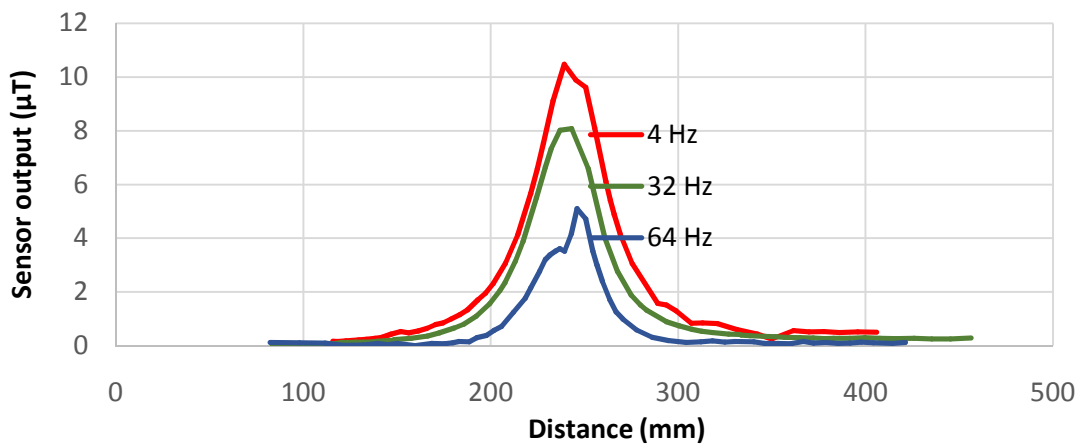


Figure 5. Single sensor output vs. piston position for excitation frequency of 4 Hz, 32 Hz and 64 Hz.

To process the 16 output values of the sensor array the following methods were examined:

1. The simplest approach is to find the maximum value and provide the position of the respective sensor. The position error is half of the spacing of sensors, in our case ± 15 mm.
2. Weighted average method $\sum(\text{output}_i \times \text{distance}_i) / \sum \text{output}_i$ reached an error of ± 5 mm, see Figure 6. For noise reduction the weighted average is computed using only the three sensors with the maximum output. The error is three times better than the “maximum output” method with only moderate computing capacity requirements of a final microprocessor-based

processing circuit.

- Least squares fitting method minimized the formula $\sum(\text{output}_i - \text{estimated_output}_i)^2$, where the estimated output function is known by the single-sensor measurement in Figure 4. This output function is supposed to be the same for all 16 sensors. The only unknown coefficient of the model is the distance shift, so the computation time is reasonable. This method reached the position error better than ± 2 mm (Figure 6). Disadvantage of this method is that the output function is likely to be different between distinct cylinder types and needs to be measured. Further improvement of accuracy would provide a lookup table method with a laborious calibration throughout the full range with a fine step.

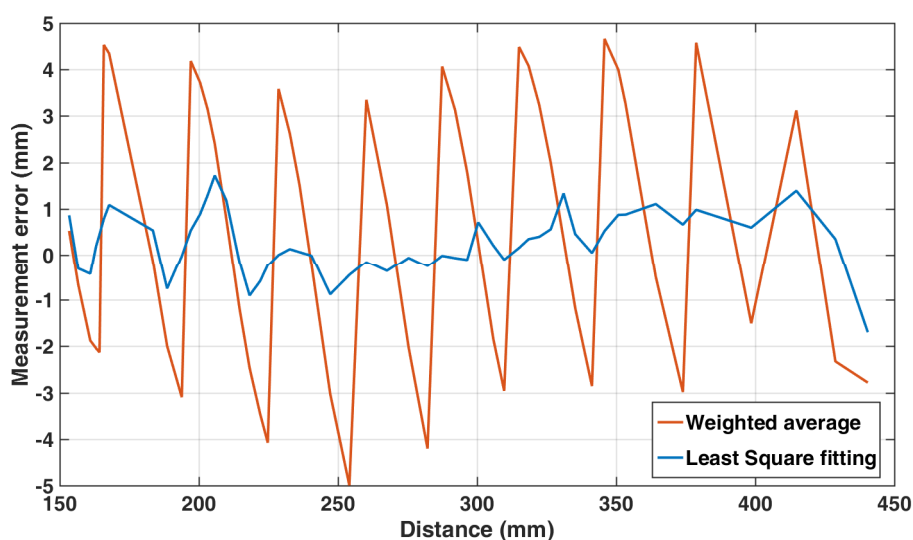


Figure 6. Positioning error throughout the central 300 mm stroke of the pneumatic actuator

4. Discussion

The sensor has no moving parts and is suitable e.g. for retrofit applications where magnet for position sensor is missing. The measuring principle needs a common magnetizable steel rod rather than stainless steel one which is however more expensive and less usual. Due to the low amplitude of the signal measured, which is about 1/1000 of the amplitude provided by a piston magnet, the position sensor is susceptible to the background magnetic noise. However if the noise is limited to a specified frequency, it can be avoided by shifting the excitation frequency.

References

- Ripka, P.; Vyhnanek, J.; Janosek, M.; Vcelak, J. AMR Proximity Sensor with Inherent Demodulation. *IEEE Sens J* **2014**, *9*, 3119-3123, DOI: 10.1109/JSEN.2014.2325406.
- Reininger, T.; Welker, F.; Von Zeppelin, M. Sensors in position control applications for industrial automation. *Sens Act A: Phys* **2006**, *129*, 270-274, DOI: 10.1016/j.sna.2005.09.056.



© 2017 by the authors. Submitted for possible open access publication under the terms and conditions of the Creative Commons Attribution (CC BY) license (<http://creativecommons.org/licenses/by/4.0/>)

3.2.6 Localization of the Chelyabinsk Meteorite From Magnetic Field Survey and GPS Data

This chapter demonstrates the application of DC magnetic field sensors for mapping of remanent magnetic fields and fields induced by the effects of magnetic susceptibility in the Earth's field. A typical application is a buried bomb search. All the detectors in the previous paper are able to detect DC fields as well, but at small distances the AC mode of the detectors proved more suitable for visualization and proximity detection.

On the other hand, for long distances an AC excitation is not practical, because the usable excitation field is limited to the vicinity of the excitation coil. Increasing the coil diameter partially mitigates this problem. But for DC sensors the detection distance is almost unlimited given the object is a source which is strong or large enough in physical size to provide a detectable field at a given distance.

The effect of strong distant sources complicates data interpretation in the DC method compared to the AC method. A gradiometer setup can suppress the homogeneous Earth's field and partly also geology features, but for size and depth estimation a magnetic field map or multiple scans capturing a magnetic anomaly are necessary. Compact objects appear usually as a dipole, the orientation of which depends on the remanent field and direction of the Earth's field. In the paper, a model fitting was used to obtain the size and depth of discovered objects. Fluxgate sensors were used due to higher sensitivity than AMRs have and differential GPS was used for centimeter-level position sensing.

Localization of the Chelyabinsk Meteorite From Magnetic Field Survey and GPS Data

Gunther Kletetschka, Jan Vyhnanek, Darja Kawasumiova, Ladislav Nabelek, and Vojtech Petrucha

Abstract—The Chelyabinsk meteorite fragment that landed in the Chebarkul lake in Russia on February 15, 2013 weighed over half a ton. We provide magnetic field maps that were obtained during underwater measurements above the fragment. The data acquisition process was multiple global position system referenced magnetic surveys 0.5–1 m above the top of the lake sediment layer at 10 m water depth. Gradiometric configuration of the survey using two triaxial fluxgate magnetometers helped to suppress local geological anomalies. The location of the ice crater and the underwater magnetic anomaly provided final meteorite landing coordinates, which were made available during meteorite recovery.

Index Terms—Gradient methods, fluxgate sensor, global positioning system, meteorite search.

I. INTRODUCTION

CHELYABINSK bolide parameters indicated that the largest solid fragment surviving the decomposition by heat in the atmosphere landed in Lake Chebarkul, near the city of Chebarkul, on 15 February 2013. The Chelyabinsk meteorite is a rare end product of super bolide, whose initial mass started to defragment and evaporate over the Chelyabinsk region [1]. The initial body reduced down to the largest surviving fragment, with a mass of approximately 600 kg, which plunged through the 80 cm thick ice covering the water of Lake Cherbarkul. Its observed trajectory was 254 km long with an azimuth of 279.5° , and a slope of 16.5° to the horizontal. The speed was 4.3 km/s at the end of registration time at position of 54.922° N latitude, 60.606° E longitude, 14.94 km altitude [1], [2]. The largest fragment landed in Lake Chebarkul, where an 8 m diameter circular opening in ice was found shortly after this meteorite event. Fragments from the bolide event were collected soon after the fall and were of an ordinary chondrite composition [3] with

Manuscript received March 11, 2015; revised May 7, 2015; accepted May 10, 2015. Date of publication May 20, 2015; date of current version July 7, 2015. This work was supported in part by MEYS Grant LK21303, in part by Research Plans of the Institute of Geology AS CR RVO67985831, and in part by the Czech Science Foundation under Grant 13-39088P. The associate editor coordinating the review of this paper and approving it for publication was Prof. Kazuaki Sawada.

G. Kletetschka and L. Nabelek are with the Faculty of Science, Charles University in Prague, Prague 116 36, Czech Republic, and also with the Institute of Geology, Academy of Sciences of the Czech Republic, Prague 117 20, Czech Republic (e-mail: gunther.kletetschka@natur.cuni.cz; nabelek1@natur.cuni.cz).

J. Vyhnanek and V. Petrucha are with the Faculty of Electrical Engineering, Czech Technical University in Prague, Prague 166 36, Czech Republic (e-mail: jan.vyhnanek@fel.cvut.cz; vojtech.petrucha@fel.cvut.cz).

D. Kawasumiova is with CaJ Ltd., Prague 129 99, Czech Republic (e-mail: darjakawasumi@gmail.com).

Color versions of one or more of the figures in this paper are available online at <http://ieeexplore.ieee.org>.

Digital Object Identifier 10.1109/JSEN.2015.2435252

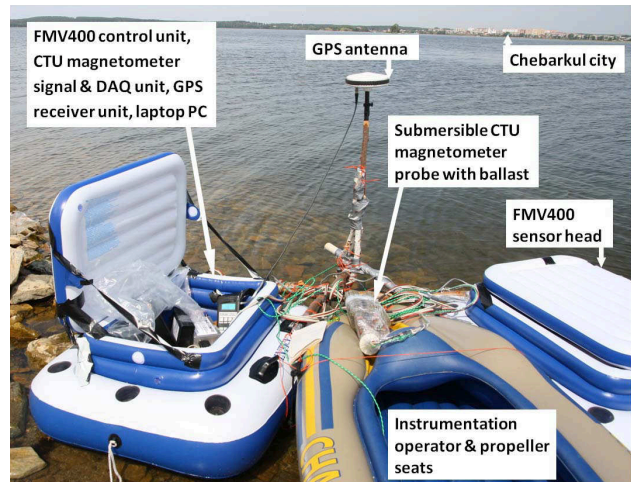


Fig. 1. Improved non-magnetic vessel equipped with instrumentation for GPS referenced magnetic survey.

iron/nickel component, providing a potential for magnetic detection [4]–[7]. On 5 March, our team arrived at the site and obtained Global Position System (GPS) coordinates of the crater (using a commercial Garmin 76 unit) whose boundary was outlined by wooden sticks inserted in the ice. A surface magnetic survey was done at this time using a single vector fluxgate magnetometer. An underwater magnetic survey of the impact site was performed on 19–22 June 2013 using a gradiometric configuration of two vector fluxgate magnetometers. Here we present a description of the hardware used for the survey, the results of the instrument calibration, the methodology of the magnetic and GPS data evaluation, and synchronization. Final survey results are confronted with simulations and information obtained during the meteorite recovery on October 2013.

II. INSTRUMENTS AND METHODS

In our magnetic survey and mapping we used a non-magnetic inflatable boat to cross the water surface in the area where the opening in the ice was created by meteorite impact in the winter. There were three substantial instruments: a geodetic-grade GPS system for precise positioning, one submersible fluxgate magnetometer (developed by CTU in Prague), and one on-board commercial fluxgate magnetometer (MEDA Inc.) that were used for magnetic measurements. There was also a laptop computer present in the boat, which served as a user display and logger for magnetic data (see Fig. 1). The GPS data were stored directly in the instrument and processed offline.

Meteorite localization by magnetic gradiometry was a very similar task to Unexploded Ordnance (UXO) detection, although the anomaly intensity is supposed to be significantly lower for the chondrite type meteorite. The authors deal with UXO detection in ground [8], [9] or underwater [10]–[13] conditions using various instruments and techniques. We considered the application of multi-sensor instruments measuring simple magnitude gradient or even full gradient tensor. The benefits of this multi-sensor approach include higher spatial resolution, wider coverage, and thus faster scanning. We finally decided to use the presented concept of two vector magnetometers because of a high potential risk of loss of the underwater probe (e.g. due to unknown underwater obstacles) and the limited carrying capacity of the expedition. Another suitable instrument developed at our laboratory was still in a test phase [14].

A. GPS for Accurate Positioning of Gradient Measurements

Ashtech's ProMark 2 GPS system was operated in differential mode utilizing a fixed base station and mobile rover receiver, thus reaching centimeter-level accuracy for relative positioning. The rover antenna was positioned above the submersible probe of the magnetometer to follow its position. The speed of the survey was 0.3 m/s at maximum and 0.1 m/s on average to avoid horizontal separation between the probe and antenna. With regards to relative positioning, simultaneous logs of the base and rover station included pseudo-range and carried-phase data, which enabled improved accuracy. Post-processing of the raw data in Ashtech Solutions software indicated the accuracy of each recorded point, which was 3 cm RMS in the worst case of all of the measurements.

The base station unit logged data in a static position. There were two substantial conditions to ensure the desired accuracy: an unobstructed sky view to receive the maximum number of satellites and a solid stand for the antenna. Most of the surrounding terrestrial area was covered with forest and the only suitable place was a sandy area near the anchorage. The antenna was placed on a 2 m tall wooden pole. Each day the base antenna was placed onto the pole, so the only additional error between measurements on different days was the antenna spatial shift after reassembling the base station. The wooden pole was kept on the site and no apparent shift of the pole was noticed between the days of the survey. The positioning error of the antenna attached to the pole was estimated to be 2 cm at maximum.

For absolute positioning in the world coordinate system, the absolute position of the base station was estimated. The most credible method was to place the rover unit on a known geodetic point, so the position of the base was estimated with the accuracy of the relative positioning. Unfortunately, there were no such points available in the survey area. We used data averaging of the long-lasting base station log. Apart from the simple averaging, we used an on-line service Precise Point Positioning (PPP) [15].

The PPP service applies corrected information of satellite orbits and atmosphere conditions for post-processed calculations. We used this to estimate the absolute position in Prague

prior the actual survey. The base antenna was positioned in Prague at a point with known coordinates. The log took about 20 minutes in the area with restricted sky view due to buildings. The averaged point was 10.5 m away from the real coordinates. The PPP point showed a ten times lower error, about 1 meter, the indicated standard deviation was 3.3 m.

Three long-lasting base station logs were recorded at Chebarkul Lake: each lasted for about 4 hours. These were selected for averaging and PPP post-processing. Both averaging and PPP gave similar results for these 4-hour logs. We selected the PPP positions for the final coordinate calculation, given the Prague results. The PPP service indicates standard deviations of the estimated positions, which for our data were 1.7 m, 1.5 m, and 1.5 m (day 1, 2, 3, respectively). Assuming independent observations, the final base station coordinates are the result of averaging the three PPP points, each of which was obtained during one day of the magnetic survey. The final coordinates are in the WGS84 system: 54.95828749° N, 60.31818468° E with 0.9 m of combined standard uncertainty.

Synchronization of GPS with magnetometers and mapping positional accuracy needs to account for the fact that GPS and magnetometer data were logged separately and that for data synchronization we used timestamps from magnetometer logs. Time for both magnetometers was derived from the computer clock. The computer clock was manually synchronized each day at the beginning of the survey using a GPS receiver. The accuracy of the time synchronization t_{e_sync} was estimated to be ± 0.5 s. Position error s_{e_sync} in magnetic maps due to the limited synchronization accuracy can be obtained for each point according equation (1). The maximum velocity v during the survey (on 19.6. 2013) was 0.3 m/s, which is similar to other days. So the maximum positioning error is ± 0.15 m.

$$S_{e_sync} = V \cdot t_{e_sync} \quad (1)$$

B. Surface Fluxgate Vector Magnetometer (MEDA FVM400)

This compact commercially available tri-axial vector fluxgate magnetometer was used during the first visit to Chebarkul Lake on March 2013 for surface magnetic field mapping. It was used as a surface magnetometer to create a gradiometric configuration for magnetic field mapping during the final measurements on June 2013. The magnetometer has a digital data output (RS232 interface) with 1nT resolution and 1 Sa/s sample rate. The three vector components (X, Y and Z) provided the vector magnitude. The magnetometer offers National Institute of Standards and Technology traceable calibration, but a scalar calibration [16] has been performed to verify and improve its precision. We used a non-magnetic positioning device [17] to precisely collect 55 different vectors of the Earth's magnetic field. The calibration procedure was performed twice and the results are summarized in Table 1. The accuracy of the magnetic field vector magnitude measurement has been improved by a factor of 9 (reduction of magnitude peak-peak variation from 142 nT to 16 nT for differently oriented vectors). As indicated by the results, the sensitivities are well factory

TABLE I
MEDA FMV400 SCALAR CALIBRATION RESULTS

Axis	X	Y	Z
Sensitivity [-]	0.9997	0.9999	0.9997
Orthogonality [°]	0.0926	0.1024	0.0408
Offset [nT]	-3.6	-14.7	-8.9

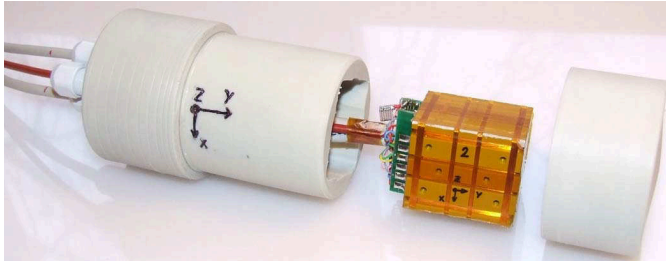


Fig. 2. Vector compensated tri-axial fluxgate sensor before embedding into a watertight package (sensor dimension 48 mm × 40 mm × 40 mm). The sensor was developed at CTU in Prague.

calibrated but the improvement comes from the calibration of the orthogonality angles.

Although the instrument noise was stable within units of nT during its testing, the recorded data showed up to 40 nT peaks, which were neither related to the real magnetic signal nor other electronic disturbance (verified). Given that these peaks are present only when the sensor is moving (e.g. waves on the lake), they suggest that an FMV400 is not suitable for dynamic measurements. Smoothing the raw waveform with a 20-second moving average resulted in acceptable data for further processing, although this allows only low-frequency homogeneous disturbances to be compensated in the differential data.

C. Submersible Vector Fluxgate Magnetometer

The magnetometer used for underwater survey (DIGMAG) was developed at the Department of Measurement of the Faculty of Electrical Engineering of the Czech Technical University in Prague. The research instrument is a vector compensated tri-axial vector fluxgate magnetometer [18], which has been modified for underwater operation. An improvised watertight plastic package filled with two-component silicone adhesive provided the desired water resistance (see Fig. 2). The sensor head was connected by an 11 m long cable to the signal conditioning and data acquisition electronics carried in the boat. The fluxgate magnetometer sensor head was based on three single-axis ring-core fluxgate sensors, which were embedded into a cuboidal compensation structure. The vector compensation improved the linearity of the sensor by virtually eliminating the cross-field errors and improved the overall stability of the sensor's calibration parameters. The magnetometer had a measurement range of $\pm 100 \mu\text{T}$, the analog signal noise was below $20 \text{ pT}/\sqrt{\text{Hz}}$ at 1 Hz, the effective digital resolution was below 100 pT at sample rate of 10 measurements per second, and the offset temperature dependence was 0.1 - 0.5 nT/°C.

The magnetometer was calibrated before the actual survey to assure the best possible performance. The total vector

TABLE II
CTU FLUXGATE MAGNETOMETER SCALAR CALIBRATION RESULTS

	X	Y	Z
Sensitivity [-]	1.0041	0.9904	1.0668
Orthogonality [°]	-0.3910	-0.0019	-0.0501
Offsets [nT]	9.73	-2.91	13.96

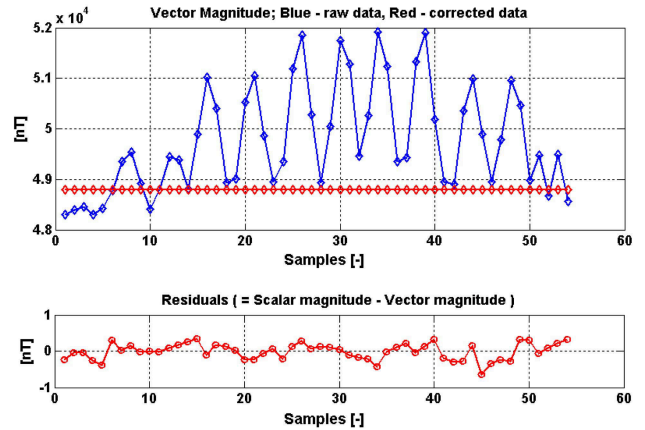


Fig. 3. Comparison of the calculated vector magnitude (vertical axis) before and after scalar calibration (top). Residuals are within 1 nT range (bottom). The calibration is essential for reaching good measurement results.

magnitude was used for the gradient measurements to allow scalar calibration. Scalar calibration did not calibrate the sensor's sensitive axes orientation with respect to external reference frame because it is not needed when only the vector magnitude is calculated. The results of the scalar calibration (average of three calibrations) are presented in Table 2. The peak-peak value of magnitude variance was reduced from 3613 nT to 0.974 nT. The main effect came from the calibration of the sensitivities and orthogonality angles. Fig. 3 shows the difference between calibrated and non-calibrated magnitude for different (uniformly distributed) vectors. The regular pattern of the "raw magnitude" came from the positioning sequence. The ambient field was monitored by an Overhauser scalar magnetometer GEMSYS GSM-19 during the calibration (and was used in the data processing).

D. Magnetic Gradient Data

We obtained the magnetic field gradient by subtracting the calculated total field from the submersible and surface probes. Homogeneous fields affecting both probes were eliminated this way and the gradient anomalies were more pronounced. In this case, the improvement was limited to low frequencies. FMV400 logged with a 1-second interval but the data had to be smoothed with a 20-second moving average filter (see section B). The geomagnetic field was quiet during the measurement (see data from Novosibirsk Observatory - www.intermagnet.org, [19]) and relevant magnetic anomalies were apparent even without computing the gradient.

The submersible probe detected a low frequency (0.1 Hz) signal, mostly along the x axis (20 nT peak to peak), which

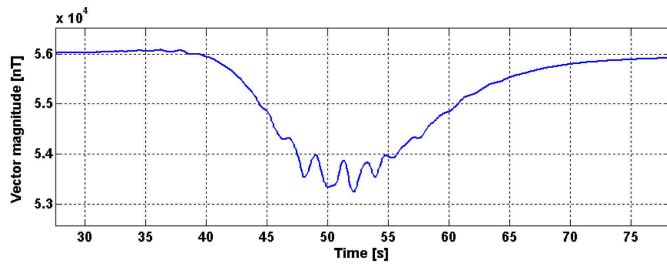


Fig. 4. Effect of waves on measured vector magnitude while crossing the magnetic anomaly area with high gradient.

was attributed to periodic rotation of the probe along the vertical axis. The submersible probe was equipped with ballast (five glass bottles filled with sand) but there was no fin to stabilize the sensor. This effect was probably due to a minor change in the calibration parameters that was induced by the internal pressure in the submersible magnetometer probe; otherwise this effect would not be visible in a gradient free area. The boat was too small (~ 3.5 m) to compensate the influence of water waves. Therefore, the rope with sensor was moving up and down in rhythm with the waves. When looking closely at the data, the magnetometer sensor in a gradient field showed a frequency signal that closely matched the frequency of the waves (see Fig. 4). These error sources were filtered out to reveal the actual anomalies, which have a lower time frequency because the scanning speed was slow (0.1-0.3 m/s).

III. RESULTS

A. Magnetic Field Survey

The first measurement (March 5) with a single surface operated magnetometer showed a magnetic anomaly of about 80 m N-W of the ice crater. When we used two probes, the differential data indicate a geologic source (e.g. boundary of two geological units) because both magnetometers (i.e. the MEDA measuring on the surface and DIGMAG at 9.5 m depth) show comparable offsets.

Near the crater multiple scans revealed a major magnetic anomaly that was easily detectable by the submersible probe but not by the surface probe. The profiles over the anomaly were selected for the speed of the boat not exceeding 0.1 m/s and were used for further processing. The spatial shift of scans was caused both by the position shift of the GPS antenna and the submersible sensor on a 9.5 m long rope. Therefore, scans at a low speed with smooth narrow movement are preferred. Fig. 5 shows the result of the magnetic survey done during one day.

To align the scans, we developed the following rules. Minimum speed implies minimum spatial shift, and vice versa. Scans in opposite directions have opposite spatial shifts, the scans can be centered if the speed is similar. Once the scans are merged, a dipole-like map of the anomaly can be created. Three dimensional representation of the detected anomaly showed anomaly dominance against the geomagnetic field, which points to the remanent nature of the magnetic source. Fig. 6 presents the final magnetic gradient map that is composed of multiple surveys done during the three days of measurements at Chebarkul Lake. A significant magnetic

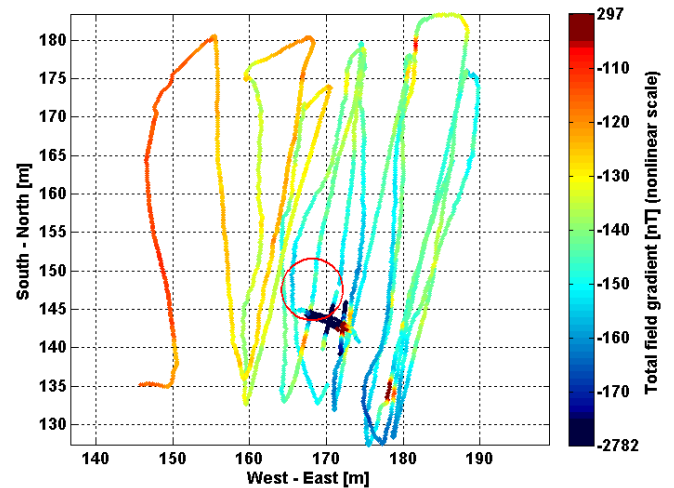


Fig. 5. Magnetic survey results (one day crossing), the red circle shows the probable ice crater position, coordinate axes indicate distances from the base station located at 54.95828749° N, 60.31818468° E.

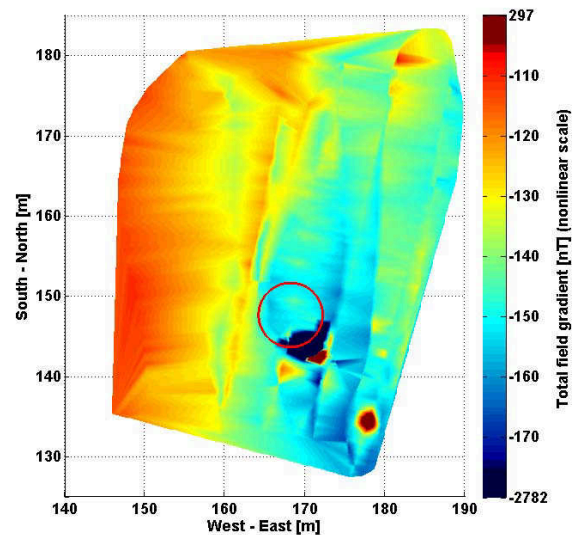


Fig. 6. Multiple survey data combined into one picture.

anomaly is visible at the S-E rim of the supposed ice crater position. The anomaly has a maximum amplitude of 3000 nT (peak - peak) at 9.5 m below water level. However, the $1/r^3$ dipole field decay makes its surface detection difficult (i.e. there are few nT gradient levels). There is another anomaly with lower amplitude (450 nT) visible approximately 12 m in a S-E direction from the supposed crater rim, which may be a smaller fragment that has detached from the main meteorite body. The effect of the approaching bedrock is visible in the West side of the map.

Although the GPS antenna - sensor spatial shift error is systematic and is compensated by the corrections, the number of high quality scans is low and the spatial shift error cannot be perfectly eliminated. Considering the values of position corrections applied (e.g. for Y position: 0.6 m, 0.8 m, -0.8 m, 1 m, and 0 m), the error caused by the sensor spatial shift plus the error of estimating the anomaly center should be at maximum ± 1 m. With this error estimation, we determined the resulting coordinates of the anomaly center (Fig. 7) as:

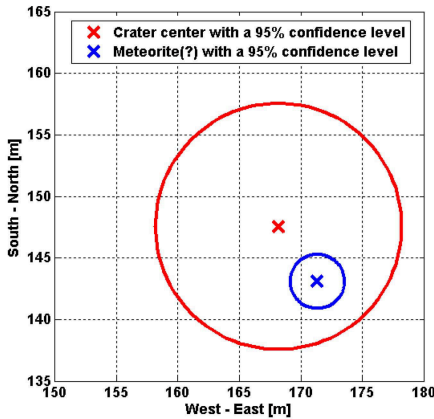


Fig. 7. This chart shows the uncertainty circles of position of both the meteorite impact location (ice crater) and predicted location of the largest meteorite fragment. The axes have their origin at base station coordinates at 54.958287° N, 60.318185° E.

54.959631° N 60.320772° E. For the absolute accuracy evaluation we combine position uncertainties of synchronization u_{sync} , relative positioning u_{rel} , and uncertainty of dipole position u_{pole} , base u_{base} , and rope lag $u_{\text{rope_lag}}$ (2). Coverage factor $k=2$ determines confidence interval of 95% to 2.2m.

B. Ice Crater and Meteorite Position

The horizontal shift of the ice crater and magnetic anomaly center is 5.5 m. The meteorite anomaly center was estimated with the absolute positioning accuracy of 2.2m, thus the confidence circle has a diameter of 4.4 m. The crater center was estimated with a Garmin GPS receiver using the internal averaging feature. Its operating manual states that it has an accuracy <10 m, 95%, and does not specify the accuracy of averaging. So the error of 10 m for the confidence level 95% is further considered. The confidence circle has a diameter of 20 m and, therefore, the confidence circles of both locations are overlapping (see Fig. 7)

$$\begin{aligned}
 u_{\text{total}} &= \sqrt{u_{\text{sync}}^2 + u_{\text{rel}}^2 + u_{\text{pole}}^2 + u_{\text{base}}^2 + u_{\text{rope_lag}}^2} \\
 &= \sqrt{\left(\frac{S_{\text{sync}}}{\sqrt{3}}\right)^2 + u_{\text{rel}}^2 + \left(\frac{S_{\text{pole}}}{\sqrt{3}}\right)^2 + u_{\text{base}}^2 + \left(\frac{S_{\text{rope_lag}}}{\sqrt{3}}\right)^2} \\
 &= \sqrt{\left(\frac{0.15}{\sqrt{3}}\right)^2 + 0.03^2 + \left(\frac{0.02}{\sqrt{3}}\right)^2 + 0.9^2 + \left(\frac{1}{\sqrt{3}}\right)^2} \\
 &= 1.1\text{m}
 \end{aligned} \tag{2}$$

IV. SIMULATIONS AND DISCUSSION

Simulations taking into account the published magnetic properties [20] suggest that the meteorite was sitting in the very upper layer of the sediment, approximately 10-12 m below the water surface (the sediment started in the depth of 9-11 m). We used several methods for the simulations (i.e. Finite Elements Methods simulations using ANSYS and Flux3D, experimental modeling - dike model and other), considering permanent magnetization as well as

susceptibility effects. The simulations confirm the measurement if high values (60 Am^2) of magnetic moment are used in calculations. The meteorite fragment could have been magnetically influenced by the people who tried to pick up small meteorite fragments using strong permanent magnets shortly after the incident. This also brings the possibility that the anomaly was modified by permanent magnet(s) left at the site, which could create a magnetic footprint of similar amplitude.

The main fragment of the Chelyabinsk meteorite (mass of 540kg) was recovered from the bottom of Cherbarkul Lake on 16 October 2013 [21]. Unfortunately, there is no detailed information available concerning the recovery process (e.g. precise GPS coordinates and how deep was the meteorite initially buried in the lake sediments were not provided). The magnetic moment of the recovered main fragment is also unknown. Reference [21] mentions ultrasonic sonar was used to detect the meteorite, but also mentions that the search area was $\sim 35 \times 30$ m and the divers used multiple pumps to remove large quantities of the sediment. Consequently, it is impossible to confirm our results or those of the other groups [22] who used different methods (GPR). The results of surface measurements of magnetic gradient at the crater location are presented in the supplementary information of [23]. The gradient map shows a magnetic anomaly located at a similar position with respect to the ice crater, but the presented GPS coordinates points to a location shifted by 28 m to the south.

V. CONCLUSION

Our GPS referenced magnetic survey attempted the absolute localization of both the impact in the ice crater and the final position of the major meteorite fragment from the Chelyabinsk event. Data analysis revealed that the impact location in the ice was centered at 54.95967° N and 60.32072° E, with a 95% confidence circle that has a diameter of 20 m. The magnetic anomaly indicates the possible location of the largest fragment of the meteorite that broke through the ice. This location was centered at 54.959631° N and 60.320772° E, with a 95% confidence circle that has a diameter of 2.2 m. Magnetic numerical and experimental modeling suggests that the source of this magnetic anomaly was shallow, probably not deeper than 1m in the sediment.

ACKNOWLEDGMENT

The authors would like to thank A. Orlov, V. Korolkov, S. Zacharov, and M. Klucar. Special thanks to P. Ripka for advice with the measurement procedure and securing the geodetic grade GPS receivers, B. Koska for help during the GPS system testing and data processing, V. Vigner for providing spare GPS time synchronization modules, and M. Janosek who helped with magnetometer calibration and magnetic data interpretation.

REFERENCES

- [1] J. Borovicka, P. Spurny, and L. Shrbeny, "Trajectory and orbit of the Chelyabinsk superbolide," Int. Astronomical Union, Cambridge, MA, USA, Electron. Telegram No. 3423, 2013.

- [2] J. Borovička *et al.*, "The trajectory, structure and origin of the Chelyabinsk asteroidal impactor," *Nature*, vol. 503, pp. 235–237, Nov. 2013.
- [3] E. M. Galimov *et al.*, "Analytical results for the material of the Chelyabinsk meteorite," *Geochem. Int.*, vol. 51, no. 7, pp. 522–539, 2013.
- [4] N. S. Bezaeva, D. D. Badyukov, M. A. Nazarov, P. Rochette, and J. Feinberg, "Magnetic properties of the Chelyabinsk meteorite: Preliminary results," *Geochem. Int.*, vol. 51, no. 7, pp. 568–574, 2013.
- [5] C. Cournède, J. Gattacceca, and P. Rochette, "Magnetic study of large apollo samples: Possible evidence for an ancient centered dipolar field on the moon," *Earth Planetary Sci. Lett.*, vols. 331–332, pp. 31–42, May 2012.
- [6] J. Gattacceca *et al.*, "Can the lunar crust be magnetized by shock: Experimental groundtruth," *Earth Planetary Sci. Lett.*, vol. 299, nos. 1–2, pp. 42–53, 2010.
- [7] L. Folco, P. Rochette, J. Gattacceca, and N. Perchiazzi, "In situ identification, pairing, and classification of meteorites from Antarctica through magnetic susceptibility measurements," *Meteoritics Planetary Sci.*, vol. 41, no. 3, pp. 343–353, 2006.
- [8] G. Marin, S. Radu, G. Samoilescu, and O. Baltag, "The analysis of gradiometer signal in magnetic field measurement with fluxgate transducer," in *Proc. 10th Int. Conf. Commun. (COMM)*, May 2014, pp. 1–6.
- [9] R. Wiegert, K. Lee, and J. Oeschger, "Improved magnetic STAR methods for real-time, point-by-point localization of unexploded ordnance and buried mines," in *Proc. OCEANS*, Sep. 2008, pp. 1–7.
- [10] M. Tchernychev, J. Johnston, and R. Johnson, "Total magnetic field transverse gradiometer as UXO locating tool: Case study," in *Proc. EGM Int. Workshop*, Capri, Italy, 2010, pp. 1–3.
- [11] Y. H. Pei and H. G. Yeo, "UXO survey using vector magnetic gradiometer on autonomous underwater vehicle," in *Proc. MTS/IEEE Biloxi-Marine Technol. Our Future, Global Local Challenges OCEANS*, Oct. 2009, pp. 1–8.
- [12] E. Mersch, Y. Yvinec, Y. Dupont, X. Neyt, and P. Druyts, "Underwater magnetic target localization and characterization using a three-axis gradiometer," in *Proc. OCEANS-TAIPEI*, Apr. 2014, pp. 1–6.
- [13] G. L. Allen, G. Sulzberger, J. T. Bono, J. S. Pray, and T. R. Clem, "Initial evaluation of the new real-time tracking gradiometer designed for small unmanned underwater vehicles," in *Proc. MTS/IEEE OCEANS*, 2005, vol. 3, pp. 1956–1962.
- [14] M. Janosek, A. Platil, J. Vyhnanek, and J. Brinek, "Dual-core fluxgate gradiometer with gradient feedback," in *Proc. IEEE SENSORS*, Nov. 2013, pp. 1–3.
- [15] Natural Resources Canada. *Precise Point Positioning*. [Online]. Available: <http://webapp.geod.nrcan.gc.ca/geod/tools-outils/ppp.php?locale=en>, accessed Jun. 12, 2013.
- [16] J. M. G. Merayo, P. Brauer, F. Primdahl, J. R. Petersen, and O. V. Nielsen, "Scalar calibration of vector magnetometers," *Meas. Sci. Technol.*, vol. 11, no. 2, pp. 120–132, 2000.
- [17] V. Petrucha, P. Ripka, P. Kaspar, and J. M. G. Merayo, "Automated system for the calibration of magnetometers," *J. Appl. Phys.*, vol. 105, no. 7, p. 07E704, 2009.
- [18] V. Petrucha, M. Janosek, and M. A. Azpurua, "Vector feedback homogeneity and inner layout influence on fluxgate sensor parameters," *IEEE Trans. Instrum. Meas.*, vol. 64, no. 5, pp. 1293–1299, May 2014.
- [19] D. Kerridge, "INTERMAGNET: Worldwide near-real-time geomagnetic observatory data," in *Proc. Workshop Space Weather*, 2001, pp. 1–4. [Online]. Available: http://www.intermagnet.org/publications/IM_ESTEC.pdf
- [20] N. S. Bezaeva *et al.*, "Magnetic properties of the LL5 ordinary chondrite Chelyabinsk (fall of February 15, 2013)," *Meteoritics Planetary Sci.*, vol. 49, no. 6, pp. 958–977, 2014.
- [21] A. V. Kocherov, A. V. Korochantsev, C. A. Lorenz, M. A. Ivanova, and V. I. Grokhovskiy, "Recovery, laboratory preparation and current state of the main mass of the Chelyabinsk meteorite," in *Proc. 45th Lunar Planetary Sci. Conf.*, 2014, p. 2227.
- [22] V. V. Kopeikin, V. D. Kuznetsov, P. A. Morozov, A. V. Popov, A. I. Berkut, and S. V. Merkulov, "GPR inspection of the Chelyabinsk meteorite impact site at the Chebarkul Lake bottom," in *Proc. 15th Int. Conf. Ground Penetrating Radar (GPR)*, Jun./Jul. 2014, pp. 1024–1027.
- [23] O. P. Popova *et al.*, "Chelyabinsk airburst, damage assessment, meteorite recovery, and characterization," *Science*, vol. 342, no. 6162, pp. 1069–1073, Nov. 2013.



Gunther Kletetschka was born in Litomerice, Czech Republic, in 1964. He received the B.S. degree in physics/geophysics in 1989, the RNDr (Equivalent of M.S.) degree in physics/geophysics from the Charles University in Prague, Czech Republic, in 1989, and the M.S. and Ph.D. degrees in geology/geophysics from the University of Minnesota, Minneapolis, MN, USA, in 1994 and 1998, respectively.

He joined the Department of Geophysics and Meteorology, Faculty of Science, Charles University, in 1989, as a Teaching Assistant/Lecturer. Since 1991, he has been a member of the Department of Geology and Geophysics, University of Minnesota, where he was a Teaching Assistant/Lecturer. Since 1998, he has been with NASA GSFC, Greenbelt, MD, USA, first as a Post-Doctoral Researcher with the National Research Council and then as a Contractor via Research Professor at Howard University, Catholic University of America, Delaware University. In 2004, he joined the Institute of Geology, and Academy of Sciences of the Czech Republic as a Research Scientist. In 2011, he joined the Faculty of Science, Charles University in Prague, Czech Republic. Since 2010, he has been a Guest Researcher at NIST, Gaithersburg, MD, USA, and the Lawrence Berkeley National Laboratory in Berkeley, CA, USA, since 2013.

His current research interests include planetary geophysics, magnetic mineralogy, climate change, and planetary instruments. He leads the group of extraterrestrial geology and geophysics and is serving on NASA panels for proposal reviews.



Jan Vyhnanek was born in Prague, Czech Republic, in 1987. He received the M.Sc. degree in measurements and instrumentation from the Faculty of Electrical Engineering, Czech Technical University in Prague, Prague, in 2011, where he is currently pursuing the Ph.D. degree at the Department of Measurement. He is mainly interested in magnetic sensors and their applications in object detection.



Darja Kawasumiova was born in Czech Republic in 1955. She received the bachelor's degree in liberal arts, intercultural/interhuman relationships from the International Christian University, Tokyo, in 1982.

She returned in 1992 from Japan back to Czech Republic and graduated from Charles University, Prague, Czech Republic, receiving Bachelor of Liberal Arts in 1994, Japanese Studies, and Mast of Liberal Arts in 1999. She then studied at the Wesley Theological Seminary, Washington DC, USA, and received the Master of Theology Studies in 2010. The art of hospitality as a tool to enhance understanding between nations, cultures, religions, religion, and science is her life academic theme. In her Master thesis, at Charles University, she searched for bonds between the Western Christian thought and the Eastern philosophy, as represented in the art of communication and hospitality, the core of the Japanese Tea Ceremony. In her Master thesis, at Wesley, she used the Tea Ceremony theme to support her theology, in which a great role is given to human hospitable creativity. She returned to Czech Republic in 2011, and searched for connections between science and art. She currently runs CaJ Ltd. (CaJ stands for Czech and Japan)



Ladislav Nabelek was born in Prague, Czech Republic, in 1991. He graduated with a Degree in electrical engineering from High School Technical F. Krizika, Prague, in 2011, and received the B.S. degree in geology from the Faculty of Science, Charles University in Prague, in 2014, where he is currently pursuing the Degree in applied geophysics.

He joined the Institute of Geology, Academy of Sciences of the Czech Republic, in 2011, as an Assistant and Laboratory Technician of Science and Research. In 2012, he joined the Extraterrestrial Geology and Geophysics Group, Faculty of Science, Charles University in Prague, Czech Republic. His current research interests include planetary geophysics, magnetic mineralogy, climate change, and planetary instruments.



Vojtech Petrucha was born in Prerov, Czech Republic, in 1982. He received the M.Sc. degree in measurement and instrumentation and the Ph.D. degree in measurement and instrumentation for work on the calibration of magnetometers from the Faculty of Electrical Engineering, Czech Technical University in Prague, Czech Republic, in 2007 and 2012, respectively.

He is currently a Research Assistant with the Department of Measurement, Faculty of Electrical Engineering, Czech Technical University in Prague. His research interests include the development, construction, and calibration of sensor systems, especially magnetic field sensors.

4 Conclusions

Current magnetic field measurement methods for object detection show several possibilities for further development, some have been addressed by the recent research.

The objectives from the chapter 2 were fulfilled:

- I. The detector with AMR sensors was designed and its performance verified in applications for detection of mines (3.2.2) and for visualization of metal structures in buildings (3.2.3).
- II. The solution, how to compensate for strong excitation and biasing field, is:
 - II.a field compensation by a feedback compensation coil, which was successfully used in the innovative AMR gradiometer design (3.2.1).
 - II.b. Perpendicular orientation of a sensor to the excitation field was used in the low-frequency linear position sensor (3.2.5). Effects of the crossfield error and comparison of an AMR and integrated fluxgate sensor were examined and result published in the respective paper (chapter 3.1.3). The integrated fluxgate sensor provided a distinct advantage over the AMR in terms of the crossfield.
- III. Applications, where DC magnetic field sensors provide an advantage over induction sensors at low-frequencies, are those which have to minimize eddy currents (3.2.4). Detection of metal objects behind a conductive wall requires the low frequency to penetrate the wall. The frequency limit, where a DC sensor has better noise than a similarly sized induction sensor, was studied (3.1.1). This limit is between 10 Hz and 100 Hz, depending on the sensor type.

AC metal detectors with excitation field are usually using induction coils, however there are applications where the low excitation frequencies are necessary and where the induction coil is limited by low sensitivity at low frequencies. NDT and position sensors with magnetoresistors and integrated fluxgates proved useful in applications where the excitation field should have low frequency in order to penetrate a thick conductive material to detect a deep defect or sense a position of metallic object covered by a conducting shield.

4.1 Future work

The author would suggest to continue research in this area by developing more thorough theoretical description of the noise and sensitivity limits of various competing technologies used for metal detection and buried object visualization. (Especially in the area of classical large induction coil for mine detectors and their respective advantages and disadvantages compared to AMR and/or fluxgate sensor arrays.) Such a theoretical background should provide guidelines for evaluation of design limits and possible advantages in comparison to existing commercial devices for visualization of metal structures in buildings.

5 List of own publications

5.1 Publications related to the thesis

5.1.1 Publications in journals with impact factor

- [J1] Vyhnánek, J.; Ripka, P. *Experimental Comparison of the Low-Frequency Noise of Small-Size Magnetic Sensors*, IEEE Transactions on Magnetics. 2017, 53(4), ISSN 0018-9464. *co-authorship 50 %*
- [J2] Ripka, P.; Vyhnánek, J.; Chirtsov, A. *Crossfield response of industrial magnetic sensors*, International Journal of Applied Electromagnetics and Mechanics. 2017, 55(S1), 39-47. ISSN 1383-5416. *co-authorship 30 %*
- [J3] Vyhnánek, J.; Janošek, M.; Ripka, P. *AMR Gradiometer for Mine Detection*, Sensors and Actuators. 2012, 186 100-104. ISSN 0924-4247. *co-authorship 75 %*
- [J4] Ripka, P.; Vyhnánek, J.; Janošek, M.; Včelák, J. *AMR Proximity Sensor With Inherent Demodulation*, IEEE Sensors Journal. 2014, 14(9), 3119-3123. ISSN 1530-437X. *co-authorship 25 %*
- [J5] Kletetschka, G.; Vyhnánek, J.; Kawasumiova, D.; Nabelek, L.; Petrucha, V. *Localization of the Chelyabinsk Meteorite from Magnetic Field Survey and GPS Data*, IEEE Sensors Journal. 2015, 2015(15), 4875-4881. ISSN 1530-437X. *co-authorship 20 %*
- [J6] Janošek, M.; Platil, A.; Vyhnánek, J. *The Effect of Sensor Size on Axial Gradiometer Performance*, IEEE Transactions on Magnetics. 2015, 51(1), ISSN 0018-9464. *co-authorship 20 %*

5.1.2 Conference proceedings in WoS

- [C1] Vyhnánek, J.; Janošek, M.; Ripka, P. *Low frequency noise of anisotropic magnetoresistors in DC and AC-excited metal detectors*, In: Sensors & Their Applications XVII. Bristol: IOP Publishing Ltd, 2013, pp. 1-5. Journal of Physics Conference Series. ISSN 1742-6588. *co-authorship 50 %*
- [C2] Janošek, M.; Vyhnánek, J.; Ripka, P. *CW Metal Detector Based on AMR Sensor Array*, In: IEEE Sensors 2011 - Proceedings. Limerick: IEEE Sensors Council, 2011, pp. 1515-1517. ISSN 1930-0395. ISBN 978-1-4244-9288-6. *co-authorship 35 %*
- [C3] Janošek, M.; Vyhnánek, J.; Platil, A. *Compact magnetic gradiometer and its astatization*, In: Procedia Engineering Special Issue Eurosensors 2015. Oxford: Elsevier Ltd, 2015. pp. 1249-1252. ISSN 1877-7058. *co-authorship 10 %*
- [C4] Janošek, M.; Platil, A.; Vyhnánek, J. *Simple estimation of dipole source z-distance with compact magnetic gradiometer*, In: Proceedings of 5th International Conference on Materials and Applications for Sensors and Transducers (IC-MAST2015). Bristol. IOP

Conference Series: Materials Science and Engineering. ISSN 1757-899X. co-authorship 33 %

- [C5] Janošek, M.; Vyhnánek, J.; Zikmund, A.; Butvin, P.; Butvinová, B. *Effects of Core Dimensions and Manufacturing Procedure on Fluxgate Noise*, Acta Physica Polonica A. 2014, 126(1), 104-105. ISSN 0587-4246. co-authorship 10 %

5.1.3 Conference proceedings – others

- [O1] Vyhnánek, J.; Král, J. *Linear Scanner with Magnetic Field Mapping*, In: POSTER 2013 - 17th International Student Conference on Electrical Engineering. Prague: Czech Technical University, 2013, ISBN 978-80-01-05242-6. co-authorship 60 %
- [O2] Vyhnánek, J.; Ripka, P.; Chirtsov, A. *Linear Position Sensing through Conductive Wall without Permanent Magnet*, In: Proceedings of Eurosensors 2017. Basel: MDPI AG, 2017. vol. 1. ISSN 2504-3900. co-authorship 40 %

5.1.4 Patent

- [P1] Ripka, P.; Vyhnánek, J.; Včelák, J. *Bezkontaktní magnetický senzor polohy magnetických nebo elektricky vodivých objektů (EN: Contactless magnetic position sensor of magnetic or electrically conducting objects)*, Czech Republic. Patent. CZ 304954. 2014-12-29. co-authorship 33 %

5.2 Publications *not* related to the thesis

5.2.1 Publications in journals with impact factor

- [J7] Mirzaei, M.; Ripka, P.; Chirtsov, A.; Kašpar, P.; Vyhnánek, J. *The effect of conductor permeability on electric current transducers*, AIP Advances. 2018, 8 ISSN 2158-3226. *co-authorship 10 %*
- [J8] Ripka, P.; Chirtsov, A.; Mirzaei, M.; Vyhnánek, J. *Inductance position sensor for pneumatic cylinder*, AIP Advances. 2018, 8(4), ISSN 2158-3226. *co-authorship 25 %*
- [J9] Janošek, M.; Vyhnánek, J.; Platil, A.; Petrucha, V. *Compact Full-tensor Fluxgate Gradiometer*, Journal of Electrical Engineering. 2015, 66(7/s), 146-148. ISSN 1335-3632. *co-authorship 10 %*

5.3 Response to author's publications

- [C1] Vyhnánek, J.; Janošek, M.; Ripka, P. *Low frequency noise of anisotropic magnetoresistors in DC and AC-excited metal detector*, In: Sensors & Their Applications XVII. Bristol: IOP Publishing Ltd, 2013, pp. 1-5. Journal of Physics Conference Series. ISSN 1742-6588:
- Diaz-Michelena, Marina; Cobos, Pedro; Aroca, Claudio *Lock-in amplifiers for AMR sensors*, SENSORS AND ACTUATORS A-PHYSICAL, vol. 222, pp. 149 - 159, 2015. ISSN 0924-4247.
- [J3] Vyhnánek, J.; Janošek, M.; Ripka, P. *AMR Gradiometer for Mine Detection*, Sensors and Actuators. 2012, 186 100-104. ISSN 0924-4247.
- Gurkan, S.; Karapinar, M.; Dogan, S. *Classification of Explosives Materials Detected by Magnetic Anomaly Method*, 2017 4TH INTERNATIONAL CONFERENCE ON ELECTRICAL AND ELECTRONIC ENGINEERING (ICEEE 2017), pp. 347 - 350, 2017.
 - Guo, Y.; Ouyang, Y.; Sato, N.; Ooi, C.; Wang, Shan X. *Exchange-Biased Anisotropic Magnetoresistive Field Sensor*, IEEE SENSORS JOURNAL, vol. 17, no. 11, pp. 3309 - 3315, 2017. ISSN 1530-437X.
 - Ege, Yavuz; Coramik, Mustafa; Kabadayi, Murat; Citak, Hakan; Kalender, Osman; Yuruklu, Emrah; Kurt, Unal; Nazlibilek, Sedat *Anomaly detection with low magnetic flux: A fluxgate sensor network application*, MEASUREMENT, vol. 81, pp. 43 - 56, 2016. ISSN 0263-2241.
 - Ege, Yavuz; Nazlibilek, Sedat; Kakilli, Adnan; Citak, Hakan; Kalender, Osman; Erturk, Korhan Lev; Sengul, Gokhan; Karacor, Deniz *A Magnetic Measurement System and Identification Method for Buried Magnetic Materials Within Wet and Dry Soils*, IEEE TRANSACTIONS ON GEOSCIENCE AND REMOTE SENSING, vol. 54, no. 3, pp. 1803 - 1811, 2016. ISSN 0196-2892.
 - Ege, Yavuz; Kakilli, Adnan; Citak, Hakan; Kalender, Osman; Nazlibilek, Sedat; Sensoy, Mehmet Gok *New magnetic measurement system for determining metal covered mines by detecting magnetic anomaly using a sensor network*, INDIAN JOURNAL OF PURE & APPLIED PHYSICS, vol. 53, no. 3, pp. 199 - 211, 2015. ISSN 0019-5596.
 - Ege, Y; Kakilli, A *Performance Analysis of Techniques Used for Determining Land Mines*, International Journal of Geosciences, 2014. ISSN 2156-8359.
 - Long, L., Zhong, S., Wu, Y. *Design and fabrication of MEMS magnetic sensor based on capacitance detection*, Nami Jishu yu Jingmi Gongcheng / Nanotechnology and Precision Engineering, vol. 11, no. 3, pp. 222 - 230, 2013. ISSN 1672-6030.
 - Long, L., Zhong, S.-L., Xu, J., Wu, Y.-M. *Design and fabrication of micro fiber-optic magnetic sensor*, Guangxue Jingmi Gongcheng / Optics and Precision Engineering, vol. 21, no. 9, pp. 2294 - 2302, 2013. ISSN 1004-924X.
 - Leito D. C., Borme J., Orozco A., Cardoso S., Freitas P. P. *Magnetoresistive Sensors for Surface Scanning*, Giant Magnetoresistance (GMR) Sensors, vol. 6, pp. 275 - 299, 2013. ISBN 978-3-642-37171-4. ISSN 2194-8402.
 - Shen, Ying; Gao, Junqi; Wang, Yaojin; Hasanyan, Davresh; Finkel, Peter; Li, Jiefang; Viehland, D. *Flux distraction effect on magnetoelectric laminate sensors and*

gradiometer, JOURNAL OF APPLIED PHYSICS, vol. 114, no. 13, 2013. ISSN 0021-8979.

- [C2] Janošek, M.; Vyhnánek, J.; Ripka, P. *CW Metal Detector Based on AMR Sensor Array*, In: IEEE Sensors 2011 - Proceedings. Limerick: IEEE Sensors Council, 2011, pp. 1515-1517. ISSN 1930-0395. ISBN 978-1-4244-9288-6.
- Hadjigeorgiou, N.; Hristoforou, E.; Sotiriadis, P. P. *Closed-Loop Current-Feedback, Signal-Chopped, Low Noise AMR Sensor With High Linearity*, 2017 6TH INTERNATIONAL CONFERENCE ON MODERN CIRCUITS AND SYSTEMS TECHNOLOGIES (MOCASST), 2017.
 - J. Borme, A. Orozco, S. Cardoso, P. P. Freitas, *Magnetoresistive Sensors for Surface Scanning*, Giant Magnetoresistance (GMR) Sensors, pp. 275 - 299, 2013. ISBN 978-3-642-37171-4.
- [J5] Kletetschka, G.; Vyhnánek, J.; Kawasumiova, D.; Nabelek, L.; Petrucha, V. *Localization of the Chelyabinsk Meteorite from Magnetic Field Survey and GPS Data*, IEEE Sensors Journal. 2015, 2015(15), 4875-4881. ISSN 1530-437X.
- Ge, J.; Qiu, X.; Dong, H.; Luo, W.; Liu, H.; Yuan, Z.; Zhu, J.; Zhang, H. *Short-Time and High-Precision Measurement Method for Larmor Frequency of Marine Overhauser Sensor*, IEEE SENSORS JOURNAL, vol. 18, no. 4, pp. 1442 - 1448, 2018. ISSN 1530-437X.
 - Hsu, L.; Tokura, H.; Kubo, N.; Gu, Y.; Kamijo, S. *Multiple Faulty GNSS Measurement Exclusion Based on Consistency Check in Urban Canyons*, IEEE SENSORS JOURNAL, vol. 17, no. 6, pp. 1909 - 1917, 2017. ISSN 1530-437X.
 - Narkhov, Eugene D.; Sergeev, Andrey V.; Milyukov, Dmitriy N.; Fedorov, Andrey L.; Sapunov, Vladimir A. *Magnetometric Survey of LL5 Chelyabinsk Meteorite in Lake Chebarkul*, PHYSICS, TECHNOLOGIES AND INNOVATION (PTI-2016), vol. 1767, 2016. ISSN 0094-243X.
- [C4] Janošek, M.; Platil, A.; Vyhnánek, J. *Simple estimation of dipole source z-distance with compact magnetic gradiometer*, In: Proceedings of 5th International Conference on Materials and Applications for Sensors and Transducers (IC-MAST2015). Bristol. IOP Conference Series: Materials Science and Engineering. ISSN 1757-899X.
- Jarvis, R.; Cawley, P.; Nagy, Peter B. *Performance evaluation of a magnetic field measurement NDE technique using a model assisted Probability of Detection framework*, NDT & E INTERNATIONAL, vol. 91, pp. 61 - 70, 2017. ISSN 0963-8695.
- [J6] Janošek, M.; Platil, A.; Vyhnánek, J. *The Effect of Sensor Size on Axial Gradiometer Performance*, IEEE Transactions on Magnetics. 2015, 51(1), ISSN 0018-9464.
- Yaglidere, I.; Gunes, E. *A Novel Method for Calculating the Ring-Core Fluxgate Demagnetization Factor*, IEEE TRANSACTIONS ON MAGNETICS, vol. 54, no. 2, 2018. ISSN 0018-9464.

- [C5] Janošek, M.; Vyhnánek, J.; Zikmund, A.; Butvin, P.; Butvinová, B. *Effects of Core Dimensions and Manufacturing Procedure on Fluxgate Noise*, Acta Physica Polonica A. 2014, 126(1), 104-105. ISSN 0587-4246.
- Butta, M. *Effect of Thickness of Electroplated NiFe Cores on the Noise of Fluxgates*, ACTA PHYSICA POLONICA A, vol. 131, no. 4, pp. 756 - 758, 2017. ISSN 0587-4246.
- [O2] Vyhnánek, J.; Ripka, P.; Chirtsov, A. *Linear Position Sensing through Conductive Wall without Permanent Magnet*, In: Proceedings of Eurosensors 2017. Basel: MDPI AG, 2017. vol. 1. ISSN 2504-3900.
- Krause, J.; Bhounsule, P. *A 3D Printed Linear Pneumatic Actuator for Position, Force and Impedance Control*. Actuators 2018, 7, 24.

References:

- Ando, B., Baglio, S., Sacco, V., Bulsara, A. R., & In, V. (2008). Pcb fluxgate magnetometers with a residence times difference readout strategy: The effects of noise. *Instrumentation and Measurement, IEEE Transactions on*, 57(1), pp.19-24.
- Bartington, G., & Chapman, C. E. (2004). A high-stability fluxgate magnetic gradiometer for shallow geophysical survey applications. *Archaeological Prospection*, 11(1), pp.19-34.
- Benitez, D. S., Quek, S., Gaydecki, P., & Torres, V. (2008). A preliminary magnetoinductive sensor system for real-time imaging of steel reinforcing bars embedded within concrete. *Instrumentation and Measurement, IEEE Transactions on*, 57(11), pp.2437-2442.
- Benitez, D. S., Quek, S., Gaydecki, P., & Torres, V. (2009). A 1-D solid-state-sensor-based array system for magnetic field imaging of steel reinforcing bars embedded within reinforced concrete. *Instrumentation and Measurement, IEEE Transactions on*, 58(9), pp.3335-3340.
- Bracken, R. E., & Brown, P. J. (2006). *Concepts and procedures required for successful reduction of tensor magnetic gradiometer data obtained from an unexploded ordnance detection demonstration at Yuma Proving Grounds, Arizona*. US Geological Survey.
- Breiner, S., 1999. *Applications manual for portable magnetometers*. California: Geometrics.
- Brown, P., Beek, T., Carr, C., O'Brien, H., Cupido, E., Oddy, T., & Horbury, T. S. (2012). Magnetoresistive magnetometer for space science applications. *Measurement Science and Technology*, 23(2), 025902.
- Bruschini, C. (2000a). Metal detectors in civil engineering and humanitarian demining: Overview and tests of a commercial visualizing system. *Insight: Non-Destructive Testing and Condition Monitoring*, 42(2), pp.89-97.
- Bruschini, C., & Sahli, H. (2000b). Phase angle based EMI object discrimination and analysis of data from a commercial differential two frequency system. *SPIE AeroSense 2000, Detection and Remediation Technologies for Mines and Mine-Like Targets*, pp.24-28.
- Bruschini, C., Marinella, A., & Sorpresa, M. (2002). A multidisciplinary analysis of frequency domain metal detectors for humanitarian demining. *Ph. D. thesis, Faculty of Applied Sciences, Vrije Universiteit*.
- Chekcheyev, S. (2009). A temperature-stable metal detector. *IEEE Transactions on Instrumentation and Measurement*, 58(6), 1907-1910.
- Daughton, J. M. (2000). GMR and SDT sensor applications. *Magnetics, IEEE Transactions on*, 36(5), pp.2773-2778.
- Di Iorio, F. (2007). *Low field magnetic sensing with giant magneto resistive sensors*. Doctoral dissertation, Università degli Studi di Napoli Federico II.
- Dogaru, T., & Smith, S. T. (2001). Giant magnetoresistance-based eddy-current sensor. *Magnetics, IEEE Transactions on*, 37(5), 3831-3838.

Dogaru, T., Smith, C. H., Schneider, R. W., & Smith, S. T. (2004). Deep crack detection around fastener holes in airplane multi-layered structures using GMR-based eddy current probes. *AIP Conference Proceedings*, Vol. 700, pp. 398.

Fukushima, E. F., & Hirose, S. (2009). Humanitarian Demining Operation Using the Teleoperated Buggy Vehicle Gryphon with a Mine Sensors Equipped Arm. In *Anti-personnel Landmine Detection for Humanitarian Demining*, Springer London, pp. 103-121.

Gasperikova, E. (2010). *Hand-Held UXO Discriminator* (No. SERDP-PROJECT-MR-1667). California University, Lawrence Berkeley lab.

Gaydecki, P., Fernandes, B., Quek, S., Benitez, D., Miller, G., & Zaid, M. (2007). Inductive and magnetic field inspection systems for rebar visualization and corrosion estimation in reinforced and pre-stressed concrete. *Nondestructive Testing and Evaluation*, 22(4), pp.255-298.

Gilles, A., Didier, R., & Stephane, F. (2012). Differential Search Coils Based Magnetometers: Conditioning, Magnetic Sensitivity, Spatial Resolution. *Sensors & Transducers*, 14.

Grosz, A., & Paperno, E. (2012). Analytical Optimization of Low-Frequency Search Coil Magnetometers. *Sensors Journal, IEEE*, 12(8), pp.2719-2723.

Grüger, H. (2003). Array of miniaturized fluxgate sensors for non-destructive testing applications. *Sensors and Actuators A: Physical*, 106(1), 326-328.

Guelle, D., Smith, A., Lewis, A., Bloodworth, T. (2003) *Metal Detector Handbook for Humanitarian Demining: A Book about Metal Detectors, Covering Detection Procedures in the Field, and the Testing and Evaluation of Metal Detectors for Humanitarian Demining*. Office for Official Publications of the European Communities.

Hadjigeorgiou, N., Hristoforou, E., & Sotiriadis, P. P. (2017). *Closed-loop current-feedback, signal-chopped, low noise AMR sensor with high linearity*. In Modern Circuits and Systems Technologies (MOCAST), 2017 6th International Conference on (pp. 1-4). IEEE.

Halloran, S., Pappas, D., da Silva, F., & Kos, A. (2007). *Defense & Security Multichannel real-time magnetic imaging system*. [online] SPIE Newsroom. Available at: <<http://spie.org>> [Accessed 22. August 2013].

Hauser, H., Fulmek, P. L., Haumer, P., Vopalensky, M., & Ripka, P. (2003). Flipping field and stability in anisotropic magnetoresistive sensors. *Sensors and Actuators A: Physical*, 106(1), pp.121-125.

He, D. F., Shiwa, M., Jia, J. P., Takatsubo, J., & Moriya, S. (2011). Multi-frequency ECT with AMR sensor. *NDT & E International*, 44(5), pp.438-441.

He, D. F., Tachiki, M., & Itozaki, H. (2009). Highly sensitive anisotropic magnetoresistance magnetometer for Eddy-current nondestructive evaluation. *Review of Scientific Instruments*, 80(3), 036102-036102.

Hesse, O., & Pankratyev, S. (2005). Usage of magnetic field sensors for low frequency eddy current testing. *Measurement science review*, 5.

Hilti Corporation. (2006). *PS200 Ferroskan operation manual*. Schaan, Lichtenstein: Hilti Co.

Hochreiter, J., & Schrottmayer, D. (2000). *DIMADS — Digital Magnetic Anomaly Detection System*. Vienna: Schiebel Elektronische Geräte GmbH.

Honeywell. (2008). *1- and 2-Axis Magnetic Sensors HMC1001/1002/1021/1022*. Plymouth, USA. Honeywell.

Cherepov, S., Hesse, O., Mook, G., Pankratyev, S., & Uchanin, V. (2004). Optimisation of Low Frequency Eddy Current Sensors Using Improved Inductive Coils and Highly Sensitive AMR and GMR Sensor Modules. *Proceeding of the 13th IMEKO TC-4 International Symposium*, Vol. 2, pp.568-576.

Christides, C., Panagiotopoulos, I., Niarchos, D., & Jones, G. (2003). Fast magnetic field mapping of permanent magnets with GMR bridge and Hall-probe sensors. *Sensors and Actuators A: Physical*, 106(1), pp.243-245.

Jagiella, M., Fericean, S., & Dorneich, A. (2006). Progress and recent realizations of miniaturized inductive proximity sensors for automation. *Sensors Journal, IEEE*, 6(6), pp.1734-1741.

Jander, A., Smith, C., & Schneider, R. (2005). Magneto-resistive sensors for nondestructive evaluation. In *Nondestructive Evaluation for Health Monitoring and Diagnostics* (pp. 1-13). International Society for Optics and Photonics.

Kang, M. H., Choi, B. W., Koh, K. C., Lee, J. H., & Park, G. T. (2005). Experimental study of a vehicle detector with an AMR sensor. *Sensors and Actuators A: Physical*, 118(2), pp.278-284.

Kletetschka, G., Schnabl, P., Šifnerová, K., Tasáryová, Z., Manda, Š., & Pruner, P. (2013). Magnetic scanning and interpretation of paleomagnetic data from Prague Synform's volcanics. *Studia Geophysica et Geodaetica*, 57(1), pp.103-117.

Kousek, H., et.al, Hilti Co. (1994). Apparatus for determining location of an element of magnetizable material in a construction structure. U.S. Pat. 5,296,807.

Kruger, H., & Ewald, H. (2008). Handheld metal detector with online visualisation and classification for the humanitarian mine clearance. *Sensors, 2008 IEEE*, pp.415-418.

Kubik, J., Pavel, L., & Ripka, P. (2006). PCB racetrack fluxgate sensor with improved temperature stability. *Sensors and Actuators A: Physical*, 130, 184-188.

Lee, R. D. (1972). *U.S. Patent No. 3,676,772*. Washington, DC: U.S. Patent and Trademark Office.

Lewis, A. M.(2004). Multisensor Mine Signatures. *Final Report of ITEP Project*, 2(1.2).

- Linzen, S., Chwala, A., Schultze, V., Schulz, M., Schuler, T., Stolz, R., & Meyer, H. G. (2007). A LTS-SQUID system for archaeological prospection and its practical test in Peru. *Applied Superconductivity, IEEE Transactions on*, 17(2), pp.750-755.
- MacDonald, J. A., & Lockwood, J. R. (2003). *Alternatives for landmine detection* (No. 1608). RAND corporation.
- Merayo, J. M., Brauer, P., & Primdahl, F. (2005). Triaxial fluxgate gradiometer of high stability and linearity. *Sensors and Actuators A: Physical*, 120(1), 71-77.
- Mesina, M. B., De Jong, T. P. R., & Dalmijn, W. L. (2003). Improvements in separation of non-ferrous scrap metals using an electromagnetic sensor. *Physical Separation in Science and Engineering*, 12(2), 87-101.
- MIT Mess- und Prüftechnik GmbH. (2008). *MIT-SCAN2-BT measuring system*. Dresden, Germany: MIT GmbH.
- Munsch, M., Boulanger, D., Ulrich, P., & Bouiflane, M. (2007). Magnetic mapping for the detection and characterization of UXO: Use of multi-sensor fluxgate 3-axis magnetometers and methods of interpretation. *Journal of applied geophysics*, 61(3), pp.168-183.
- Nelson, H. H., & McDonald, J. R. (2001). Multisensor towed array detection system for UXO detection. *Geoscience and Remote Sensing, IEEE Transactions on*, 39(6), pp.1139-1145.
- NVE Corporation. (2005). *Application Notes for GMR Sensors*. Minneapolis, MN: NVE Co.
- Pasadas, D., Ramos, H. G., & Alegria, F. (2011). Handheld instrument to detect defects in conductive plates with a planar probe. *Instrumentation and Measurement Technology Conference (I2MTC), 2011 IEEE*, pp.1-6.
- Platil, A., Kubik, J., Vopalensky, M., & Ripka, P. (2003). Precise AMR magnetometer for compass. In *Sensors, 2003. Proceedings of IEEE*, Vol. 1, pp.472-476.
- Popovic, R. S., Drljaca, P. M., & Schott, C. (2002). Bridging the gap between AMR, GMR, and Hall magnetic sensors. In *Microelectronics, 2002. MIEL 2002. 23rd International Conference on*, Vol. 1, pp.55-58.
- Prance, R. J., Clark, T. D., & Prance, H. (1999). Compact broadband gradiometric induction magnetometer system. *Sensors and Actuators A: Physical*, 76(1), pp.117-121.
- Prance, R. J., Clark, T. D., & Prance, H. (2000). Ultra low noise induction magnetometer for variable temperature operation. *Sensors and Actuators A: Physical*, 85(1), pp.361-364.
- Reininger, T., Welker, F., & Von Zeppelin, M. (2006). Sensors in position control applications for industrial automation. *Sensors and Actuators A: Physical*, 129(1), pp.270-274.
- Ripka, P. (2001). *Magnetic Sensors and Magnetometers*. Norwood, MA: Artech House.

- Ripka, P., Nováček, P., Reinštein, M., & Roháč, J. (2010). Position sensing system for eddy-current mine imager. *Procedia Engineering*, 5, pp.276-279.
- Ripka, P., Primdahl, F., Nielsen, O. V., Petersen, J. R., & Ranta, A. (1995). Ac magnetic-field measurement using the fluxgate. *Sensors and Actuators A: Physical*, 46(1), pp.307-311.
- Ripka, P., Tondra, M., Stokes, J., & Beech, R. (1999). AC-driven AMR and GMR magnetoresistors. *Sensors and Actuators A: Physical*, 76(1), 225-230.
- Ripka, P., Vopálenský, M., Platil, A., Döscher, M., Lenssen, K. M., & Hauser, H. (2003). AMR magnetometer. *Journal of magnetism and magnetic materials*, 254, pp.639-641.
- Roux, A., Le Contel, O., Coillot, C., Bouabdellah, A., De La Porte, B., Alison, D., & Vassal, M. C. (2009). The search coil magnetometer for THEMIS. *The THEMIS Mission*, Springer New York, pp.265-275.
- Rühmer, D., Shanmuganathan, P., Ludwig, F., & Schilling, M. (2012). Spatial and field resolution of wire-wound fluxgates in magnetic dipole fields. *Sensors and Actuators A: Physical*, 173(1), pp.30-35.
- Siegel, R., & Selfridge, R. (2008). *Man-portable simultaneous magnetometer and EM system (MSEMS)*. SCIENCE APPLICATIONS INTERNATIONAL CORPORATION NEWTON MA.
- Siegrist, C., & Bruschini, C. (2002). Metal Detectors for Humanitarian Demining: a Patent Search and Analysis. *The European Union in Humanitarian Demining*.
- Sikora, R., Gratkowski, S., Komorowski, M., Pacuk, J., Enokizono, M., Chady, T., & Kliem, H. (2001). Application of magnetoresistive sensors for eddy current non-destructive testing of materials. In *AIP Conference Proceedings*, Vol. 557, pp.977.
- Sikora, R., Chady, T., Gratkowski, S., Komorowski, M., & Stawicki, K. (2003). Eddy current testing of thick aluminum plates with hidden cracks. *AIP Conference Proceedings*, Vol. 657, pp.427.
- Smith, C. H., & Schneider, R. W. (1999). Low-field magnetic sensing with GMR sensors. *Sensors EXPO*.
- Smith, C. H., & Schneider, R. W. (2000). GMR and SDT Sensors and Arrays for Low-Field Magnetic Applications. *NVE Low Field Sensing Papers & Presentations*.
- Stutzke, N. A., Russek, S. E., Pappas, D. P., & Tondra, M. (2005). Low-frequency noise measurements on commercial magnetoresistive magnetic field sensors. *Journal of applied physics*, 97(10), 10Q107-10Q107.
- Timofeeva, M., Allegre, G., Robbes, D., Gasnier, J., & Flament, S. (2011). Optimized Mini Search Coil Magnetometer Suited To Large Bandwidth Applications. In *SENSORDEVICES 2011, The Second International Conference on Sensor Device Technologies and Applications*, pp. 34-37

- Tondra, M., Daughton, J. M., Wang, D., Beech, R. S., Fink, A., & Taylor, J. A. (1998). Picotesla field sensor design using spin-dependent tunneling devices. *Journal of applied physics*, 83(11), pp.6688-6690.
- Torres, V., Gaydecki, P., Miller, G., Fernandes, B., & Zaid, M. (2005). The use of magnetoresistors for imaging steel bars in concrete. *AIP Conference Proceedings*, Vol. 760, pp.1453.
- Tumanski, S. (2007a). Induction coil sensors—A review. *Measurement Science and Technology*, 18(3), R31.
- Tumanski, S. (2007b). Scanning of magnetic field as a method of investigations of the structure of magnetic materials. *Przegląd Elektrotechniczny*, 1, 108-112.
- Tumanski, S. (2010). *Thin film magnetoresistive sensors*. CRC Press.
- Tumanski, S., & Liszka, A. (2002). The methods and devices for scanning of magnetic fields. *Journal of magnetism and magnetic materials*, 242, pp.1253-1256.
- Vértesy, G., Gasparics, A., & Szöllösy, J. (2000). High sensitivity magnetic field sensor. *Sensors and Actuators A: physical*, 85(1), 202-208.
- Vopálenský, M., Ripka, P., & Platil, A. (2003). Precise magnetic sensors. *Sensors and Actuators A: Physical*, 106(1), pp.38-42.
- Vopálenský, M., Ripka, P., Kubík, J., & Tondra, M. (2004). Alternating biasing of SDT sensors. *Sensors and Actuators A: Physical*, 110(1), pp.182-186.
- Wincheski, B., & Namkung, M. (2000). Deep flaw detection with giant magnetoresistive (GMR) based self-nulling probe. In *AIP Conference Proceedings*, Vol. 509, pp.465.
- Wincheski, B., Simpson, J., Namkung, M., Perey, D., Scales, E., & Louie, R. (2002). Development of giant magnetoresistive inspection system for detection of deep fatigue cracks under airframe fasteners. In *AIP Conference Proceedings*, Vol. 615, pp.1007.
- Wold, R. J., Nordman, C. A., Lavelly, E., Tondra, M., Lange, E. H., & Prouty, M. (1999). Development of a handheld mine detection system using a magnetoresistive sensor array. *AeroSense'99*, pp.113-123.
- Yashan, A., Bisle, W., & Meier, T. (2006). Inspection of hidden defects in metal-metal joints of aircraft structures using eddy current technique with GMR sensor array. *Proc. 9th ECNDT, Berlin*.
- Zhang, Y., Steiger, M., Hibbs, A. D., Grimm, R. E., & Sprott, T. A. (2010). Dual-mode, fluxgate-induction sensor for UXO detection and discrimination. *Journal of Environmental & Engineering Geophysics*, 15(2), pp.51-64.
- Zimmermann, E., Verweerd, A., Glaas, W., Tillmann, A., & Kemna, A. (2005). An AMR sensor-based measurement system for magnetoelectrical resistivity tomography. *Sensors Journal, IEEE*, 5(2), 233-241.

6 Attachment: Other publications related to the thesis topic

I participated in multiple projects at the Department of measurement. Following are four papers, related to the topic of magnetic sensors and gradiometers, which I am coauthor of. My contribution to this work was participation on hardware design and experiments.

6.1.1 Compact magnetic gradiometer and its astatization

This gradiometer is made of fluxgate sensors which consist of ring cores with the diameter of 12 mm. Two sensors create the gradiometer with a base length of 30 mm. The AMR gradiometer with a similar 40-mm base was presented in chapter 3.2.1, so direct comparison of both the AMR and fluxgate technologies can be made in two gradiometers with similar complexity of the external circuitry.

The noise power spectrum density at 1 Hz is for the fluxgate gradiometer $1\text{nT}/(\text{m}\sqrt{\text{Hz}})$ and for the AMR gradiometer $100\text{ nT}/(\text{m}\sqrt{\text{Hz}})$, when recalculated to the identical base length of 30 mm. AMR sensors with lower noise level are available, than the KMZ51 sensor has in the AMR gradiometer. But generally fluxgate technology is preferable when low noise is a priority.

The next important parameter of a gradiometer is its spurious sensitivity to homogeneous field. Misalignment of sensitive axes and different sensitivity constants will cause different output reading of both sensors in the gradiometer, even when they experience the same magnetic field. Therefore, if the gradiometer is rotated in the homogeneous field, the gradiometer output is changing as if a gradient field is detected. When rotated in the Earth's field, the fluxgate gradiometer has a spurious sensitivity of $\pm 50\text{ nT}/\text{m}$ and the AMR gradiometer $\pm 5000\text{ nT}/\text{m}$ (same base length considered). The AMR gradiometer was however operated without any calibration.



EUROSENSORS 2015

Compact magnetic gradiometer and its astatization

Michal Janošek^{a*}, Jan Vyhnánek^a and Antonín Platil^a

^a*Czech Technical University in Prague, Technická 2, 166 27 PRAHA, Czech Republic*

Abstract

We present a compact (10-cm head size, 3-cm base) axial magnetic gradiometer with a method of its astatization (i.e. suppression of false response to homogeneous field). For astatization, we use two integrated orthogonal sensors and a second-order polynomial correction; after astatization the gradiometer error is suppressed more than 1000×. The gradiometer has been successfully used in a real-world metal-detection task which was allowed by the low gradiometer astatization error of ± 50 nT/m and its noise of 1 nT/(m $\sqrt{\text{Hz}}$) @ 1 Hz.

© 2015 The Authors. Published by Elsevier Ltd.

Peer-review under responsibility of the organizing committee of EUROSENSORS 2015.

Keywords: gradiometer;astatization;noise;fluxgate;

1. Introduction

Compact gradiometer has several important advantages, mainly the ability to suppress even relatively close magnetic disturbances. For close sources, the advantage of small gradiometric base is the possibility to determine the magnetic field gradient more precisely [1]. Our gradiometer consists of two ring-core fluxgate sensors, with 30-mm gradiometric base, and sharing common gradient feedback and homogeneous feedback coils [2] – see Fig. 1a.

The small base however emphasizes geometric imperfections, astatization (suppression of false response to homogeneous field) is thus necessary for real-world scenarios. For example in metal-detection, the gradiometer head may be positioned arbitrarily in the Earth's magnetic field (48 μT in our case) and the gradiometer error due to the large homogeneous common-mode can mask the desired response. Even for a state-of-the-art highly-balanced SQUID gradiometer with a gradiometric base of 35 mm [3], a compensation technique was necessary to achieve less than 2 nT/m error due to movements in the Earth's field and finite common-mode rejection of the gradiometer.

* Corresponding author. Tel.: +420-22435-3964; fax: +420-2333-39929.

E-mail address: janosem@fel.cvut.cz

As opposed to other approaches using multiple scalar calibrations [4] or establishing the angular deviations [2, 5], we propose an alternative gradiometer astatization method. In comparison with [3], our approach utilizes higher-order correction terms allowing for better astatization results.

Nomenclature

G_{zz}	Gradient tensor component estimation $\partial B_z/dz$ [T/m]
M_z	Measured values of homogeneous field B_z (in engineering units) [-]
$G_{corr_{zz}}$	Corrected (astatized) G_{zz} with response to homogeneous fields suppressed [T/m]

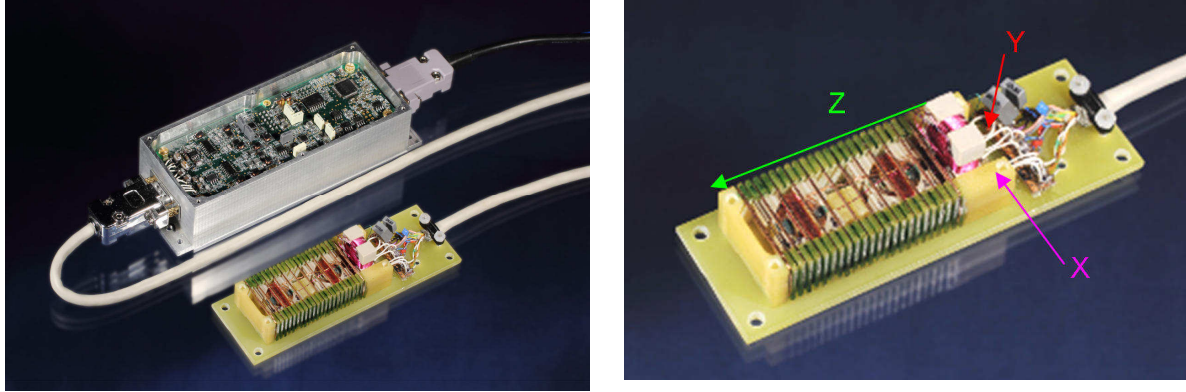


Figure 1: a) The compact gradiometer and its electronics. b) The gradiometer head detail - Z is the main sensing direction, X and Y are the orthogonal directions

2. Gradiometer astatization

For a two-sensor gradiometer with base d , with the two sensor readings M_{z1} and M_{z2} and sensitivities (scale constants) S_{z1} and S_{z2} [T^{-1}], we can define the uncorrected gradient estimation $G_{zz} \approx \partial B_z/dz$ (if no astatization was used):

$$G_{zz} = \frac{B_{z1} - B_{z2}}{d} = \frac{1}{d} \left(\frac{M_{z1}}{S_{z1}} - \frac{M_{z2}}{S_{z2}} \right) \quad (1)$$

We propose a method of gradiometer astatization by the use of information about the orthogonal components of homogeneous field sensed by the X-Y orthogonal sensor pair (M_x, M_y) and by the homogeneous compensation coil coaxial to the gradient coil (M_z). We propose that the corrected gradient $G_{corr_{zz}}$ can be estimated as:

$$G_{corr_{zz}} = G_{zz} - [k_1 \quad k_2 \quad k_3] \cdot \begin{bmatrix} M_x \\ M_y \\ M_z \end{bmatrix} - [k_4 \quad k_5 \quad k_6] \cdot \begin{bmatrix} M_x^2 \\ M_y^2 \\ M_z^2 \end{bmatrix} \quad (2)$$

It is sufficient to know the M_x, M_y, M_z values in engineering units only, since the inverse sensitivities are already part of the coefficients k_1 - k_6 . Having a large set of calibration points similar to the calibration presented in [2] in a gradient-free location, thus assuming $G_{corr_{zz}}=0$, we get a linear system – an overestimated set of equations, allowing to find k_1 to k_6 by SVD matrix decomposition:

$$[k_1 \quad \dots \quad k_6] = \begin{bmatrix} M_x \\ \dots \\ M_z^2 \end{bmatrix}^{-1} G_z \quad (3)$$

After astatization using the established k_1 to k_6 coefficients and the Equation 2, the gradiometer error was reduced from $\pm 50\,000$ nT/m to ± 50 nT/m – see Fig. 2. The residual error after astatization did not depend on orientation to the Earth’s field demonstrating the suitability of the algorithm. For practical use, the error is even lower for a limited movement of the probe.

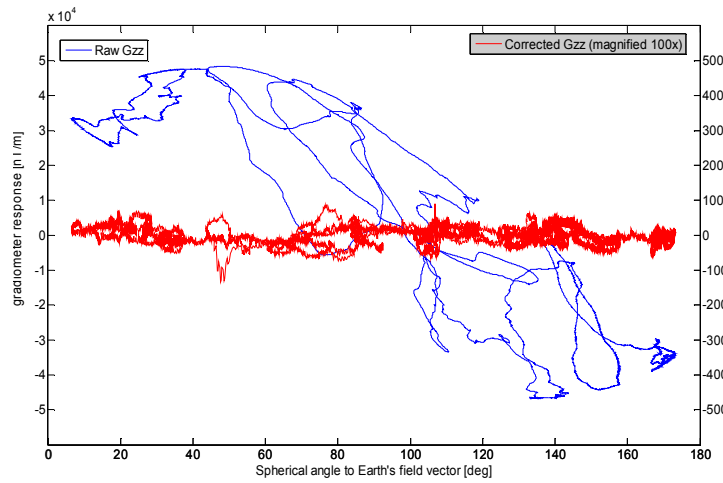


Figure 2 - The gradiometer response to homogeneous field in various orientations to the Earth's field vector - before and after astatization

Gradiometer performance

The gradiometer with small gradiometric base cannot compete with large 1-m base systems; however it allows to obtain accurate gradient information about weak and near sources [1]. For example we could estimate a source of $1.8 \times 10^{-2} \text{ Am}^2$ strength (35 cm^3 magnetized iron ore piece) with 10% error in a 20-cm distance, whereas 2-points magnetometric method yielded a 40% error. The low gradiometer noise ($1 \text{ nT/m}/\sqrt{\text{Hz}}$) allowed 30-cm field detection distance of a $5 \times 10^{-4} \text{ Am}^2$ source, which can be e.g. a 1 cm^3 chondrite [6]. Field trials of the gradiometer have been performed in a public park showing the feasibility of astatization: without it, the test objects (permanent magnets and various steel objects) could not be detected because of the parasitic response of the gradiometer – see Fig. 3.

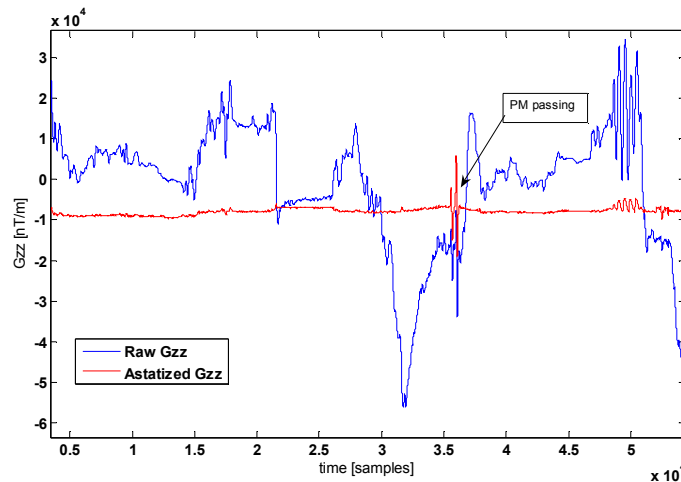


Figure 3 – a): the gradiometer probe (mounted at bottom) with (D)GPS on the top. b) gradiometer response with/without astatization

After processing the data and DGPS position, we could map the strongest sources according to Fig. 4 – we used 5-Hz output of the GPS and no artificial grid when scanning the scene with the device of Fig. 3a.

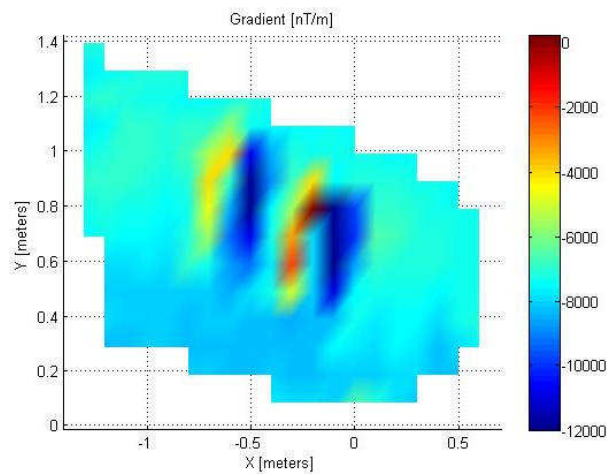


Figure 4 - Gradient field map of the search area from DGPS positions and probe signal showing two dipole field sources.

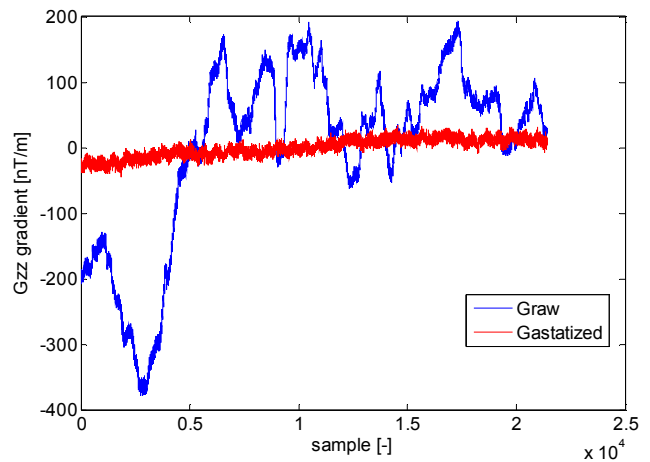


Figure 5 - Stationary log of gradient signal

The gradient noise measured at a location of this kind provides valuable information. This time, the probe was kept fixed, and the output was logged for 2 minutes. The noise in Fig. 5 shows that astatization improves the noise floor of the gradiometer even when it is fixed in the Earth's field – the raw gradiometer output still contains the large homogeneous noise from distant sources (DC powered subway, DC electric train traction) due to angular misalignments of the two gradiometer sensors. After astatization, the gradiometer noise decreased about 30 \times .

Conclusion

The presented method for compensating the gradiometer spurious sensitivity to homogeneous field was applied to a compact gradiometer with the help of additional outputs giving information about the three homogeneous field components. With a 3-cm gradiometric base, the error due to the motion in the Earth's field decreased 1000-times down to ± 50 nT/m. A field trial was conducted showing feasibility of such gradiometer and we have also shown that even for a static position, gradiometer astatization is necessary to suppress strong field noise of distant sources – this could be a problem for other gradiometers relying only on gain adjustment, assuming perfect alignment of gradiometric probes [7].

References

- [1] M. Janosek, A. Platil, J. Vyhnanek, The effect of sensor size on axial gradiometer performance, *IEEE Trans. Magn.* 51 (2015), #4002504
- [2] M. Janosek, A. Platil, J. Vyhnanek, J. Brinek, Dual-core fluxgate gradiometer with gradient feedback, *IEEE Sensors 2013* (2013), 1-3.
- [3] A. Chwala, Full Tensor SQUID Gradiometer for airborne exploration, *ASEG Extended Abstracts, 22nd Geophysical Conference* (2012), 1-4
- [4] J. Tomek et al., Suppression of Environmental Noise in Magnetopneumography by the use of Higher Order Gradients, *IEEE Transactions on Magnetism* 48.4 (2012), 1317-1319.
- [5] José MG Merayo et al, A portable single axis magnetic gradiometer, *Sensors and Actuators A: Physical* 93.3 (2001), 185-196.
- [6] L. J. Pesonen, M. Terho, I. T. Kukkonen, Physical properties of 368 meteorites: implications for meteorite magnetism and planetary geophysics, *Proc. NIPR Symp. Antarct. Meteorites* 6 (1993), 401-416.
- [7] A.L.Elrefai, I. Sasada, S. Harada, Gradiometer and Magnetometer Integration by Using a Pair of Fundamental Mode Orthogonal Fluxgate Sensor Heads, *IEEE Transactions on Magnetism*, in press (2015)

6.1.2 Simple estimation of dipole source z-distance with compact magnetic gradiometer

The gradiometer described in the previous paper is used as a distance sensor. A simple formula is derived to obtain an estimation of the distance between a dipole and the gradiometer. Experiments specify limits of the method with respect to orientation and lateral displacement of the dipole.

Simple estimation of dipole source z-distance with compact magnetic gradiometer

M Janošek, A Platil¹ and J Vyhnánek

Czech Technical University in Prague, Technická 2, 166 27 Prague, Czech Republic

E-mail: platil@fel.cvut.cz

Abstract. A compact magnetometer/gradiometer with combined homogeneous and gradient outputs facilitates precise measurement of both H and G values with good spatial and temporal coherence. By evaluating combination of both signals, it is possible to estimate distance to a dipole source with relatively small error and largely independent from precise knowledge of source strength, orientation and lateral displacement. The performance is limited primarily by ambient noise. With an AC-driven source, tool navigation or distance sensing is also possible.

1. Introduction

We have previously presented a compact (10-cm head size, 3-cm base) axial magnetic gradiometer with two ring-core fluxgate sensors and combined homogeneous feedback and gradient feedback coils [1]. This arrangement provides simultaneously information about the homogeneous field strength B_z as well as the gradient dB_z/dz in one axis with minimal geometric error. Thanks to that we can utilize simple method of dipole source distance estimation [2, 3]. Such an information is needed e.g. for unexploded-ordnance-detection or mine-hunting [4]. In our method, we do not obtain the radial distance, but the z -, or the vertical distance to the detected object, which is one of the most important informations to distinguish between deep and strong sources and shallow and weak ones. Assuming constant background conditions (both homogeneous field H and gradient G), the vertical distance (z -component) to a source positioned along the gradiometer axis can be estimated with relatively low error simply from the ratio of H_z and G_{zz} signals, largely independent from radial distance to the dipole, and its strength. If we calculate $3 \times H_z / G_{zz}$, we get a figure characterizing the distance to source directly from one reading - not depending on its actual amplitude - this approach can be used also with AC-current driven coils for distance measurements or tool navigation tasks.

2. Experiment

The sensor was fixed in space after H and G readings in "infinity" (i.e. far from dipole source) were recorded as offsets for later subtraction from data. The dipole source in our case is small ($13 \times 4 \times 5 \text{mm}^3$) NdFeB permanent magnet. In the first experiment, the sensor and dipole were aligned on the same axis (z), with the dipole axis oriented either coaxially or perpendicularly - see figure 1 (left). The vertical distance (z) was modified and the corresponding distance estimate from H and G

¹ To whom any correspondence should be addressed.



data was calculated. In the following experiment, the vertical (z) distance was fixed at 15 cm and lateral displacement (y) was modified - again, see figure 1 (left) for the geometry of the setup.

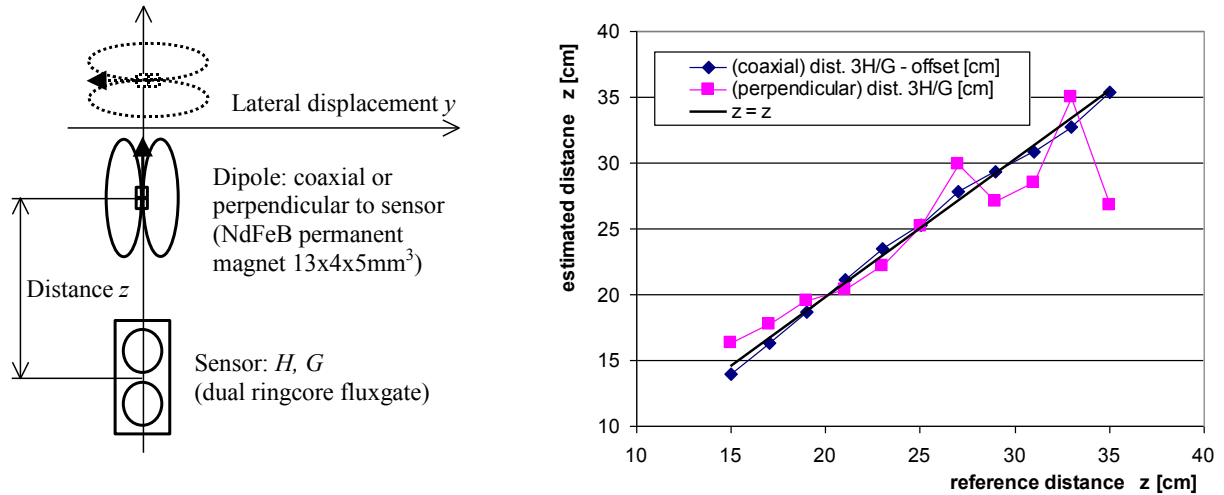


Figure 1. Left: the geometrical situation of dipole and sensor. Right: the estimated distance vs. real (reference) distance to a dipole in coaxial or perpendicular orientation to sensor. For coaxial orientation, an offset must be subtracted from the estimate. Here, the lateral displacement y is 0 cm.

3. Theory

As was shown in [2] and several related papers, measurement of full tensor gradient and field vector provides information for dipole source position estimate, irrespective of dipole orientation relative to sensor. In [2] the source is loop antenna transmitting AC signal. In our approach, we simplified the setup to just combined single-axis magnetometer and gradiometer. Also the dipole in our case was permanent magnet within Earth's field. In spite of these limitations, we achieved reasonably good position estimates, albeit in limited range of distances.

If we assume z - orientation of the magnetic dipole (magnetic moment m_z), we can write for the z -component of the magnetic field B_z :

$$B_z = -\nabla\left(\frac{\mu_0 \cdot m_z \cdot z}{4\pi \cdot z^3}\right) = -\nabla\left(\frac{\mu_0 \cdot m_z}{4\pi \cdot z^2}\right) = \frac{2\mu_0 \cdot m_z}{4\pi \cdot z^3} \quad (1)$$

The G_{zz} gradient can be then written as:

$$G_{zz} = \frac{\partial B_z}{\partial z} = -\nabla\left(\frac{\mu_0 \cdot m_z}{2\pi \cdot z^3}\right) = \frac{-3\mu_0 \cdot m_z}{2\pi \cdot z^4} \quad (2)$$

$$\text{By dividing } B_z \text{ and } G_{zz}, \text{ we get finally: } z = -3 \times \frac{B_z}{G_{zz}} \quad (3)$$

This result is consistent with the tensor representation presented in [2].

4. Results and discussion

As shown in figure 1 (right), the estimated distance from $3 \times H/G$ matches with reference distance quite well in 15-30 cm range. The estimate for coaxial case contained an unwelcome position offset (about 7cm), but after subtraction thereof, the error is 1cm or less. The data from perpendicular case are more influenced by noise due to lower dipole signal strength in 2nd Gauss position.

In the second measurement, the influence of lateral displacement (along y-axis) on distance (z) estimate was examined. The dependence of homogeneous field H_z and G_{zz} gradient on y-axis position of dipole is shown in figure 2, again for coaxial and perpendicular orientation of dipole. The position $y = 0$ corresponds to alignment of dipole with sensor from first experiment. From the same data, position estimates are again calculated. The quality of estimated z-distance quickly deteriorates by more than 100 % - see figure 3 and figure 4, but for small lateral displacements (< 5 cm) the error is quite acceptably low. Dashed line represents true z-distance 15 cm. Note that in figure 3, the estimated distance z is not corrected for offset.

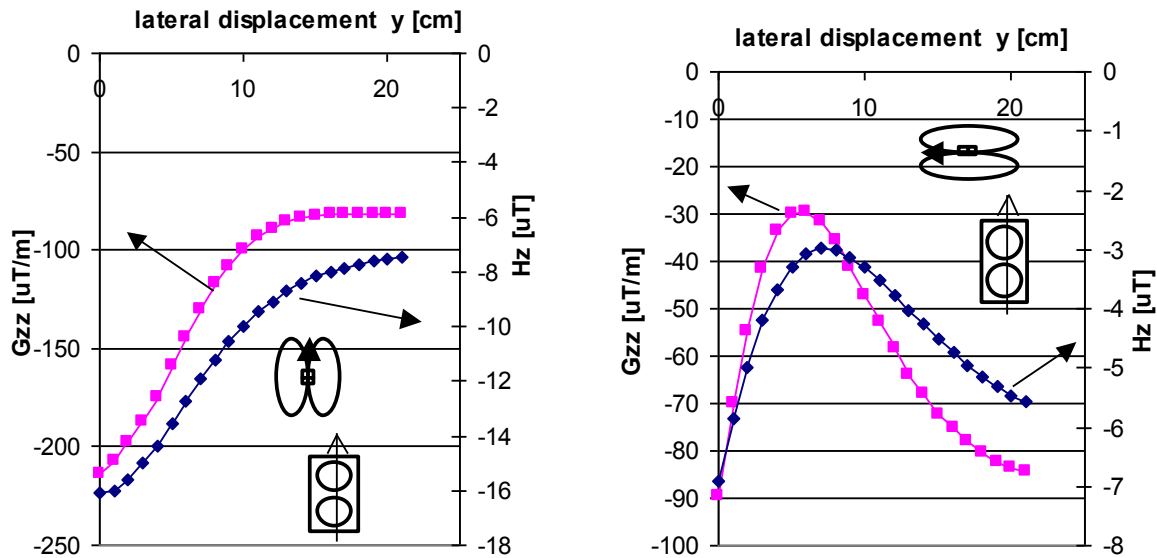


Figure 2. The measured homogeneous magnetic field and gradient in coaxial (left) and perpendicular (right) orientation of dipole to sensor vs. lateral displacement along y-axis.

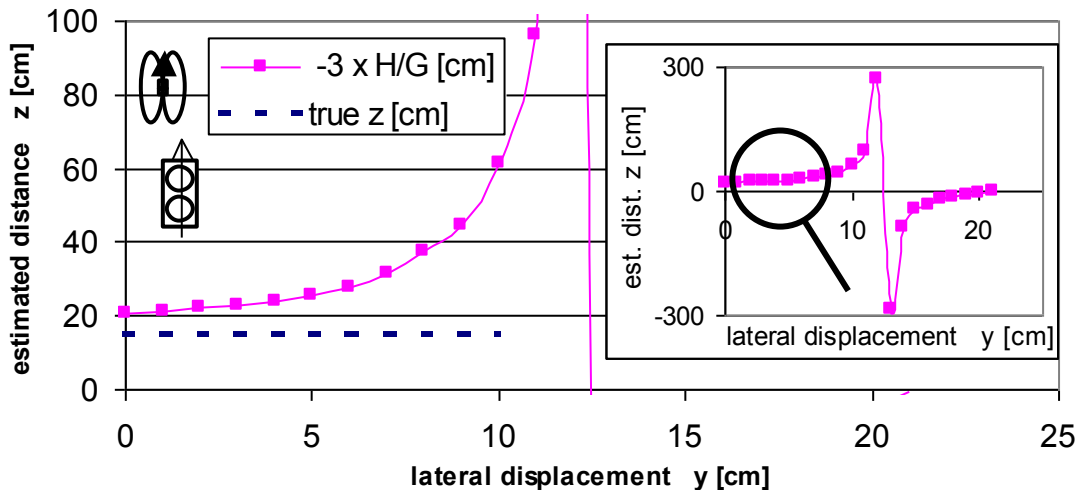


Figure 3. Coaxial orientation. The estimate of distance z vs. lateral displacement along y-axis. In limited range of lateral displacements (< 5 cm), the estimate error is small (< 5 cm after offset removal). The inset shows overall response for large lateral displacements (detail in main graph).

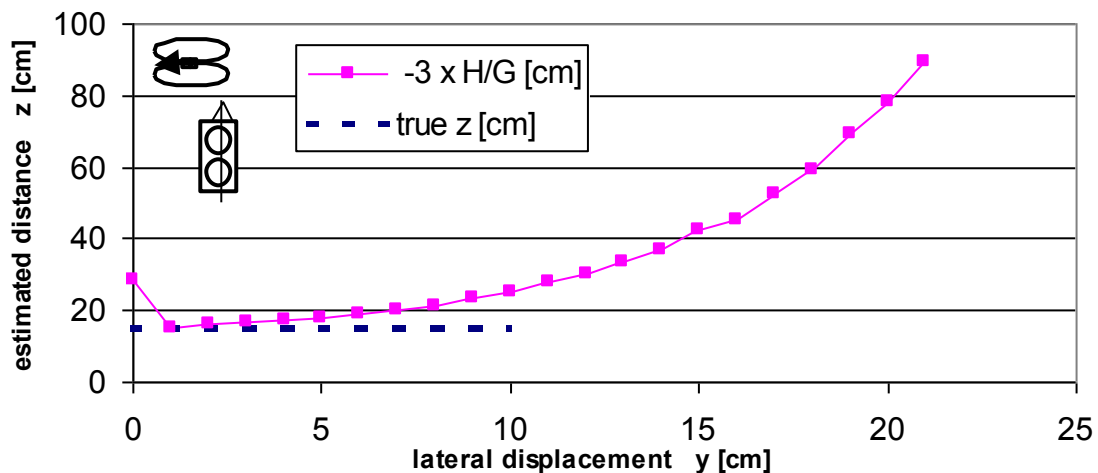


Figure 4. Perpendicular orientation. The estimate of distance z vs. lateral displacement along y -axis. In limited range of lateral displacements (1 - 7cm), the estimate error is small (< 3 cm).

5. Conclusions

We conducted several experiments with dipole distance estimation in 15 cm to 30 cm distance. After offset subtraction, the distance estimation error in our experiment with small NdFeB source was < 5 cm for coaxial case and < 3 cm for perpendicular case in 15 cm to 30 cm dipole-to-gradiometer distance. Moreover, the z -axis distance estimation was largely independent (within some limits) to axial misalignment (lateral shift) between the source and gradiometer axes. The performance was mainly limited by ambient noise, which was about $100\times$ larger than our gradiometer noise ($1 \text{ nT/m}/\sqrt{\text{Hz}}$). AC-driven coils experiment was also conducted showing feasibility of the proposed algorithm e.g. for tool navigation purposes or for distance sensors.

References

- [1] Janosek M, Platil A, Vyhnanek J and Brinek J 2013, Dual-core fluxgate gradiometer with gradient feedback *IEEE Sensors 2013 Proceedings*, DOI: 10.1109/ICSENS.2013.6688287
- [2] Nara T, Suzuki S and Ando S 2006, A closed-form formula for magnetic dipole localization by measurement of its magnetic field and spatial gradients *IEEE Transactions on Magnetics* **42** 3291-93.
- [3] Young, JA, Clark DA 2010, Magnetic tensor gradiometry in the marine environment *International Conference on Electromagnetics in Advanced Applications (ICEAA)* pp 701-4, DOI: 10.1109/ICEAA.2010.5650898
- [4] Wiegert R, Oeschger J and Tuovila E 2007, Demonstration of a novel man-portable magnetic STAR technology for real time localization of unexploded ordnance *OCEANS 2007, IEEE conference*, 2007, DOI: 10.1109/OCEANS.2007.4449229

6.1.3 The Effect of Sensor Size on Axial Gradiometer Performance

This paper deals with the error of the gradient estimation, when a gradiometer is close to the source of a dipole magnetic field. Different values are therefore obtained by measuring with sensors of different size and construction. Experimental comparison of AMR and fluxgate sensors is described. Theoretical models for ringcore, racetrack and rectangular sensors are provided and verified.

The Effect of Sensor Size on Axial Gradiometer Performance

Michal Janošek, Antonin Platil, and Jan Vyhnánek

Czech Technical University in Prague, Prague 166 36, Czech Republic

In this paper, we examine the influence of sensor size, sensor spacing (gradiometric base), and distance from dipole source on the performance of a single-axis gradiometer positioned along the dipole axis. The case of a finite base gradiometer with ideal sensors is considered, then the influence of finite-size sensing elements is modeled, and finally, a comparison with experimental results obtained with two ring-core and race-track fluxgates and two anisotropic magnetoresistors (AMRs) is evaluated. Some of the effects found may be counterintuitive, and especially in close proximity of the dipole source, the gradient cannot be further modeled by simplified uniaxial approximation because of the active element size. Full Biot–Savart field model was considered in those cases.

Index Terms—Gradient, magnetic field measurement, magnetic sensors, noise, resolution.

I. INTRODUCTION

THE gradiometric arrangement of measurement setup is especially suitable for measuring magnetic field from relatively close sources in presence of relatively large homogeneous background field. Axial magnetic gradiometers are usually built with uniaxial magnetic sensors aligned in one direction [1]. The sensor type depends on application and precision required—sensitive room-temperature gradiometers use fluxgate or AMR sensors [2]. They can be used for detection of buried ferromagnetic objects, magnetic markers, biomagnetism [3]–[7], and so on.

In our case, the gradient (ideally a point-defined quantity) is approximated from the readings of two homogenous field sensors separated by a known distance (other arrangements with truly gradiometric sensors are not considered here). When the gradient base and sensor size are comparable with the source distance, and moreover when the source is dipolar and weak—e.g., when detecting the response of magnetic nanoparticles—the situation is more complicated.

In this paper, we examine the influence of sensor size, sensor spacing (gradiometric base), and distance from a dipole source on the performance of a single-axis gradiometer positioned along the dipole axis. A similar study was done by finite-element modeling in [5] for the determination of point spread function for the horizontal displacement from a dipolar source.

With finite-size sensing elements (ring and race-track core for fluxgate, stripe structure for AMR), some averaging of the measured field along the structure can be expected, however this effect has not been widely discussed in literature. We modeled the influence of finite-size sensing elements for the case of different sensor geometries, and finally evaluated the experimental results obtained with the real sensors.

II. INITIAL EXPERIMENT

Let us consider the following measurement setup. The dipole source is located in a distance—here called *L*—from the first gradiometer probe consisting of

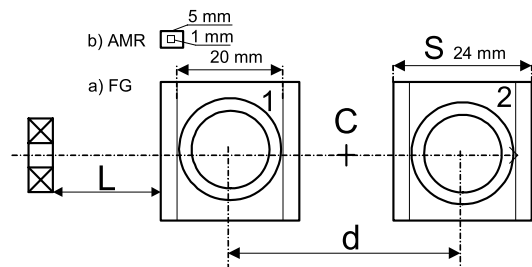


Fig. 1. Fluxgate gradiometer (AMR sensor shown for comparison).

sensor 1 and 2 (Fig. 1). We have used two fluxgate sensors (depicted) or AMR sensors with 5 mm × 5 mm chip size in an unshielded laboratory environment. The dipole moment of the 5 mm diameter, three-turns coil was 5.2×10^{-6} Am². The liftoff of the gradiometer was 10, 20, and 60 mm, respectively, and the second sensor was moved to increase the gradient base *d*.

The SNR was calculated from the two sensor readings and respective gradiometer noise without the signal (70 Hz was used for measurements in a narrow 1 Hz bandwidth; SNR is thus higher than for broadband measurements)

$$\text{SNR} = 20 \log \frac{(U_1 G_1 - U_2 G_2)}{\sqrt{(N_1^2 + N_2^2)}} \quad (1)$$

where U_1 and U_2 are the sensor output voltages, G_1 and G_2 are the respective sensor gains, and N_1 and N_2 are the (uncorrelated) magnetic noise output by the sensors.

In Fig. 2 we can see that to obtain the same SNR of ~45 dB, either an AMR gradiometer with a 25 mm base and 20 mm liftoff or a fluxgate gradiometer with the same base, however, with 10 mm liftoff only can be used. For the largest 60 mm liftoff, the higher AMR sensor noise causes a decrease in SNR. A detailed view on the data from Fig. 2 is shown in Fig. 3—the relative change in SNR from its saturation value is shown, as the gradiometric base is decreased. The 10 and 20 mm liftoffs are shown; the 60 mm liftoff was not plotted as the data were already affected by AMR sensor noise.

The decrease in SNR when decreasing the gradiometric base is almost 5 dB if the AMR gradiometer is very close toward the dipole source (due to relatively close sensor readings).

Manuscript received June 13, 2014; revised August 25, 2014; accepted September 15, 2014. Date of current version January 26, 2015. Corresponding author: M. Janošek (e-mail: janosem@fel.cvut.cz).

Color versions of one or more of the figures in this paper are available online at <http://ieeexplore.ieee.org>.

Digital Object Identifier 10.1109/TMAG.2014.2359960

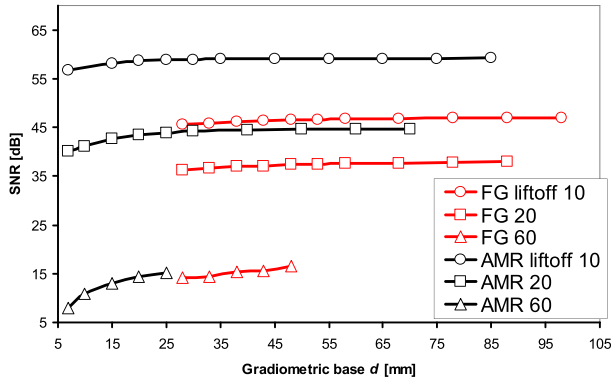


Fig. 2. Gradiometer SNR for $L = 10, 20,$ and 60 mm.

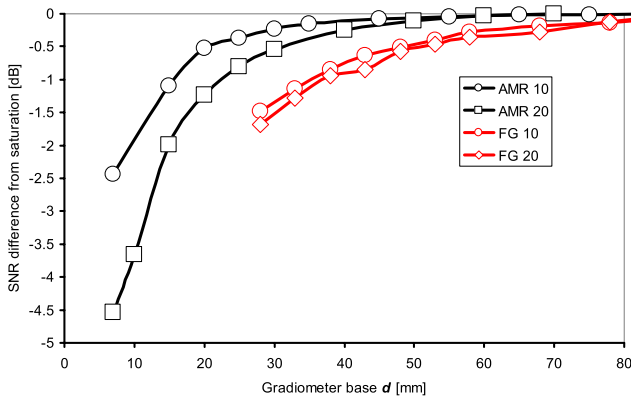


Fig. 3. SNR difference from the saturation SNR (Fig. 2) versus gradient base d .

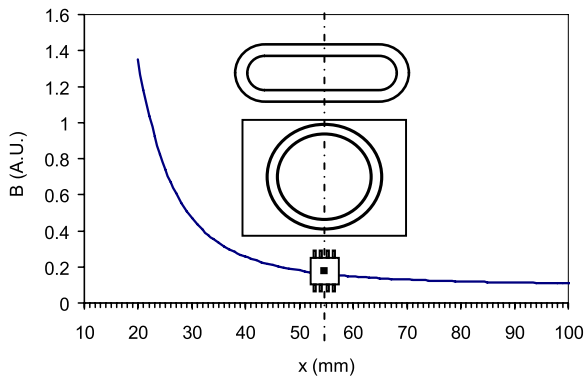


Fig. 4. Dipolar field and sensor size—illustration of the size effect—three different sensors (AMR, ring-core, and race-track fluxgate) have their sensing elements exposed to a spatially variable magnetic field on a different scale.

However, for the same gradiometric bases and liftoffs, the fluxgate gradiometer shows faster decrease in SNR than AMRs. This would indicate that there is an averaging-like effect that depends on sensor size.

III. SENSOR GEOMETRY EFFECT

The effect of gradiometer base length on gradiometer reading was already discussed in [1]. However, for small distances from the source, the real sensing element geometries of the respective sensors should be considered. The sensor active

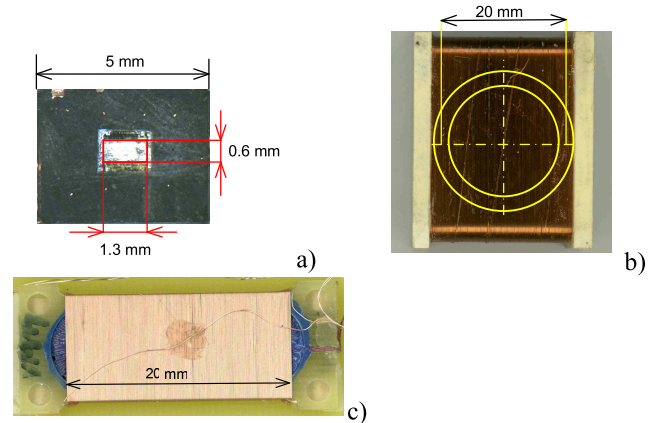


Fig. 5. Active element dimensions. (a) KMZ51. (b) Ringcore fluxgate. (c) Race-track fluxgate (not to scale).

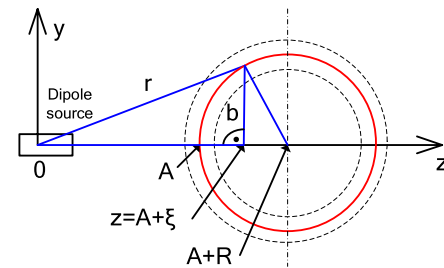


Fig. 6. Ringcore active element with notation considered in the calculations.

length impacts its output reading when related to an ideally small (short) sensor located at the same central point—a demonstration is shown in Fig. 4 for a dipolar field. It is clear that the AMR sensor will have its reading closer to reality than the fluxgate sensor with a wide magnetic core and this might affect the gradiometer reading and performance.

We estimated from the disassembled package that the AMR KMZ 51 sensor has its internal sensing structure 1.3 mm long and 0.6 mm wide [Fig. 5(a)]. Our ring-core fluxgate has its core with a mean diameter of 20 mm fully covered by the 22 mm wide combined pickup-compensation coil [Fig. 5(b)]. The race-track fluxgate [Fig. 5(c)] has its longitudinal branches 20 mm long and the mean racetrack width is 8 mm.

If we consider a magnetic field sensor with a uniform pickup coil or a uniform sensing structure across its magnetic element (the case of fluxgate and AMR), its field response is affected by the mean value of the response across the magnetic sensing elements. The high-permeability magnetic material does not flatten the magnetic field profile as it was shown with the so-called single-core fluxgate gradiometers [7], where the field profile across the magnetic core is used for gradiometer operation. We also assume that the sensor is feedback compensated, which is a standard technique, thus its demagnetization factor [8] further affecting its gain has not to be considered since it works as zero detector in the loop.

The situation of the fluxgate ring core in a dipolar field is shown in Fig. 6. The core geometry has been simplified to a circle with mean radius R , with its lower z -coordinate A and

upper $A + 2R$. Its effective sensitivity is then a function of the distance $z = A + \zeta$ from the magnetic dipole.

The magnetic field component in z -direction is from the Biot–Savart law, a function of both the z -coordinate and radial distance r

$$B_Z = M \frac{\mu_0}{4\pi} \left[\frac{3z^2}{r^5} - \frac{1}{r^3} \right]. \quad (2)$$

Let us define the sensitivity function b assuming the integration path between A and $A + 2R$ (Fig. 6) with an increment of ζ

$$b = \sqrt{R^2 - [A + R - (A + \zeta)]^2} = \sqrt{R^2 - (A + R - z)^2}. \quad (3)$$

We can also write for the radial distance r

$$r = \sqrt{b^2 + z^2}. \quad (4)$$

We can then express (2) describing the z field component at each point across the ring half-circumference (the second half is not considered due to fluxgate sensor symmetry)

$$B_Z = M \frac{\mu_0}{4\pi} \left\{ \frac{3z^2}{[b^2 + z^2]^{\frac{5}{2}}} - \frac{1}{[b^2 + z^2]^{\frac{3}{2}}} \right\}. \quad (5)$$

Finally, the spatial integral of the measured field across the sensing element length can be expressed by integrating the product of the two functions (3) and (5)

$$\int B_{\text{ring}} = \int_A^{A+2R} b(z) \cdot B_z(z) \cdot dz. \quad (6)$$

If we assume that the sensor works in a feedback loop and that the feedback coil also fully covers the respective sensing element (Fig. 5), we can express the spatial average flux density, which is compensated by the feedback field (created by feedback coil) in a closed-loop operation, assuming that the feedback field is homogeneous. We obtain it by dividing (6) with $\pi R^2/2$, which is the result of the integral (6) if the sensor would be exposed to a unit, homogeneous field ($B_z = 1$)

$$\overline{B_{\text{ring}}} = \frac{2}{\pi \cdot R^2} \int_A^{A+2R} b(z) \cdot B_z(z) \cdot dz \quad [T]. \quad (7)$$

For other sensor geometries, the situation would be analogical and the formalism of Fig. 6 can be used. For a race-track sensor, if we assume only its longitudinal branches with a unit sensitivity function, the resulting feedback field is

$$\overline{B_{\text{race}}} = \frac{1}{2R} \int_A^{A+2R} 1 \cdot B_z(z) \cdot dz. \quad (8)$$

The values of B_{ring} and B_{race} were solved numerically with Riemann sums for 5000 elements evenly spaced across the $2R$ distance.

For thin and long cores (i.e., Vacquier fluxgate) with the length $S = 2R$ and origin A as in Fig. 6, the calculation can

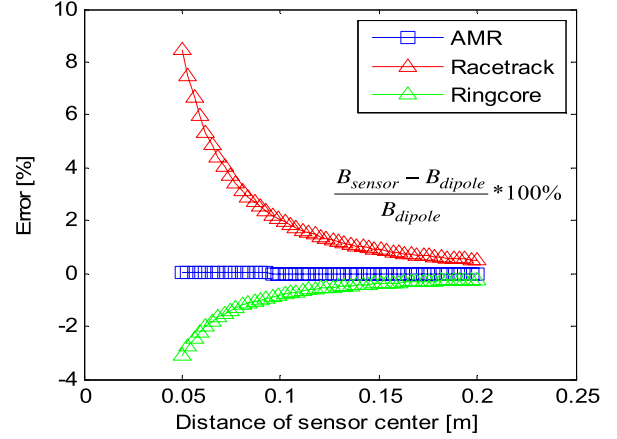


Fig. 7. Modeled response of the three sensors for different distances from dipole-field source.

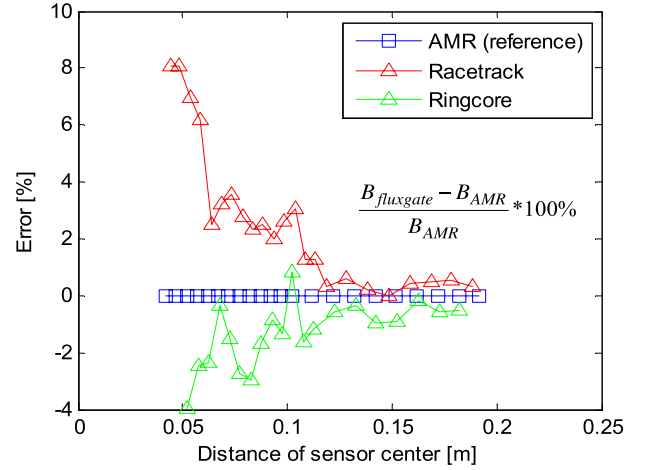


Fig. 8. Measured response of the three different sensors as a function of the distance from dipole-field source.

be simplified omitting the correction on b . Assuming again unit sensitivity per length element, we can directly solve

$$\overline{B_{\text{long}}} = \frac{1}{S} \frac{\mu_0}{4\pi} M \int_A^{A+S} \frac{1}{z^3} \cdot 1 \cdot dz = \frac{\mu_0}{4\pi S} M A^{A+S} \left[-\frac{1}{2z^2} \right] \quad (9)$$

$$\overline{B_{\text{long}}} = \frac{1}{S} \frac{\mu_0}{4\pi} M \frac{2AS + S^2}{2A^2(A + S)^2}. \quad (10)$$

The KMZ51 response was modeled using this equation not considering the negligible sensor width.

IV. MODEL VERIFICATION

To support the theory presented above, an experiment was arranged with the three above sensors using a 20 mm long solenoid creating a 7 Hz ac field. A sliding holder for the fluxgate and AMR sensors was mounted in the solenoid axis. The solenoid response was modeled to verify its character—at the lowest distance of 40 mm, the field was dipolar. The output of the two respective sensors has been evaluated with a fast Fourier transform spectrum analyzer. The gradiometric base d was 28, 31, and 48 mm, respectively. For fluxgate sensors, this resulted in sensor separation of 0, 3, and 20 mm, which

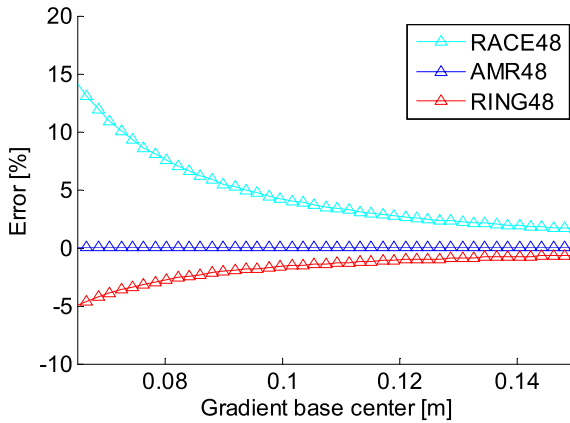


Fig. 9. The modeled 48 mm gradiometer error—data from simulation compared with an ideal 48 mm base gradiometer output.

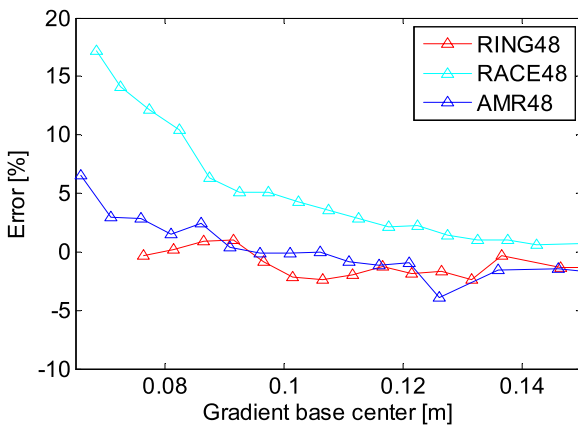


Fig. 10. The same comparison as in Fig. 9—measured data.

is a distance short enough to cause mutual influencing of the sensor feedback fields [1]. The fluxgate sensor gains were thus calibrated for each separation independently—their gain values differed by 4.3% and 3% for 0 and 3 mm separations compared with the 20 mm one. The AMR sensors due to their small size and thus larger separation for the same gradiometric base did not exhibit this error.

To confirm the proposed model, we have done following comparison. First, the theoretical and measured field values by the respective sensors were compared when measuring a dipole-field source with increasing distance to the sensor center ($L+S/2$) (Figs. 7 and 8). The response was normalized in both cases to the output of a theoretical, infinitely small sensor or the AMR in real case. From the two figures, it can be seen that proposed model agrees well with the measured data.

We have done the same also for a gradiometer. Fig. 9 shows the theoretical gradiometer response, as was calculated for the gradient base of 48 mm, in dependence on the distance from the dipole source (from the gradiometric base center).

The figure displays the error compared with an ideal value (if the gradiometer would have infinitely small sensors).

The measured data shown in Fig. 10 correspond well to the theoretical values in the case of the racetrack gradiometer. We see that the AMR gradiometer with a 48 mm base is well within $\pm 5\%$ measurement error, the ringcore gradiometer measures lower values when decreasing the distance, however, the racetrack gradiometer with the same base measures up to 20% more for the same close distances. The AMR gradiometer and ringcore fluxgate gradiometer errors, however, appear to be comparable with the measurement precision so their difference is not as clear as for the racetrack gradiometer. In addition, a systematic error due to mutual axial misalignment cannot be excluded.

V. CONCLUSION

We have shown that if a feedback-operated magnetic field sensor used in a gradiometer has comparable size with the gradiometric base and also the distance from the dipolar field source, several non-intuitive effects appear. The SNR of the gradiometer is shown to decrease when the gradiometric base is decreased or the gradiometer center is moved toward the dipole. Although the racetrack fluxgate might have the same length as the ring-core sensor, the response of the two gradiometers having same gradient base and being placed in identical positions was different—the racetrack gradiometer measured a larger value by 20%, when the distance from dipole source was approximately equal to the gradiometric base (48 mm). The AMR gradiometer was measuring close to theory. We have proposed a theoretical approach to explain this phenomenon by using the Biot–Savart law and integration across the respective sensing element—the response of each sensor was affected by its sensitivity function across the sensing element and by the non-uniform magnetic dipole field.

REFERENCES

- [1] J. M. G. Merayo, J. R. Petersen, O. V. Nielsen, F. Primdahl, and P. Brauer, "A portable single axis magnetic gradiometer," *Sens. Actuators A, Phys.*, vol. 93, no. 3, pp. 185–196, 2001.
- [2] J. Vyhnanek, M. Janosek, and P. Ripka, "Low frequency noise of anisotropic magnetoresistors in DC and AC-excited metal detectors," *J. Phys., Conf. Ser.*, vol. 450, nos. 1–5, p. 2031, 2013.
- [3] Q. A. Pankhurst, J. Connolly, S. K. Jones, and J. Dobson, "Applications of magnetic nanoparticles in biomedicine," *J. Phys. D, Appl. Phys.*, vol. 36, no. 13, p. R167, 2003.
- [4] J. Tomek, A. Platil, P. Ripka, and P. Kaspar, "Application of fluxgate gradiometer in magnetopneumography," *Sens. Actuators A, Phys.*, vol. 132, no. 1, pp. 214–217, 2006.
- [5] D. Rühmer, P. Shanmuganathan, F. Ludwig, and M. Schilling, "Spatial and field resolution of wire-wound fluxgates in magnetic dipole fields," *Sens. Actuators A, Phys.*, vol. 173, no. 1, pp. 30–35, 2012.
- [6] J. Tomek, A. Platil, and P. Ripka, "Multiple layer scanning in magnetopneumography," *IEEE Sensors J.*, vol. 9, no. 4, pp. 383–389, Apr. 2009.
- [7] P. Ripka, K. Draxler, and P. Kaspar, "Race-track fluxgate gradiometer," *Electron. Lett.*, vol. 29, no. 13, pp. 1193–1194, Jun. 1993.
- [8] F. Primdahl, P. Brauer, J. M. G. Merayo, and O. V. Nielsen, "The fluxgate ring-core internal field," *Meas. Sci. Technol.*, vol. 13, no. 8, pp. 1248–1258, Jul. 2002.

6.1.4 Effects of Core Dimensions and Manufacturing Procedure on Fluxgate Noise

This paper deals with the design of low noise fluxgate sensors with a tape-wound ring core. The parameters affecting the sensor noise are the sensor diameter and thickness of the tape layer. The bending stress increases the noise of sensors with a low diameter due to magnetostriction effects. The dependence of sensor noise on the tape layer thickness relates to the demagnetization factor.

Effects of Core Dimensions and Manufacturing Procedure on Fluxgate Noise

M. JANOŠEK^{a,*}, J. VYHNÁNEK^a, A. ZIKMUND^a, P. BUTVIN^b, B. BUTVINOVÁ^b

^aDept. of Measurement, FEE, Czech Technical University in Prague, Technická 2, 166 27 Praha, Czech Republic

^bInstitute of Physics, Slovak Academy of Sciences, Dúbravská cesta 9, 84511 Bratislava, Slovakia

The effect of demagnetizing factor and manufacturing procedure on noise of the fluxgate probes, manufactured from metallic glasses, is presented. The fluxgate probes were either tape-wound, or flat, wet-etched ringcore and race-track geometries. When combining low demagnetizing factor and high enough cross-section of the probe, a minimum in the noise dependence can be found. For 50 mm ringcores, in such minimum the noise value as low as 7 pT_{RMS} in 0.1-10 Hz frequency band was achieved, which is very low for an as-cast tape, and has not been reported before.

DOI: [BLIND TEXT/APhysPolA.125.TEMP--8882](#)

PACS: 75.75.-c, 75.30.-m, 75.50.-y, 07.55.-w, 75.70.-i

1. Introduction

The coupling of internal noise of the magnetic material to the noise of fluxgate sensors, manufactured from that material is ruled according to the commonly agreed practice, by the so called demagnetizing factor of the probe. This factor can be altered by changing the geometry of the probe (Fig. 1). For tape-wound sensors, core radius can be modified or the number of tape-turns can be altered. For ring-core and race-track geometries etched from tapes, changing the width of the annulus or stacking of the cores brings similar results.

The effect of the demagnetizing factor on noise was shown by Primdahl [1] for a given ringcore diameter of 17 mm. Tape-wound racetracks, studied in [2], were also optimized by altering the race-track geometry.

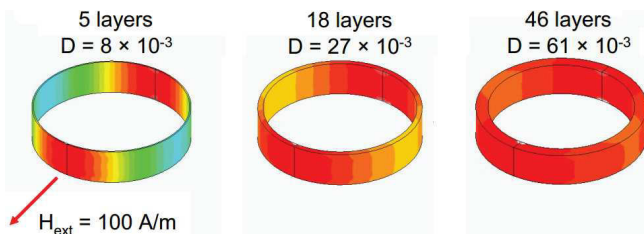


Fig. 1. Demagnetizing factor as a function of ring-core thickness (3D FEM simulation, the outer diameter (12 mm) is fixed).

However, mainly for ringcores with various diameters, the comparison is not straightforward: the bending stress, which becomes higher with smaller core diameter, is worsening the fluxgate probe noise. This can be handled either by appropriate zero-magnetostriction annealing [3], or at least by partially releasing the stresses

during field annealing of the tape-wound core in its final form [4].

A different situation exists for flat cores wet-etched from a wide amorphous tape. In this case the bending stress does not affect the probe noise, however the smoothness of etching process and mainly the art of fixing the core to the bobbin influence the noise. Fluxgate probes with etched race-track cores were previously studied in printed-circuit-board (PCB) sensors; however the internal stresses due to embedding the core in the PCB laminate affected probe performance [5]. In [4] the authors have shown noise figure also for the race-track core which was not embedded in the laminate, however its performance was limited by excitation electronics. In this study, the working conditions were all the same for all studied sensors in order to facilitate the comparison of results.

2. Material and geometry selection

In this work, Vitrokov 8116 – a Co-Cr-Fe-B-Si metallic glass tape was used, with an average thickness of 20 μm and with tape widths of 2.6 mm (wound cores) and 20 mm (etched race-tracks).

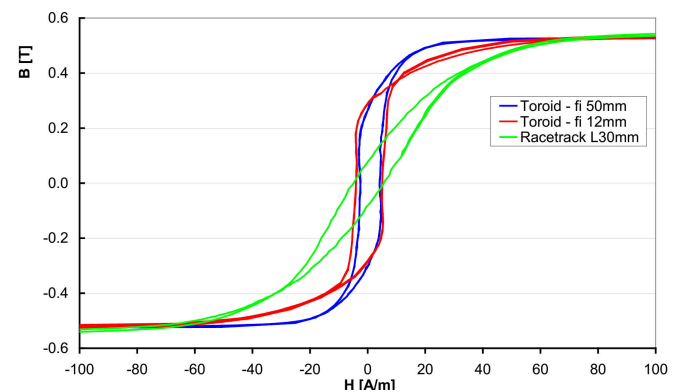


Fig. 2. B - H loops of the 3 core geometries.

*corresponding author; e-mail: janosem@fel.cvut.cz

For the tape-wound cores, the magnetoelastic effects can be seen by using the same material for 12 mm and 50 mm diameter (Fig. 2). From the $B-H$ loops it is evident, that even for these tapes with magnetostriction of $\sim 1 \times 10^{-7}$ this effect is present.

As for the 2.6 mm tape width, the material did not show any appreciable macroscopic heterogeneity, which otherwise causes poorly reproducible inhomogeneous magnetic anisotropy, brought about by macroscopic stress between surfaces and interior of many Fe-based ribbons (e.g. Finemets). The absence of this heterogeneity in Co-Cr-Fe-B-Si has been verified by comparing hysteresis loops prior to and after surfaces removal when the ribbon thickness was reduced by $10 \div 15\%$ ($2 \div 3 \mu\text{m}$).

In the 20 mm tape however, the heterogeneity was present but still acceptable. The different $B-H$ loop shape of the race-track in the comparison is evident but not caused by the tape macroscopic heterogeneity: the explanation lies in the as-cast anisotropy of the amorphous tape due to the manufacturing process, which is in the case of longitudinally etched race-tracks combined in both of the perpendicular branches of the race-track. An evidence for this behavior was shown in the MOKE pictures in [4].

4. Noise measurements – setup and results

The setup of electronics and operating conditions of the fluxgate probe were almost identical to that used in [4]. The resulting noise spectra for various tape thicknesses in the case of 50 mm ringcores obtained in a 6-layer magnetic shielding can, are shown in Fig. 3. To decrease the statistical error, an integral value of the noise in the frequency band of 0.1 to 10 Hz was calculated.

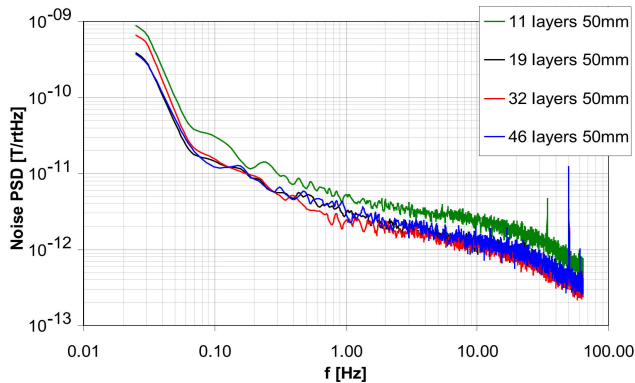


Fig. 3. Noise spectra of the 50 mm ringcore sensors.

The spectrum clearly maintains $1/f$ behaviour with lowpass filtering visible for frequencies above 12 Hz. The measuring procedure was done for the 50 mm cores in two tracks: 4 cores with different number of turns were produced and also one core was sequentially re-wound with decreased number of turns of the tape. The almost identical 50 mm results shown in Fig. 4 are thus independently obtained.

For 12 mm cores, there was a manufacturing problem of the bobbins, so only values for two demagnetizing fac-

tors are shown (5 and 10 turns). Although no dependence can be deduced, the overall increased noise, due to the bending stress is evident. This was further confirmed by the one-layer, 30 mm long race-track noise: absence of the bending stress and relatively low demagnetizing factor resulted in a noise comparable to that of 50 mm wound cores.

The results are in agreement with the behaviour found by Primdahl [1]. The noise for a given geometry slowly decreases with the decreasing demagnetizing factor up to a given minimum, from which it increases much faster.

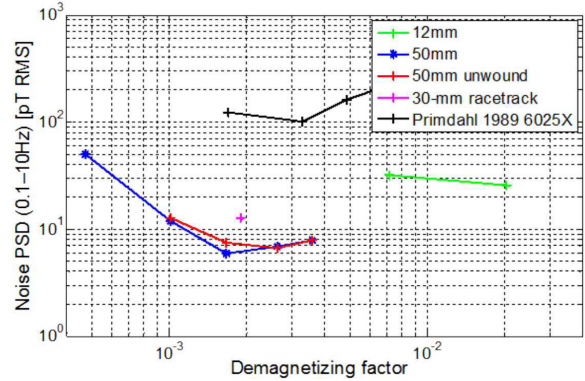


Fig. 4. Noise vs. demagnetizing factor for three geometries, including results of Primdahl for reference (he used 5, 10, 15 and 20 turns, respectively, on 17 mm diameter).

The authors offer the following explanation: as the cross-section of the magnetic material decreases in this case, also the signal-to-noise ratio of the whole sensor-electronics setup decreases, so the lower demagnetizing factor cannot bring a benefit anymore. Here the limitation was not the 5 nV lock-in amplifier noise, but rather remanent parasitic signal from unwanted even harmonics in the excitation current, which does not change when the core cross-section (and thus demagnetizing factor) is altered.

Acknowledgments

The authors are grateful for partial financial support by APVV grant SK-CZ-0078-11.

References

- [1] F. Primdahl, B.Hernando, O.V. Nielsen, J.R. Petersen, *J. Phys. E: Sci. Instrum.* **22**, 1004 (1989).
- [2] C. Hinrichs, J. Stahl, K. Kuchenbrandt, M. Schillin, *IEEE Trans. Mag.* **37**, 1983 (2001).
- [3] F. Primdahl, P. Brauer, J.M.G. Merayo, O.V. Nielsen, *Meas. Sci. Technol.* **13**, 1248 (2002).
- [4] P. Butvin, M. Janošek, P. Ripka, B. Butvinová, P. Švec sr., M. Kuzminski, P. Švec jr., D. Janičkovič, G. Vlasák, *Sens. Act. A* **184**, 72 (2012).
- [5] J. Kubík, L. Pavel, P. Ripka, *Sens. Act. A* **130-131**, 184 (2006).